**Phase-contrast x-ray imaging of microstructure and fatigue-crack propagation in single-crystal nickel-base superalloys**

**by**

**Naji Sami Husseini**

A dissertation submitted in partial fulfillment
of the requirements for the degree of
Doctor of Philosophy
(Applied Physics)
in The University of Michigan
2012

Doctoral Committee:

Professor Roy Clarke, Chair
Professor J. Wayne Jones
Assistant Professor Anton Van der Ven
Research Scientist John F. Whitaker
Professor Tresa M. Pollock, The University of California at Santa Barbara

2012

## ACKNOWLEDGMENTS

First and foremost, I'd like to thank my incredible wife, Jacque. Graduate school has been tough at times, and having her love and support helped me pull through the thorny times. Her proofreading skills are unparalleled, and without her keen eye for details, I might have committed a terminating-preposition crime against nature, something up with which she cannot put. I'd also like to thank Sami, Catherine, Jad, and Rami for endless support as well, from my younger nerdy days to the later ones, and to both sets of grandparents. Pépé, je suis devenu l'ingénieur que vous devriez avoir été!

My deepest thanks go to my advisor, Professor Roy Clarke. He gave me freedom to explore as I made my way through graduate school and provided guidance when I traipsed down the primrose path of dalliance. His dedication to teaching, mentoring, and outreach is something I greatly respect and strive to emulate. Thank you for everything, Roy.

Professors Wayne Jones and Tresa Pollock have been close advisors since my first days at Michigan, and they have involved me in conferences and projects that have broadened this physicist's horizons beyond theoretical chalkboard scribbles. From probing materials questions to crashing The Ohio State University reunions to the occasional good-natured PowerPoint barbs when presenting in succession, I have many positive memories of our work together. Thank you as well to the other members of my committee, Professor Anton Van der Ven and Dr. John Whitaker for their insight and suggestions in this manuscript.

I'm indebted to some brilliant colleagues in physics who've made long days at synchrotrons more fun than they should be. Divine Kumah and Codrin Cionca have been very good friends and mentors from the beginning, both in science and love ("Got a ring

for Jacque yet? Here's a Tiffany's catalog."). Christian Schlepütz and Yongsoo Yang have been kind enough to let me tag along on their synchrotron runs to Switzerland (noch ein grosses, bitte). Yizhak Yacoby has always been an inspiration in how much he can work, despite his age, and what he has accomplished in his career. Thanks also to the other Clarke group members, Yuwei Li, Ibrahim Oraiqat, Alexandru Riposan, and Vladimir Stoica for help and support throughout the years. Outside of the Clarke group, Dennis Allen and Ramon Isea-Torres were always good for discussions of scientific pedagogy and bovine aquatics, as well as afternoon coffee and scones while enjoying the best Ann Arbor summers have to offer. And Charles Sutton, thanks for making everything happen.

Thank you to the staff at the Advanced Photon Source, particularly to Dohn Arms, Alex Deriy, Eric Dufresne, Wah-Keat Lee, and Don Walko. Thank you also to those at the Swiss Light Source, especially Professor Phillip Willmott and Stefan Pauli. These are both fantastic laboratories that awe me whenever I enter them. By the fifth night shift, though...

I appreciate greatly my collaborations and discussions with Clinique Brundidge, Jason Geathers, Anish Kumar, Liu Liu, Jian Yi, and Martina Zimmermann. They helped prepare many of the samples and assisted at beamtimes, and their insights were useful in explaining many results. Liu Liu created the brilliant finite element model discussed in Chapter 5 and deserves significant credit for that. Finally, I'd like to Chris Torbet, one of the kindest people I know and one mullet short of MacGyver. We shared many date nights together with (hurried) dinners and (crack-propagation) movies, enough to make Jacque jealous.

Finally, I owe a great deal of my remaining sanity to all the members – white belt to black belt, long-gone to newly-joined – of the University of Michigan Taekwondo Club. Every painful kick and emotional tournament win or loss reminded me that I was alive. The opportunity to teach and train with such great people relieved stress (with personal crack propagation occurring on only three occasions), developed my oratory skills and teaching skills, and formed valuable friendships. Sweating and suffering with someone forms a bond difficult to replicate any other way.

# TABLE OF CONTENTS

# LIST OF FIGURES

**FIGURE**

# LIST OF TABLES

**TABLE**

## ABSTRACT

Single-crystal nickel-base superalloys are ubiquitous in demanding turbine-blade applications, and they owe their remarkable resilience to their dendritic, hierarchical microstructure and complex composition. During normal operations, they endure rapid low-stress vibrations that may initiate fatigue cracks. This failure mode in the very high-cycle regime is poorly understood, in part due to inadequate testing and diagnostic equipment. Phase-contrast imaging with coherent synchrotron x rays, however, is an emergent technique ideally suited for dynamic processes such as crack initiation and propagation. A specially designed portable ultrasonic-fatigue apparatus, coupled with x-ray radiography, allows real-time, *in situ* imaging while simulating service conditions.

Three contrast mechanisms – absorption, diffraction, and phase contrast – span the immense breadth of microstructural features in superalloys. Absorption contrast is sensitive to composition and crack displacements, and diffraction contrast illuminates dislocation aggregates and crystallographic misorientations. Phase contrast enhances electron-density gradients and is particularly useful for fatigue-crack studies, sensitive to internal crack tips and openings less than one micrometer.

Superalloy samples were imaged without external stresses to study microstructure and mosaicity. Maps of rhenium and tungsten concentrations revealed strong segregation to the center of dendrites, as manifested by absorption contrast. Though nominally single crystals, dendrites were misoriented from the bulk by a few degrees, as revealed by diffraction contrast. For dynamic studies of cyclic fatigue, superalloys were mounted in the portable ultrasonic-fatigue apparatus, subjected to a mean tensile stress of

~50-150 MPa, and cycled in tension to initiate and propagate fatigue cracks. Radiographs were recorded every thousand cycles over the multimillion-cycle lifetime to measure micron-scale crack growth. Crack openings were very small, as determined by absorption and phase contrast, and suggested multiple fracture modes for propagation along {111} planes at room temperature, which was verified by finite element analysis. With increasing temperature, cracks became Mode I (perpendicular to the loading axis) in character and more sensitive to the microstructure. Advancing plastic zones ahead of crack tips altered the crystallographic quality, from which diffraction contrast anticipated initiation and propagation. These studies demonstrate the extreme sensitivity of x-ray radiography for detailed studies of superalloys and crack growth processes.

# CHAPTER 1

# INTRODUCTION

Since their discovery in 1895 by Wilhelm Röntgen [1], x rays have been an invaluable imaging tool in diverse disciplines ranging from radiology to geology to biology. Initially, the main source of contrast was different attenuation rates between bone, muscle, and metal, in part due to limitations from low photon counts and incoherent sources. Over a hundred years later, not only would current x-ray diagnostic techniques reveal Frau Röntgen's bone structure and whether Herr Röntgen splurged on a real diamond or skimped with a cubic zirconia gem, but they would show the exact atomic arrangement and lattice structure of the gem with diffraction, edge enhancement at the interface between bone and soft tissue from phase contrast, and real-time blood flow through her rapidly ionizing fingers with very short exposure times. Today's brilliant third-generation synchrotron sources can produce extremely high photon counts at a specific wavelength with the spatial and temporal coherence required to enable all these imaging modalities. The panoply of promising possibilities is endless.

## 1.1 X-Ray Imaging

An emergent technique for x-ray radiography is called phase-contrast imaging (PCI) [2], pioneered in optical microscopy by the Dutch physicist Frits Zernike in 1930 for imaging biological objects otherwise invisible without staining [3]. It was only implemented in x-ray science in the mid-1990s [4-6], due to technological improvements in synchrotron science. In standard bright-field microscopy, contrast comes from the difference in attenuation of light by various parts of a sample, similar to Röntgen's experiment. Although cells and diatoms are very thin and mostly transparent,

their refractive indices differ from that of air, which refracts and retards light and causes it to travel a different optical path compared with light traveling through air only. This phenomenon leads to interference effects, providing contrast where only a minor difference in attenuation exists. Zernike's work was indeed constructive, starting with a successful image of a diatom (Fig 1.1) and culminating with a Nobel Prize in 1953. Since x rays are just another type of electromagnetic radiation, these same principles for visible light apply to them, and they will be discussed in greater detail in Chapter 3.

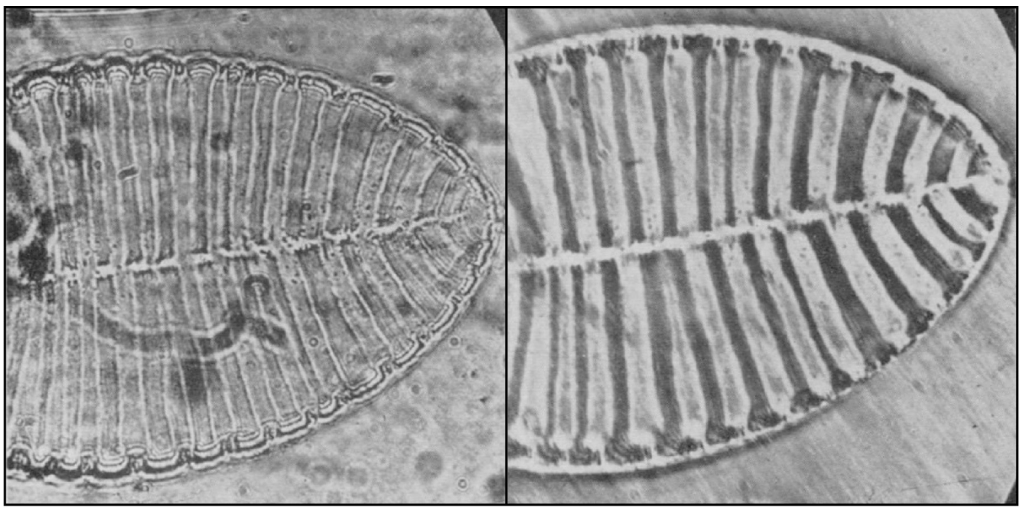

Fig. 1.1. First photomicrograph by Zernike in 1932, showing a diatom imaged by bright-field (left) and phase-contrast (right) microscopy [3]. No scale bar provided.

PCI in both optical microscopy and x-ray radiography require spatially, also called laterally, coherent incoming radiation, one of the reasons why it was not seen in x-ray radiography until recently. Owing in part to the short source-to-sample distance compared to the source size, traditional table-top x-ray sources generally lack spatial coherence. The incident radiation fronts still have some spherical characteristics; and given that the wavelength of x rays is on the order of Ångstroms, even very small curvatures can destroy any spatial coherence. The output radiation of a synchrotron source is highly spatially coherent by design, with finite source sizes and divergences but very large source-to-sample distances upwards of 50 m at imaging beamlines. At the Advanced Photon Source (APS), for example, the source size and divergence are

~275 µm and ~11.5 µrad, respectively, in the horizontal direction and ~11 µm and ~4.0 µrad in the vertical direction [7], with even shorter values possible when the synchrotron is operated under different modes (e.g., Reduced Horizontal Beta). The elongation along the x-axis and contraction along the y-axis is due to the radiation profile from the undulator that characterizes synchrotrons of the third generation. An undulator is a series of alternating magnets that force the electron beam into a series of gentle undulations. Electrons emit synchrotron radiation whenever they are bent, and by matching the frequency of the oscillations to the electron propagation speed, the radiation adds constructively for a collimated, coherent beam [8-9].

While PCI does not require monochromatic radiation [5], its edge-enhancing effects become blurred with several wavelengths. Conventional x-ray sources may be polychromatic (Bremsstrahlung), or monochromatic, where discrete wavelengths are determined by specific atomic-energy levels in a metal target. Controlling the wavelength of such monochromatic sources requires changing the target, and the types of viable target metals greatly limits the usable energies. Synchrotron beamlines with monochromators (e.g., double-crystal silicon (111)) have easily tuned energies with very narrow energy spreads of $\Delta E/E \approx 10^{-4}$, aiding in PCI and increasing sensitivity to certain elements in the sample by tuning the energy above or below its characteristic x-ray absorption edge. The energy resolution also determines the degree of temporal, or longitudinal, coherence, which is very important for Bragg diffraction [10].

A final advantage synchrotrons have over traditional x-ray sources is a significantly higher brilliance, which is defined as photons per second per 0.1% energy bandwidth per milliradian squared per millimeter squared. A brilliant source has a high fluence, defined as photons/second, at a very narrow wavelength, which is important for monochromatic PCI and allows imaging of thick, dense materials that may only transmit a tiny fraction of photons. High brilliance also means small values for the divergence and source size area, indicative of collimation and thus of spatial coherence. Third-generation synchrotron sources typically have brilliances exceeding

$10^{19}$ (ph/s) / mrad$^2$ / mm$^2$ / 0.1%bw, which is several orders of magnitude greater than conventional laboratory sources (Fig. 1.2).

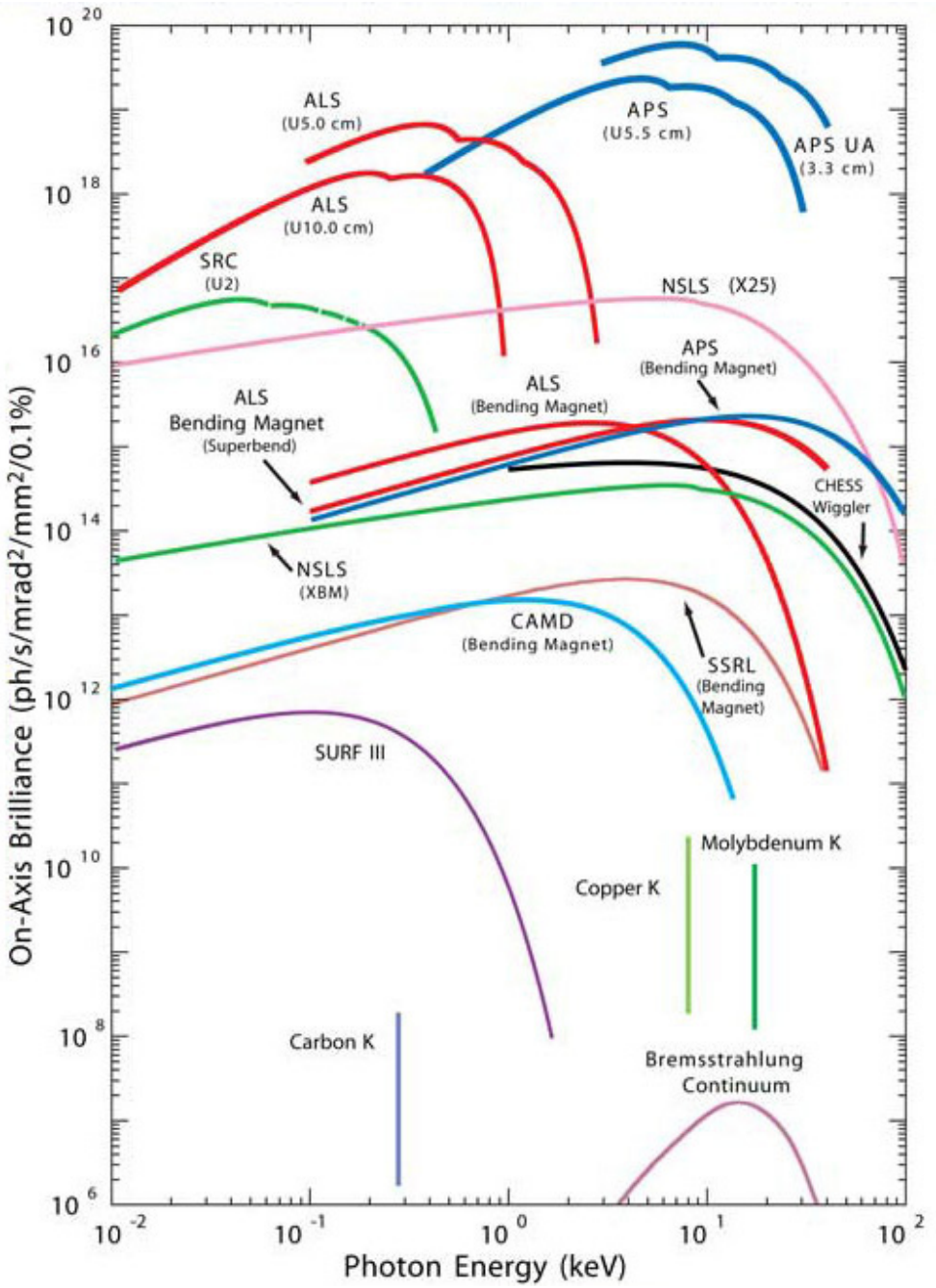


Fig. 1.2. Comparison of brilliance between a number of synchrotron sources (acronyms) and conventional sources (three vertical lines and Bremmstrahlung) [11]. The APS, the facility used extensively in this dissertation, is located near the top-right corner.

Three main techniques currently exist for PCI. The first involves splitting the initial beam into two separate components. One passes through the sample and acquires a phase shift while the other travels an equal path length but avoids the sample; both waves interfere at the detector (Fig 1.3a). This method is called interferometer-based PCI and is similar to Zernike's original method [2-3]. Alternatively, if the transmitted beam after the sample is reflected from an analyzer crystal to the detector, this method is called diffraction-enhanced imaging (DEI) [2,12]. After refraction within the sample, the rays will reflect at different angles to the detector, altering the contrast (Fig 1.3b). The third method, in-line or propagation-based PCI, sets the sample at a distance sufficiently far from the detector for diffracted and undiffracted components of the beam to interfere and diverge (Fig 1.3c) [2,4-5,13-14]. The setup is the simplest of the three and very similar to traditional absorption radiography. This particular PCI method will be employed in this dissertation.

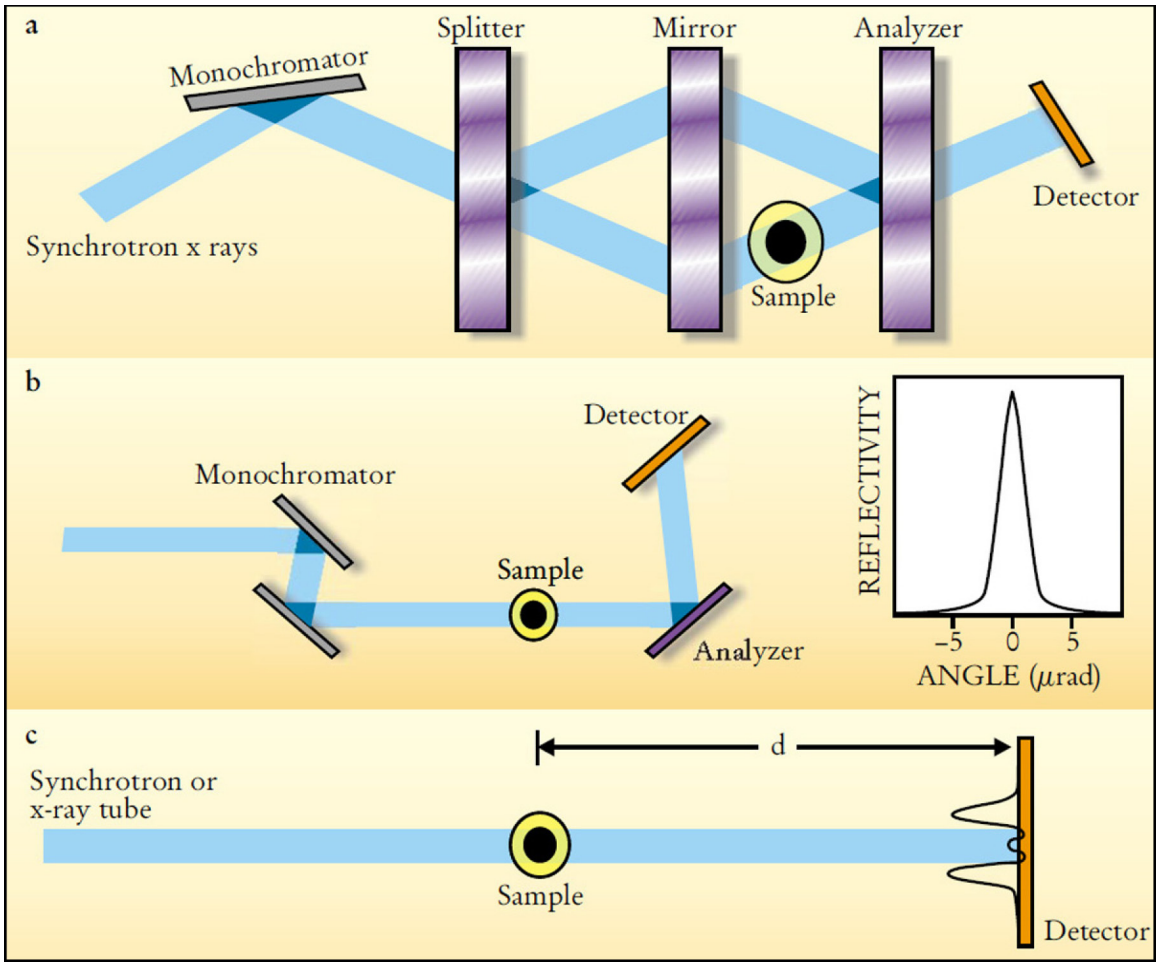


Fig. 1.3. Three experimental setups for phase-contrast imaging, including (a) interferometer-based PCI, (b) diffraction-enhanced PCI, and (c) in-line or propagation-based PCI [2].

Only recently has the PCI potential of third-generation synchrotron sources been realized (Fig. 1.4). Pioneering studies of mammography [15], digestion and respiration in insects [16-17], fuel spray from nozzles [18], and droplet coalescence [19] have begun to impact their respective fields with diagnostics not limited to invasive surgery or postmortem analyses. In these cases, the object under investigation barely attenuates the incoming photons, producing minimal contrast due to absorption alone. As the tumor, food, fuel, or droplet has a slightly different index of refraction than its surroundings, the optical path length (OPL) of the radiation is altered, and the resulting phase difference leads to interference and improved contrast. This is the basis for the

technique's extreme sensitivity to small changes in OPL and its utility for real-time diagnostics.

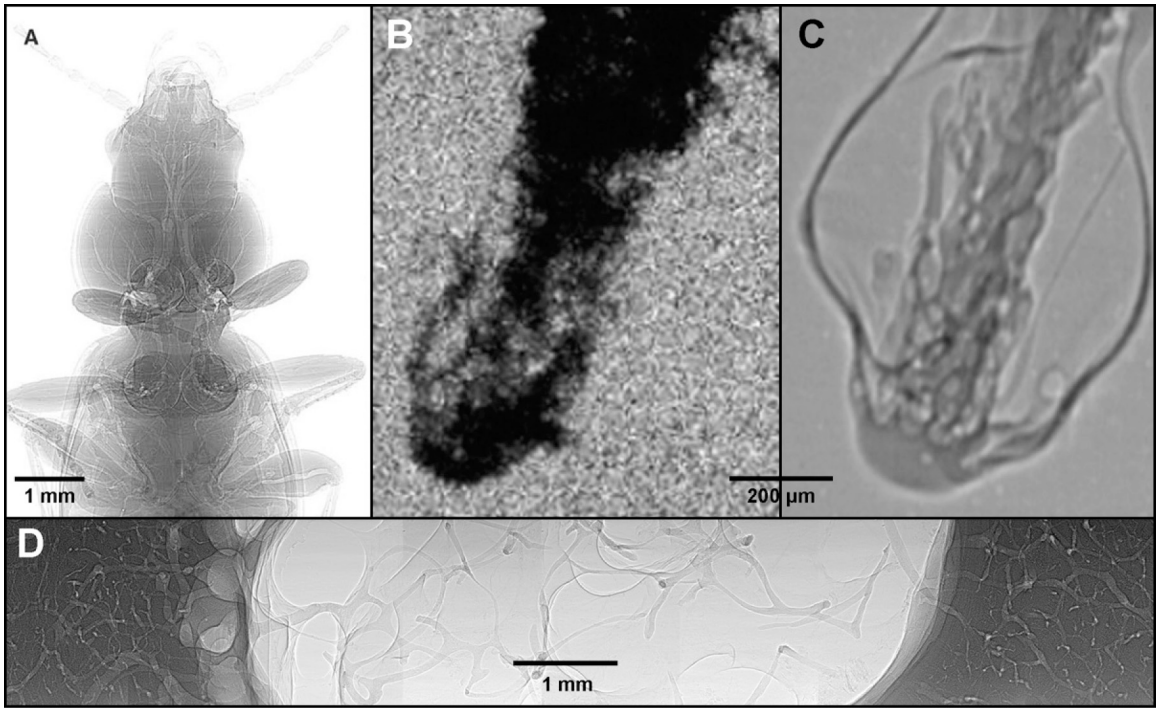


Fig. 1.4. Sample phase-contrast radiographs. (A) Tracheal system of a pterostichus stygicus (a type of beetle); adapted from [17]. (B) Visible-light and (C) x-ray snapshot taken 20 µs after start of fuel spray injection; adapted from [18]. (D) Diaphysis of canine femur; sample harvested and prepared by Dr. J. H. Cole.

PCI has also been used in materials research applications, such as the mapping of three-dimensional (3D) grain boundaries and damage propagation in cast aluminum cylinders [20-21], as well as crack opening in aluminum [22]. In these applications, the sample attenuates the x-ray beam appreciably, such that phase contrast is not the sole contrast mechanism, but rather provides an enhanced absorption radiograph. The technique is non-destructive and produces radiographs that are 3D projections of two dimensions; with some additional work, the images can be reconstructed using tomographic techniques [23]. Mapping grain boundaries is aided by diffraction, in addition to absorption and phase contrast, to locate regions with different crystallographic orientation [21].

As shown in this section, the PCI technique is ideally suited for non-destructive, *in situ*, real-time studies where features of interest may span several spatial orders of magnitude and are virtually invisible to simple bright-field imaging. One critical application not yet explored in the literature with PCI is understanding and anticipating the initial nucleation and propagation of catastrophic fatigue cracks during high-cycle fatigue. This is the main focus of the dissertation.

## 1.2 Superalloys

Operating conditions in air-, space-, and land-based turbine engines impose extreme conditions in critical engineering components, such as blades and vanes. These parts can operate under significant stresses at temperatures up to 1,200°C, yet they must retain their mechanical strength and resist creep and fatigue-crack damage over long lifetimes [24]. Superalloys were introduced shortly after World War II to address these needs and have since been continually refined and developed. They are typically based on Group VIIIB elements, particularly nickel, iron, and cobalt, with additives of various lighter elements (e.g., titanium, aluminum) and heavy elements (e.g., tungsten, rhenium, zirconium, tantalum). The exact composition and ratio of elements depends on the application and fabrication method [25]. Arguably the most important class of superalloys is nickel-base, comprising 40-50% of an engine's total weight and located in the most demanding areas [25]. The single-crystal variety has a higher melting point than the polycrystalline type, and thus they are used in the hottest sections of turbines. Polycrystalline superalloys are found in cooler sections of turbine engines, such as turbine disks, because of their lower melting point and greater susceptibility to creep and fatigue-crack initiation at ubiquitous grain boundaries.

Single-crystal nickel-base superalloys are extremely durable because of many microstructural features spanning numerous length scales, from atomic to macroscopic. At the hundred-nanometer scale is a two-phase system consisting of a γ matrix and a high volume fraction (about 50-70%) intermetallic ´γ phase, which is ductile and strengthens the overall material to protect against fatigue-crack propagation and creep

damage (Fig. 1.5) [26]. This precipitate phase is nominally $Ni_3Al$, and it is further strengthened by elements such as niobium, tantalum, and titanium to form $Ni_3$(Nb, Ta, Ti) compounds. These additives also affect the volume fraction of which in turn affects the rupture lifetime during creep [25]. Other refractory alloying elements, including rhenium and tungsten, segregate to the γ phase and improve the high-temperature mechanical properties. Despite upwards of ten constituent elements and a lattice mismatch between the γ and γ′ phases of approximately 0.3% [25,27], the crystalline planes of the γ-Ni matrix and cuboidal γ′ precipitates are in registry, maintaining an $L1_2$, or face-centered-cubic (FCC) structure, across the superalloy.

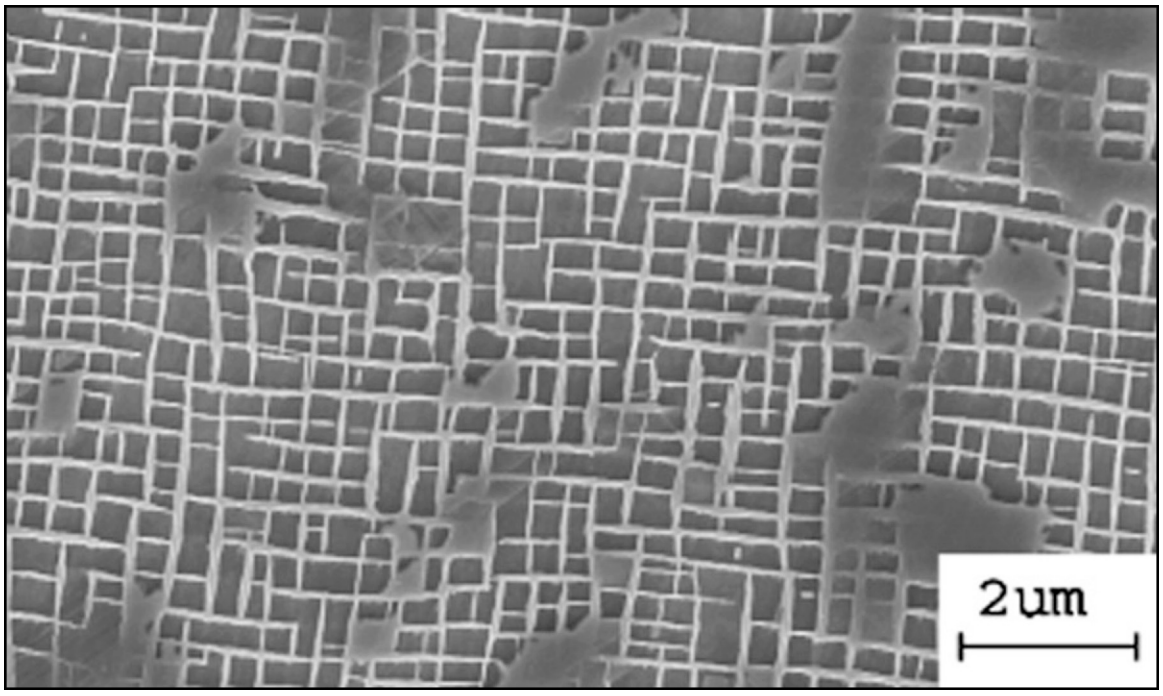


Fig. 1.5. Microstructure of a single-crystal nickel-base superalloy showing the cuboidal γ′ precipitates embedded within the γ matrix [25].

On a slightly larger length scale (1 to 10 μm) are metal carbide inclusions (Fig. 1.6). Carbon is added to improve single-crystal growth and reduce damage accumulation at any grain boundaries that may form during solidification of complicated geometries [28-29]. Carbon does not remain in a pure form and bonds with several of the reactive and refractory elements added to the γ and γ′ phases, forming metal carbides of

hafnium, titanium, tantalum, and tungsten, for example [25]. These carbides tend to aggregate at grain or dendrite boundaries, and while beneficial for high-temperature rupture strength, they may produce stress concentrations that hasten fatigue-crack initiation [30].

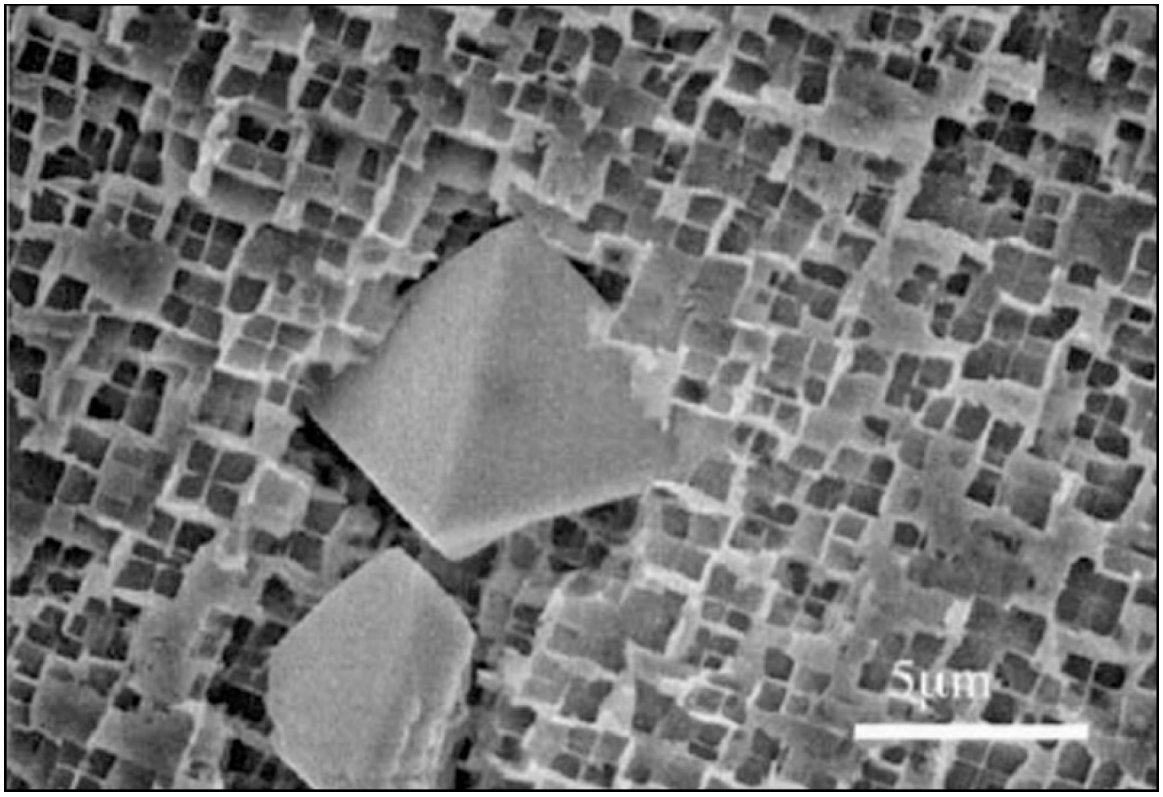


Fig. 1.6. Scanning electron micrograph of two blocky tantalum metal carbides amid the γ and γ′ phases [28].

At the hundred-micron scale are dendrites, characteristic of single-crystal superalloys grown by directional solidification. Solid superalloy is liquefied and poured into a ceramic investment mold at temperatures well above the melting point. The mold is withdrawn slowly at between 5 to 40 cm/hr to a vacuum (Bridgman method) or liquid-metal-cooled (LMC) zone to create a unidirectional thermal gradient of approximately 10 to 100°C/cm [25,31]. As the melt begins to solidify, dendritic structures form first, oriented such that the <001> crystallographic axis is coincident to the withdrawal direction, with secondary dendrites forming in the orthogonal plane. The arboresque

structures at the top of the melt are visible in Fig. 1.7, where the liquid has been withdrawn before complete solidification. Separations between the dendrite cores and branches, ranging from tens to hundreds of microns, are closely related to the cooling rate during withdrawal.

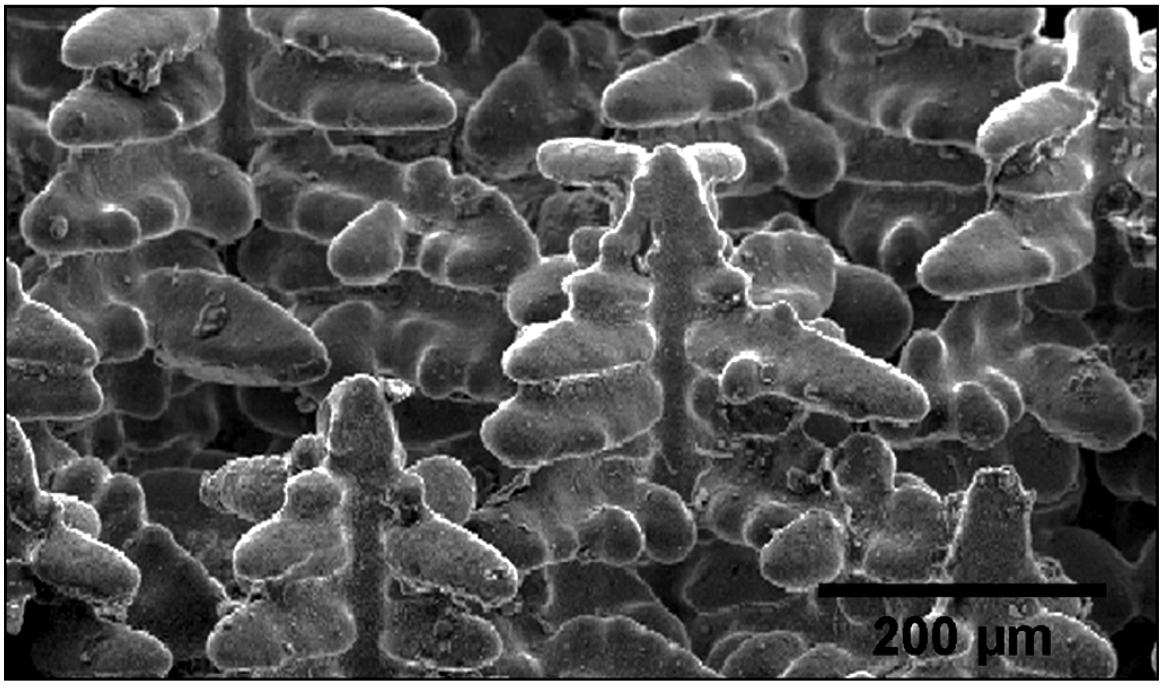


Fig. 1.7. Scanning electron micrograph of the top of the melt during solidification with the liquid decanted [32]. The <001> axis is vertical and coincident with the dendrite cores. Primary and secondary dendrites are visible. Image courtesy of M. P. Echlin.

Some refractory-metal additives, such as rhenium and tungsten, diffuse slowly and segregate non-uniformly throughout the dendrite [33], generally concentrating at the center of the dendritic core. This thermodynamically driven segregation process may cause convective instabilities during withdrawal and break down the single-crystal solidification front, possibly leading to high-angle grain boundaries [34-35]. Furthermore, elemental inhomogeneity may adversely affect mechanical properties, so a detailed understanding of the heavy-element distribution is crucial.

The last liquid to cool during solidification forms the interdendritic regions, and while still coherent with the dendritic region, it frequently has a different composition. For example, the interdendritic regions of the René N5 superalloy [36] has a slightly

different composition that the dendrites (e.g., more heavy elements and less nickel) and contains various metal carbides [25,30]. Due to thermal stresses from solidification and slight misalignments between adjacent dendrites, dislocations may accumulate in the interdendritic regions (Fig. 1.8), causing neighboring dendrites to have slight crystallographic misorientations of up to a few degrees [32]. This subtle mosaicity is not well-studied, even though dislocation networks may influence primary creep behavior [26].

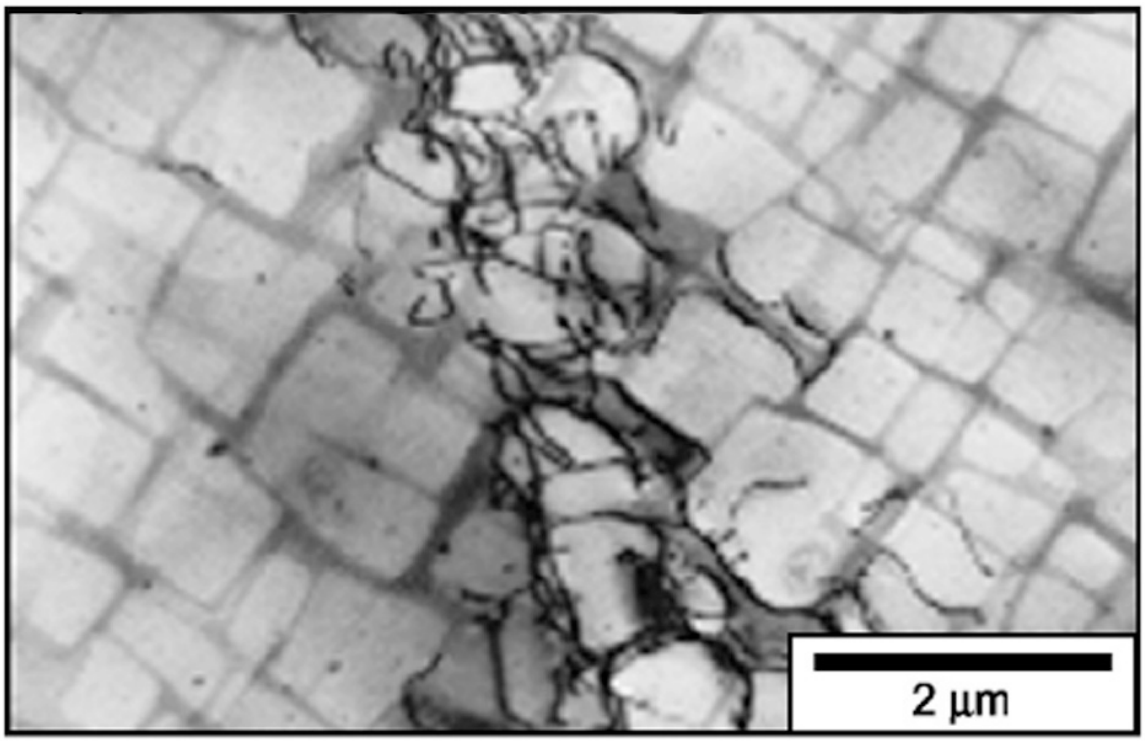


Fig. 1.8. Transmission electron micrograph of the γ and γ′ phases of two dendrites separated by a dislocation-rich interdendritic region [26,32].

The length scales spanned by the hierarchical microstructure and damage mechanisms in superalloys are immense: nearly seven orders of magnitude, ranging from atomic-scale dislocations to micrometer-scale carbides to millimeter-scale fatigue cracks. These length scales are interconnected: a carbide may spawn a millimeter-long fatigue crack, which is preceded by dislocations along slip bands. Obtaining information

across the full spatial breadth is important during *in situ* real-time imaging of crack propagation, because many features contribute to and mitigate fatigue damage.

## 1.3 High-Cycle Fatigue

During turbine blade operation nickel-base superalloys endure two types of fatigue, low-cycle fatigue (LCF) and high-cycle fatigue (HCF), that may lead to catastrophic crack propagation. LCF occurs in aircraft components during takeoff and landing due to thermomechanical loading cycles, and in terrestrial applications (e.g., power plants) during start-up and shutdown. LCF is generally defined by a lifetime of less than $10^5$ cycles and involves stresses large enough to exceed the elastic region and cause plastic deformation during each cycle [37]. This type of fatigue in various components has led to numerous accidents, including two de Havilland Comet aircraft in 1954 [38] and more recently in Alaska Airlines Flight 261 in 2000 [39]. HCF, by comparison, occurs in components subject to very rapid vibrations, such as jet-engine turbine blades. LCF is generally better understood than HCF, since it can be more easily tested in the laboratory with conventional servo-hydraulic testing equipment operating at a maximum frequency of ~100 Hz. Accumulating $10^5$ cycles in the laboratory is feasible, but anything higher is prohibitively time-consuming.

HCF is less well-studied and consequently is the last major failure mode remaining in commercial turbine blades [40]. It involves more than $10^6$ cycles accumulated at kHz frequency with stress amplitudes low enough to stay in the elastic region and much lower than the yield stress [37]. Oscillations of this scale are usually transient effects encountered in service due to turbulent airflow around the turbine or when the airfoil passes rapidly through alternating high- and low- flow regions [41]. Even larger cycles counts, between roughly $10^8$ and $10^{10}$, define the very high-cycle fatigue (VHCF) regime [42]. HCF and VHCF are of great interest in industry for extending lifetimes of existing systems and improving design lives in new transportation and energy systems. Both regimes are even more important for the military, which estimates that 56% of engine-related failures in United States Air Force aircraft between

1982 and 1996 were attributed to HCF [43]. Because other failure modes, such as creep and LCF, are better understood, improved turbine-blade materials and component-retirement procedures have significantly decreased accidents attributed to these modes [40].

Studying HCF is more difficult than LCF using traditional servo-hydraulic equipment, because applying $10^9$ cycles at 100 Hz, for example, requires nearly four months of continuous operation. Reaching the HCF and VHCF regimes and simulating service-grade stresses has only recently become feasible with the development of ultrasonic fatigue testing equipment, which use a piezoelectric actuator to generate kilohertz-frequency cycles [44]. Though in existence since the 1950s, they have only recently seen significant adoption in laboratories for a broad assortment of materials [45-49]. These apparatus, typically operating at 20 kHz, can accumulate $10^9$ cycles in just 14 hours. Previous studies have not shown a significant difference in fatigue behavior with different loading frequencies in superalloys [49-50]. The work described in this dissertation is the first to combine HCF techniques with real-time phase-contrast x-ray imaging. The specific details of the portable ultrasonic fatigue apparatus work will be discussed in greater detail in Chapter 2.

Some major differences exist between the different fatigue regimes that make extrapolation of preexisting LCF studies to HCF difficult or inaccurate. Plastic deformation during LCF tends to spread among the majority of grains, while in HCF it is localized at strain concentrators that act as weak links and may ultimately lead to fatigue-crack initiation [51]. These high-strain regions include microstructural features such as pores, inclusions, carbides [25,52], and large grains [24,48], particularly those with high-angle grain boundaries [53]. Also acting as damage-initiation sites are larger-scale defects from machining, foreign-object damage, and certainly any notches introduced for testing purposes (an approach employed extensively in this work). Some of these features may have beneficial effects to mitigate other types of damage or may be difficult to eliminate from fabrication or operation. Real materials, therefore, will almost certainly have some localized regions of high stress during operation, though it

may not be significant enough for crack initiation. While fatigue-susceptible features can be located at the surface of a material where conventional surface-diagnostic tools can image them *in situ*, microstructural features are more likely found internally, based simply on the surface-to-volume ratio, and are therefore invisible to surface imaging techniques. For this and other reasons, including compressive residual stresses on the surface and environmental effects, fatigue cracks during HCF generally tend towards subsurface initiation [48,54-55].

The stress concentrations endemic in HCF can be quantified with the stress-intensity factor (SIF) range, $\Delta K$. In a simple example of a cracked planar sample under a uniform uniaxial stress,

$$\Delta K = Y \cdot \Delta\sigma \cdot \sqrt{\pi \cdot a} \quad [1.1]$$

where $Y$ is a geometric factor based on the crack orientation, $\Delta\sigma = \sigma_{max} - \sigma_{min}$ is the stress amplitude in MPa, and $a$ is the crack length in meters [56]. SIFs are useful parameters for determining the severity of a defect and the corresponding likelihood of crack initiation and propagation. Graphs of the fatigue-crack growth increment, defined as the derivative of crack length with respect to the number of cycles ($N$), as a function of $\Delta K$ tend to have three regimes in ductile solids (Fig. 1.9). Regime A contains the threshold for crack initiation, $\Delta K_{th}$, and is the domain of very slow crack growth where $da/dN \leq$ ~1 nm/cycle. Crack initiation and growth in this regime are highly sensitive to stress concentrations at microstructural extremes [57]. Regime C is the rapid-growth rate region, where catastrophic failure can occur very quickly as $\Delta K$ approaches $K_c$, called the fracture toughness. Regime B, where the crack rate is governed by a simple power law and relatively insensitive to microstructure, is frequently modeled according to the Paris Law [58]:

$$\frac{da}{dN} = C(\Delta K)^m \quad [1.2]$$

where $C$ and $m$ are scaling constants influenced by composition, microstructure, load ratio, and temperature. This model does not completely describe crack growth in single crystals, which may grow as a combination of all three separation modes and not just by the simple tensile opening mode [59]. These cracks are more sensitive to the lattice and

any anisotropy in the mechanical properties [56], as evidenced by the crystallographic and non-crystallographic crack character in single-crystal superalloys [60]. This will be discussed in Chapter 5.

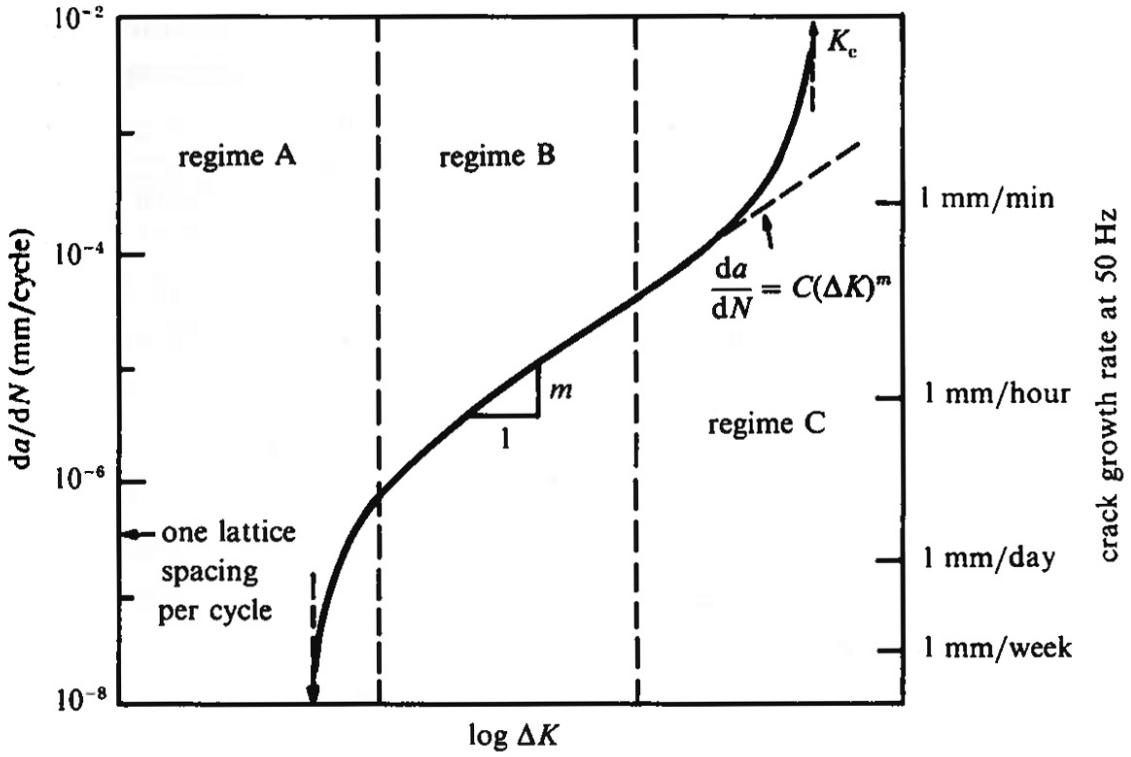


Fig. 1.9. Schematic illustration of the three different regimes of stable fatigue-crack propagation [56]. The dashed arrow on the leftmost part of the curve indicates $\Delta K_{th}$, the threshold for crack initiation.

Another difference between LCF and HCF is the percentage of the total fatigue lifetime spent during fatigue-crack initiation versus propagation. This can be described as

$$N_T = N_I + N_P \qquad [1.3]$$

where $N_T$ is the total number of cycles to failure, and $N_I$ and $N_P$ are the number of cycles during initiation and propagation, respectively. For long cracks in monocrystalline materials, the propagation stage of Eq. 1.3 may be further subdivided into Stage I (crystallographic) and Stage II (non-crystallographic) crack growth [59,61]:

$$N_T = N_I + N_{P,I} + N_{P,II} \quad [1.4]$$

In LCF, cracks initiate quickly and propagate slowly with respect to $N_T$, and they tend to be large enough for detection during routine maintenance inspections (Fig. 1.10); moreover, the slip bands at the initiation point are frequently detectable at the surface [62]. Components exhibiting this damage can be removed from service or repaired before catastrophic failure. HCF, on the other hand, is dominated by the initiation phase, with a correspondingly slow fraction of the lifetime spent during crack propagation. Successful detection by the same techniques used for LCF crack growth must happen after initiation but obviously before failure, leaving only a small window for discovery.

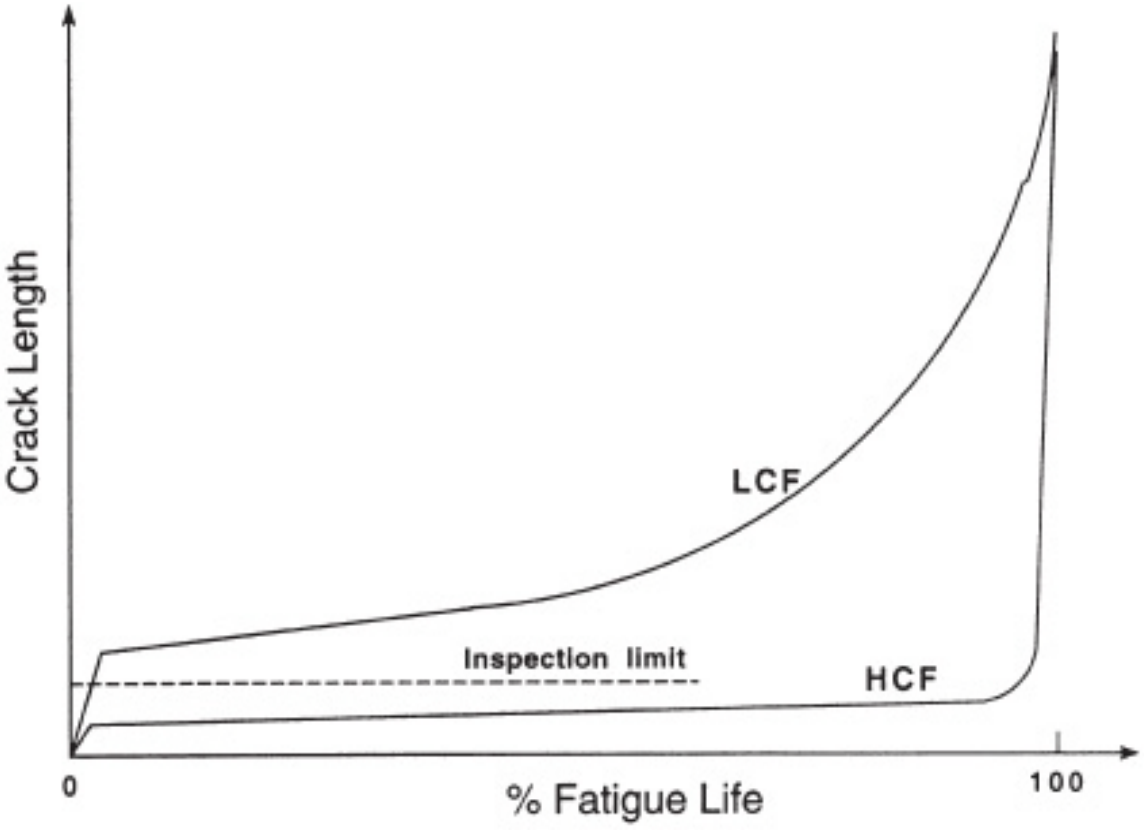


Fig. 1.10. Plot showing conceptual differences between HCF and LCF [40]. Note the significant difference in % Fatigue Life between when an LCF crack can be detected during inspection compared with an HCF crack.

Unfortunately, with low cyclic stresses in HCF, cracks initiate in regime A (Fig. 1.9), where the growth rate is highly dependent on the local microstructure and are thus more unpredictable [40]. The minimum threshold for crack initiation is also highly variable in HCF, and it is best determined statistically based on empirical results. Crack initiation is difficult to predict and complicated to image when growth rates are very low; failure, though, is all too easily detected. Therefore, solving the problem of HCF-caused failure has two steps: (1) understanding the mechanisms of crack initiation and (2) detecting pre-cracks and crack propagation as soon as possible. The latter problem in nickel-base superalloys will be a focus of this dissertation, and because crack nucleation tends to occur internally, a 3D imaging method is necessary for any real-time diagnostics.

## 1.4 Prior Synchrotron Work

Synchrotrons are no strangers to fatigue studies, although phase-contrast synchrotron radiography during high-cycle fatigue of any material has not been reported to our knowledge. While PCI produces images in real space rather than phase space, removing the need for cumbersome image-reconstruction algorithms, radiography limits the sample thickness to millimeter thicknesses (depending on the x-ray photon energy); otherwise, x rays will be too severely attenuated and provide very weak images on the detector. Surface diffraction, on the other hand, only requires photons to interact with the surface atoms, with the actual penetration depth dependent on the energy and angle of incidence. Diffraction has complemented traditional diagnostic methods in studies of surface defects [63-64], solidification [65], and strain and $\gamma/\gamma'$ phase misfits [66-68] in superalloys. In other materials, for example, Ritchie and colleagues have used microdiffraction to study crack tips in Nitinol to show the surrounding strain fields, effects of texture on the propagation path, and austenitic/martensitic transition [69]. Microdiffraction studies on other important alloys, such as Ti-6Al-4V [70] and Al-Li 2989 T8E41 [71], have mapped out von Mises stress distributions around crack tips [56]. In general, diffraction is particularly useful for

strain measurements; without rastering the x-ray beam across the sample, though, diffraction is limited to small regions, such as those near crack tips and defects, and not for real-time or large-area work. Radiography can produce qualitative maps of strain distributions [32], though not as quantitatively as via diffraction, and this will be discussed in Section 3.3.

For radiography, almost all reported cyclic-loading experiments have been in the LCF regime. Without widespread use of high-frequency fatigue apparatus, real-time studies of HCF have been impossible due to limited time available at synchrotron beamlines. Significant work has been done at the European Synchrotron Radiation Facility (ESRF) in France with LCF crack propagation in light metals, including aluminum and magnesium [21,72-74]. They have shown that x-ray imaging is sensitive to microstructural features, such as porosity, and how crack propagation is affected by crack closure and various driving forces using tomography [74]. In more recent work [21], grain orientation was determined by matching Friedel pairs of diffraction spots, and the full 3D structure of the cracked material was reconstructed using tomographic techniques (Fig. 1.11). Studies from the ESRF have reported that cracks frequently changed direction at grain boundaries, depending on their intergranular orientation and Schmid factor, and sometimes grew intragranularly. Work at Sector 2 of the APS has measured crack opening in aluminum cylinders under various stresses, also with tomography [75]. Because aluminum and magnesium are a couple orders of magnitude more x-ray transparent than nickel-base superalloys, rapid imaging of thicker, cylindrical samples is more feasible for these light elements. However, the cyclic test were paused for each tomographic rotation in these studies, yielding images that were not truly obtained in real-time.

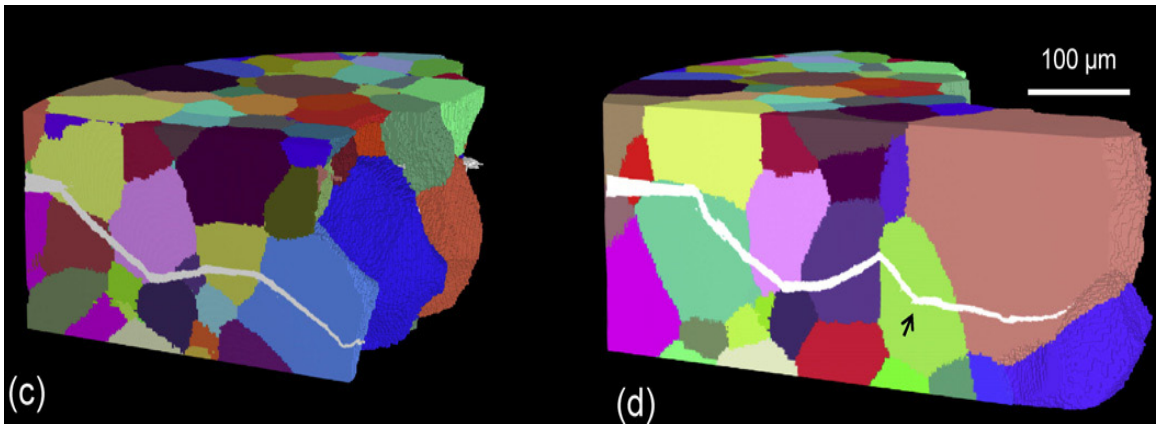


Fig. 1.11. 3D rendition of a fatigue crack in heat-treated aluminum after 75,500 cycles. (c,d) Cuts along different planes showing grain orientation and fatigue crack from notch (white). The crack usually shifted direction at grain boundaries, but also occasionally within grains (black arrow in (d)). Adapted from [21].

## 1.5 Organization of the Dissertation

The objective of this dissertation was to use phase-contrast-enhanced x-ray radiography to study superalloy microstructure and crack propagation in the high-cycle-fatigue regime. To explore this, the dissertation is organized as follows:

Chapter 2 discusses the fabrication and compositional details of the nickel-base superalloys, as well as the experimental setup involving the two emergent tools in this work: the ultrasonic fatigue apparatus and synchrotron radiography.

Chapter 3 concentrates on the principles of x-ray PCI. In addition to the familiar absorption contrast, phase and diffraction contrast will be discussed. Since the use of phase contrast to image unopened cracks is particularly novel, the focus will be on that particular contrast mechanism. The use of diffraction in a transmission radiography setup is also somewhat unconventional and will also be addressed in detail.

Chapter 4 focuses on applying the contrast mechanisms of Chapter 3 to studies of the superalloy microstructure in a static, stress-free environment. Together, the three primary contrast mechanisms provide a wealth of information, including composition maps, mosaicity information, and dislocation densities [32].

Chapter 5 deals with fatigue-crack propagation at room temperature. Detailed image sequences show micron-scale crack growth along crystallographic planes.

Absorption contrast provides details about crack opening and microstructure, but the finer details about crack position and interior fracture-surface roughness come from phase contrast. Finite element analysis confirms many of these observations.

Chapter 6 addresses some specific applications of this imaging to high-temperature crack propagation, measurements of crack-growth rates, and early-stage crack initiation. Diffraction contrast identifies qualitatively the strain and plastic zone ahead of the crack tip to anticipate the propagation path, and it provides a potential procedure for detecting crack initiation before a physical separation occurs.

Chapter 7 summarizes the results and poses some future directions for this work, including different materials to test and technological advances in x-ray sources and detectors.

## 1.6 References


1 Röntgen, W. C. On a new kind of rays. *Nature* **53**, (1896).

2 Fitzgerald, R. Phase-sensitive x-ray imaging. *Phys Today* **53**, (2000).

3 Zernike, F. How I Discovered Phase Contrast. *Science* **121**, (1955).

4 Snigirev, A., Snigireva, I., Kohn, V., Kuznetsov, S. & Schelokov, I. On the possibilities of x-ray phase contrast microimaging by coherent high-energy synchrotron radiation. *Rev Sci Instrum* **66**, (1995).

5 Nugent, K. A., Gureyev, T. E., Cookson, D. F., Paganin, D. & Barnea, Z. Quantitative phase imaging using hard x rays. *Phys Rev Lett* **77**, (1996).

6 Wilkins, S. W., Gureyev, T. E., Gao, D., Pogany, A. & Stevenson, A. W. Phase-contrast imaging using polychromatic hard X-rays. *Nature* **384**, (1996).

7 Borland M. *et al. APS storage ring parameters*, <http://www.aps.anl.gov/Accelerator_Systems_Division/Accelerator_Operations_Physics/SRparameters/SRparameters.html> (2010).

8 Jackson, J. D. *Classical electrodynamics*. (Wiley, 1999).

9 Michette, A. G. & Buckley, C. J. *X-ray science and technology*. (Institute of Physics Pub., 1993).

10 Cullity, B. D. & Stock, S. R. *Elements of x-ray diffraction*. (Prentice Hall, 2001).

11 Advanced Photon Source at Argonne National Laboratory. *Insertion devices and brilliance*, <http://www.aps.anl.gov/About/APS_Overview/insertion_devices.html> (

12 Chapman, D. *et al.* Diffraction enhanced x-ray imaging. *Phys Med Biol* **42**, (1997).

13 Cloetens, P., Barrett, R., Baruchel, J., Guigay, J. P. & Schlenker, M. Phase objects in synchrotron radiation hard x-ray imaging. *J Phys D Appl Phys* **29**, (1996).

14 Pogany, A., Gao, D. & Wilkins, S. W. Contrast and resolution in imaging with a microfocus x-ray source. *Rev Sci Instrum* **68**, (1997).

15 Arfelli, F. *et al.* Mammography with synchrotron radiation: Phase-detection techniques. *Radiology* **215**, (2000).
16 Socha, J. J., Westneat, M. W., Harrison, J. F., Waters, J. S. & Lee, W. K. Real-time phase-contrast x-ray imaging: a new technique for the study of animal form and function. *Bmc Biol* **5**, (2007).
17 Socha, J. J. *et al.* Correlated patterns of tracheal compression and convective gas exchange in a carabid beetle. *J Exp Biol* **211**, (2008).
18 Wang, Y. J. *et al.* Ultrafast X-ray study of dense-liquid-jet flow dynamics using structure-tracking velocimetry. *Nat Phys* **4**, (2008).
19 Fezzaa, K. & Wang, Y. J. Ultrafast X-ray phase-contrast imaging of the initial coalescence phase of two water droplets. *Phys Rev Lett* **100**, (2008).
20 Ludwig, W. *et al.* New opportunities for 3D materials science of polycrystalline materials at the micrometre lengthscale by combined use of X-ray diffraction and X-ray imaging. *Mater Sci Eng A* **524**, (2009).
21 Herbig, M. *et al.* 3-D growth of a short fatigue crack within a polycrystalline microstructure studied using combined diffraction and phase-contrast X-ray tomography. *Acta Mater* **59**, (2011).
22 Ignatiev, K. I., Lee, W. K., Fezzaa, K. & Stock, S. R. Phase contrast stereometry: fatigue crack mapping in three dimensions. *Philos Mag* **85**, (2005).
23 Cloetens, P. *et al.* Observation of microstructure and damage in materials by phase sensitive radiography and tomography. *J Appl Phys* **81**, (1997).
24 Shyam A., T. C. J., Jha S.K., Larsen J.M., Canton M.J., Szczepanski C.J., Pollock T.M., Jones J.W. Superalloys 2004. (2006).
25 Pollock, T. M. & Tin, S. Nickel-based superalloys for advanced turbine engines: Chemistry, microstructure, and properties. *J Propul Power* **22**, (2006).
26 Pollock, T. M. & Argon, A. S. Creep Resistance of CMSX-3 Nickel-Base Superalloy Single-Crystals. *Acta Metall Mater* **41**, (1993).
27 Pollock, T. M. & Field, R. D. Dislocations and high-temperature plastic deformation of superalloy single crystals. *Dislocations in Solids* **11**, (2002).
28 Tin, S. & Pollock, T. M. Phase instabilities and carbon additions in single-crystal nickel-base superalloys. *Mater Sci Eng A* **348**, (2003).
29 Versnyder, F. L. & Shank, M. E. Development of Columnar Grain and Single Crystal High Temperature Materials through Directional Solidification. *Mater Sci Eng* **6**, (1970).
30 Tin, S., Pollock, T. M. & Murphy, W. Stabilization of thermosolutal convective instabilities in Ni-based single-crystal superalloys: Carbon additions and freckle formation. *Metall Mater Trans A* **32**, (2001).
31 Giamei, A. F. & Tschinkel, J. G. Liquid-Metal Cooling - New Solidification Technique. *Metall Trans A* **7**, (1976).
32 Husseini, N. S. *et al.* Mapping single-crystal dendritic microstructure and defects in nickel-base superalloys with synchrotron radiation. *Acta Mater* **56**, (2008).
33 Warren, J. A. & Boettinger, W. J. Prediction of Dendritic Growth and Microsegregation Patterns in a Binary Alloy Using the Phase-Field Method. *Acta Metall Mater* **43**, (1995).

34 Pollock, T. M. & Murphy, W. H. The breakdown of single-crystal solidification in high refractory nickel-base alloys. *Metall Mater Trans A* **27**, (1996).
35 Mullins, W. W. & Sekerka, R. F. Stability of planar interface during solidication of dilute binary alloy. *J Appl Phys* **35**, (1964).
36 General Electric Company, Fairfield, CT.
37 Schijve, J. *Fatigue of Structures and Materials*. 2nd edn, (Springer, 2009).
38 Withey, P. A. Fatigue failure of the de Havilland Comet I. *Eng Fail Anal* **4**, (1997).
39 Loss of control and impact with Pacific Ocean Alaska Airlines Flight 261: McDonnell Douglas MD-83, N963AS, about 2.7 miles north of Anacapa Island, California, January 31, 2000, Washington, D.C.
40 Nicholas, T. *High Cycle Fatigue: A Mechanics of Materials Perspective*. (Elsevier, 2006).
41 Liu, L. *et al.* In situ imaging of high cycle fatigue crack growth in single crystal nickel-base superalloys by synchrotron X-radiation. *J Eng Mater Technol* **130**, (2008).
42 Allison, J. E., Jones J.W., Larsen J.M., Ritchie R. *Proceedings of the Fourth International Conference on Very High Cycle Fatigue*. (TMS, 2007).
43 Propulsion Directorate, AFRL/WPAFB. *High cycle fatigue (HCF) science and technology program 1999 annual report*. (Dayton, OH, 2000).
44 Mayer, H. Fatigue crack growth and threshold measurements at very high frequencies. *Int Mater Rev* **44**, (1999).
45 Srivatsan, T. S., Anand, S., Sriram, S. & Vasudevan, V. K. The high-cycle fatigue and fracture behavior of aluminum alloy 7055. *Mat Sci Eng a-Struct* **281**, (2000).
46 Yi, J. Z., Torbet, C. J., Feng, Q., Pollock, T. M. & Jones, J. W. Ultrasonic fatigue of a single crystal Ni-base superalloy at 1000 °C. *Mater Sci Eng A* **443**, (2007).
47 Szczepanski, C. J., Jha, S. K., Larsen, J. M. & Jones, J. W. Microstructural Influences on Very-High-Cycle Fatigue-Crack Initiation in Ti-6246. *Metall Mater Trans A* **39**, (2008).
48 Miao, J. S., Pollock, T. M. & Jones, J. W. Crystallographic fatigue crack initiation in nickel-based superalloy Rene 88DT at elevated temperature. *Acta Mater* **57**, (2009).
49 Ritchie, R. O., Davidson, D. L., Boyce, B. L., Campbell, J. P. & Roder, O. High-cycle fatigue of Ti-6Al-4V. *Fatigue Fract Eng M* **22**, (1999).
50 Papakyriacou, M., Mayer, H., Fuchs, U., Stanzl-Tschegg, S. E. & Wei, R. P. Influence of atmospheric moisture on slow fatigue crack growth at ultrasonic frequency in aluminium and magnesium alloys. *Fatigue Fract Eng M* **25**, (2002).
51 Lukas, P. & Kunz, L. Specific features of high-cycle and ultra-high-cycle fatigue. *Fatigue Fract Eng M* **25**, (2002).
52 Lamm, M. & Singer, R. F. The effect of casting conditions on the high-cycle fatigue properties of the single-crystal nickel-base superalloy PWA 1483. *Metall Mater Trans A* **38**, (2007).
53 Miao, J., Pollock, T. M. & Wayne Jones, J. Microstructural extremes and the transition from fatigue crack initiation to small crack growth in a polycrystalline nickel-base superalloy. *Acta Mater* **60**, (2012).

54 Chan, K. S., Hack, J. E. & Leverant, G. R. Fatigue Crack-Growth in Mar-M200 Single-Crystals. *Metall Trans A* **18**, (1987).
55 Wang, Q. Y., Bathias, C., Kawagoishi, N. & Chen, Q. Effect of inclusion on subsurface crack initiation and gigacycle fatigue strength. *Int J Fatigue* **24**, (2002).
56 Suresh, S. *Fatigue of Materials*. 1st edn, (Cambridge University Press, 1991).
57 Zimmermann, M. Diversity of damage evolution during cyclic loading at very high numbers of cycles. *Int Mater Rev* **57**, (2012).
58 Paris, P. C., Erdogan F. A critical analysis of crack propagation laws. *J Basic Eng*, (1963).
59 Liu, L. *et al.* In situ synchrotron x-ray imaging of high-cycle fatigue crack propagation in single-crystal nickel-base alloys. *Acta Mater* **59**, (2011).
60 Chan, K. S., Feiger, J., Lee, Y. D., John, R. & Hudak, S. J. Fatigue crack growth thresholds of deflected mixed-mode cracks in PWA1484. *J Eng Mater Technol* **127**, (2005).
61 Telesman, J. & Ghosn, L. J. Fatigue crack growth behavior of PWA 1484 single crystal superalloy at elevated temperatures. *Journal of Engineering for Gas Turbines and Power* **118**, (1996).
62 Nicholas, T. Critical issues in high cycle fatigue. *Int J Fatigue* **21**, (1999).
63 Boyce, B. L., Chen, X., Peters, J. O., Hutchinson, J. W. & Ritchie, R. O. Mechanical relaxation of localized residual stresses associated with foreign object damage. *Mater Sci Eng A* **349**, (2003).
64 Napolitano, R. E. & Schaefer, R. J. The convergence-fault mechanism for low-angle boundary formation in single-crystal castings. *J Mater Sci* **35**, (2000).
65 Bellet, D., Bastie, P. & Baruchel, J. White Beam Synchrotron Topography and Gamma-Ray Diffractometry Characterization of the Crystalline Quality of Single-Grain Superalloys - Influence of the Solidification Conditions. *J Phys D Appl Phys* **26**, (1993).
66 Bruno, G., Schumacher, G., Pinto, H. C. & Schulze, C. Measurement of the lattice misfit of the nickel-base superalloy SC16 by high-energy synchrotron radiation. *Metall Mater Trans A* **34**, (2003).
67 Royer, A., Bastie, P. & Veron, M. In situ determination of gamma' phase volume fraction and of relations between lattice parameters and precipitate morphology in Ni-based single crystal superalloy. *Acta Mater* **46**, (1998).
68 Biermann, H. *et al.* Determination of local strains in a monocrystalline turbine blade by microbeam X-ray diffraction with synchrotron radiation. *Acta Mater* **48**, (2000).
69 Robertson, S. W., Mehta, A., Pelton, A. R. & Ritchie, R. O. Evolution of crack-tip transformation zones in superelastic Nitinol subjected to in situ fatigue: A fracture mechanics and synchrotron X-ray microdiffraction analysis. *Acta Mater* **55**, (2007).
70 Korsunsky, A. M. *et al.* Crack tip deformation fields and fatigue crack growth rates in Ti-6Al-4V. *Int J Fatigue* **31**, (2009).

71 Haase, J. D., Guvenilir, A., Witt, J. R., Langoy, M. A. & Stock, S. R. Microtexture, asperities, and crack deflection in Al-Li 2090 T8E41. *Am Soc Test Mater* **1359**, (1999).

72 Ferrie, E., Buffiere, J. Y., Ludwig, W., Gravouil, A. & Edwards, L. Fatigue crack propagation: In situ visualization using X-ray microtomography and 3D simulation using the extended finite element method. *Acta Mater* **54**, (2006).

73 Buffiere, J. Y., Maire, E., Adrien, J., Masse, J. P. & Boller, E. In Situ Experiments with X ray Tomography: an Attractive Tool for Experimental Mechanics. *Exp Mech* **50**, (2010).

74 Toda, H. *et al.* A 3D measurement procedure for internal local crack driving forces via synchrotron X-ray microtomography. *Acta Mater* **52**, (2004).

75 Williams, J. J. *et al.* On the Correlation Between Fatigue Striation Spacing and Crack Growth Rate: A Three-Dimensional X-ray Synchrotron Tomography Study. *Mater Sci Eng A* **42**, (2011).

# CHAPTER 2

# EXPERIMENTAL SETUP

## 2.1 Superalloy Fabrication

Single-crystal nickel-base superalloy samples of René N4 [1], René N5 [1], and CMSX-4 [2] (Table 2.1) were directionally solidified along the [001] crystallographic axis by withdrawing a ceramic investment mold downward through a radiation baffle in a Bridgman-type high-temperature furnace [3-5], forming cylindrical bars. This was done by the Pollock research group, formerly located at the University of Michigan, Ann Arbor. Thermal gradients and withdrawal rates were approximately 40°C/cm and 20 cm/hour, respectively, resulting in a dendritic structure with primary dendrite arm spacings (PDAS) [6] of around 200-400 μm (Fig. 2.1a). Some samples of René N5 were solidified via the liquid-metal-cooling process (LMC): instead of a radiation baffle, they were withdrawn into liquid tin at 76 cm/hour with cooling rates approximately 1.5 to 7.5 times greater than in the Bridgman method [4,7]. This method formed a finer dendritic structure with a smaller PDAS of around 150 μm (Fig. 2.1b).

Table 2.1. Compositions in weight (wt.%) and atomic (at.%) percent for the dendritic regions of the three superalloys used in this work [4]. In the interdendritic region, the concentration of Ni is less and other elements' concentrations fluctuate.

| | René N4 | | René N5 | | CMSX-4 | |
|---|---|---|---|---|---|---|
| **Element** | **Wt.%** | **At.%** | **Wt.%** | **At.%** | **Wt.%** | **At.%** |
| Ni | 65.50 | 62.66 | 63.09 | 64.50 | 61.70 | 63.76 |
| Al | 4.20 | 9.23 | 6.20 | 13.55 | 5.60 | 12.59 |
| C | 0.05 | 0.25 | 0.05 | 2.45 | - | - |
| Co | 7.50 | 7.55 | 7.50 | 7.50 | 9.00 | 9.26 |
| Cr | 9.80 | 11.18 | 7.00 | 7.94 | 6.50 | 7.58 |
| Hf | 0.15 | 0.05 | 0.15 | 0.05 | 0.10 | 0.03 |
| Mo | 1.50 | 0.93 | 1.50 | 0.92 | 0.60 | 0.38 |
| Nb | 0.50 | 0.31 | - | - | - | - |
| Re | - | - | 3.00 | 0.95 | 3.00 | 0.98 |
| Ta | 4.80 | 1.57 | 6.50 | 2.12 | 6.50 | 2.18 |
| Ti | 3.50 | 4.34 | - | - | 1.00 | 1.27 |
| W | 6.00 | 1.94 | 5.00 | 1.60 | 6.00 | 1.98 |
| Y | - | - | 0.01 | 0.01 | - | - |

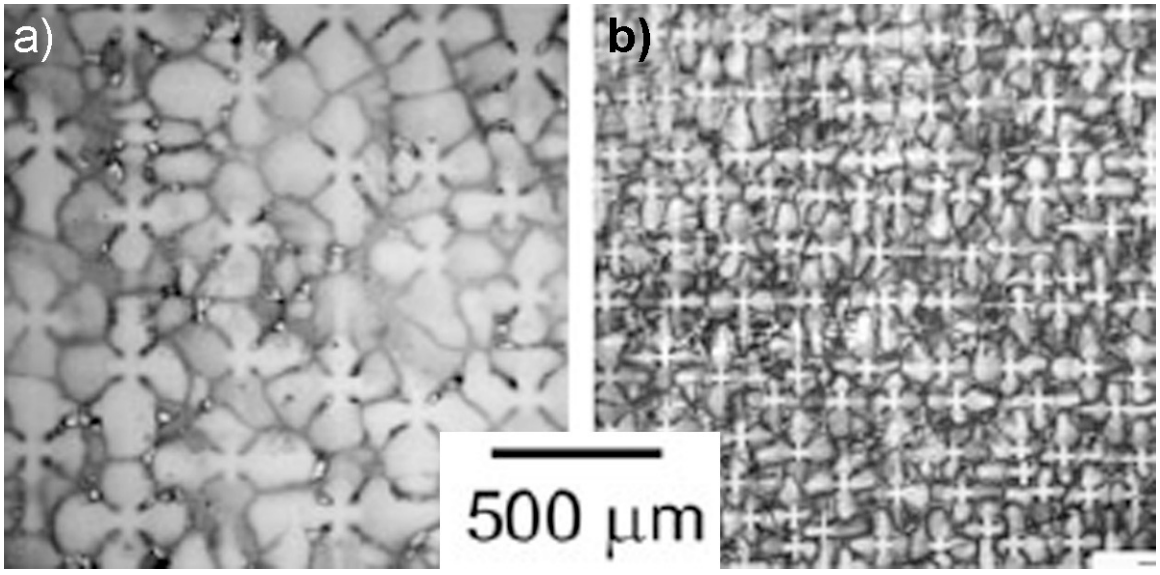


Fig. 2.1. Optical images of dendrites for (a) Bridgman-solidified sample withdrawn at 20 cm/hour and (b) LMC-solidified sample withdrawn at 76 cm/hour. Samples were cut perpendicular to the solidification axis [7].

For static imaging (Chapter 4), René N5 bars were cut both parallel and perpendicular to the [001] direction by electrodischarge machining (EDM) into 2 mm by 2 mm square coupons. Then, they were hand ground and polished to a mirror finish

with various thicknesses between 100 µm and 150 µm; a few thicker samples, up to 300 µm, were also prepared. For fatigue studies (Chapters 5 and 6), samples were cut by EDM into dogbone shapes 2-mm wide at the thinnest part of the gauge section, and ground and polished to a mirror finish with thicknesses between 150 µm and 250 µm (Fig. 2). These thicknesses were used in both studies so that only one or two dendrites were present in the through-thickness direction; otherwise, x-ray radiographs would be complicated by the projection of multiple dendrites onto the imaging plane. Also, in-plane mean stresses dominated, and out-of-plane mean stresses could be neglected.

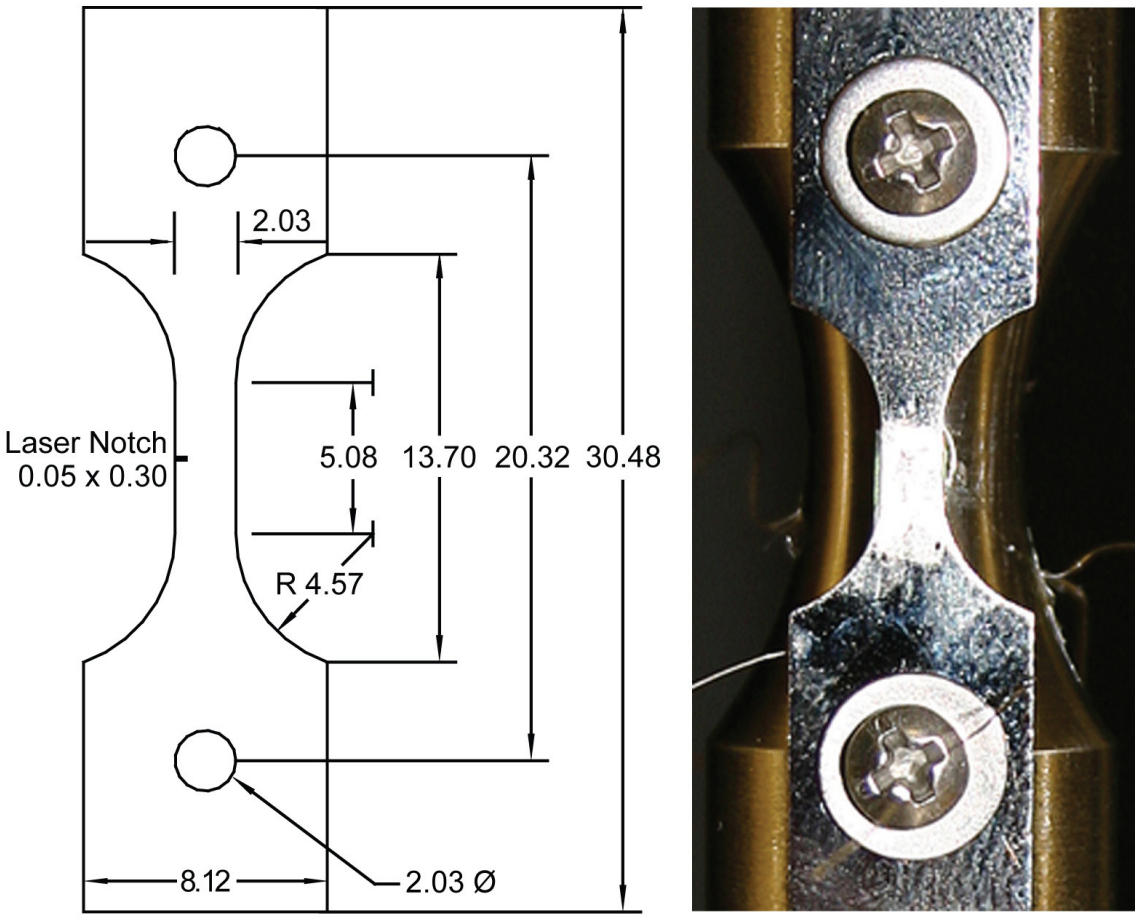


Fig. 2.2. Schematic and picture of a superalloy microspecimen used for fatigue testing. All dimensions are in mm. Sample thickness is between 150 µm and 250 µm. Schematic based on work by Christopher J. Torbet, and sample image courtesy of Dr. J. W. Jones.

Microspecimens for fatigue studies were notched with a Clark MXR CPA-2001 laser [8], which removed approximately 50 to 500 nm of material per 150-femtosecond

pulse. Femtosecond-laser machining produces very little collateral damage or residual strain [9]. The stress concentration at the end of the notch was much higher than anywhere else; thus, fatigue cracks initiated sooner and from a known location.

## 2.2 Ultrasonic Fatigue Apparatus

The ultrasonic fatigue apparatus used in these experiments was specifically designed by Christopher J. Torbet and coworkers for *in situ* radiography at a synchrotron source [10]. It combines a piezoelectric ultrasonic transducer for 20 kHz fatigue cycles and a hydraulic system to apply a mean load for testing at a variety of stresses, all in a compact and portable chassis that can be operated remotely from outside a synchrotron hutch. All fatigue tests were displacement-controlled rather than strain- or stress-controlled.

The ultrasonic transducer, amplification horn, lambda rod, and specimen form an ultrasonic fatigue system (Fig. 2.3) developed at the Universität für Bodenkultur (BOKU) in Vienna, Austria [11]. The transducer injected sinusoidal displacement waves at approximately 20 kHz through the lambda rod and into the amplification horn, where they were amplified. Larger waves traveled through a cylindrical sample, whose exact dimensions depended on the material being tested. The wave traveled through another lambda rod to a free end, whereupon it reflected back through to the transducer. Each component's vertical length was machined precisely based on its density and elastic modulus to be exactly half the wavelength of the displacement pulses. If the frequency of the sound waves matched the resonance condition of the mechanical system, the initial and reflected waves interfered constructively, and the entire system vibrated in resonance with a displacement node (strain maximum) at the exact center of the sample (Fig. 2.3b). The ultrasonic transducer self-corrected for small deviations from resonance using a sensor located after the amplification horn: it detected erroneous linear displacements and accordingly made minor corrections to the frequency of the pulse train.

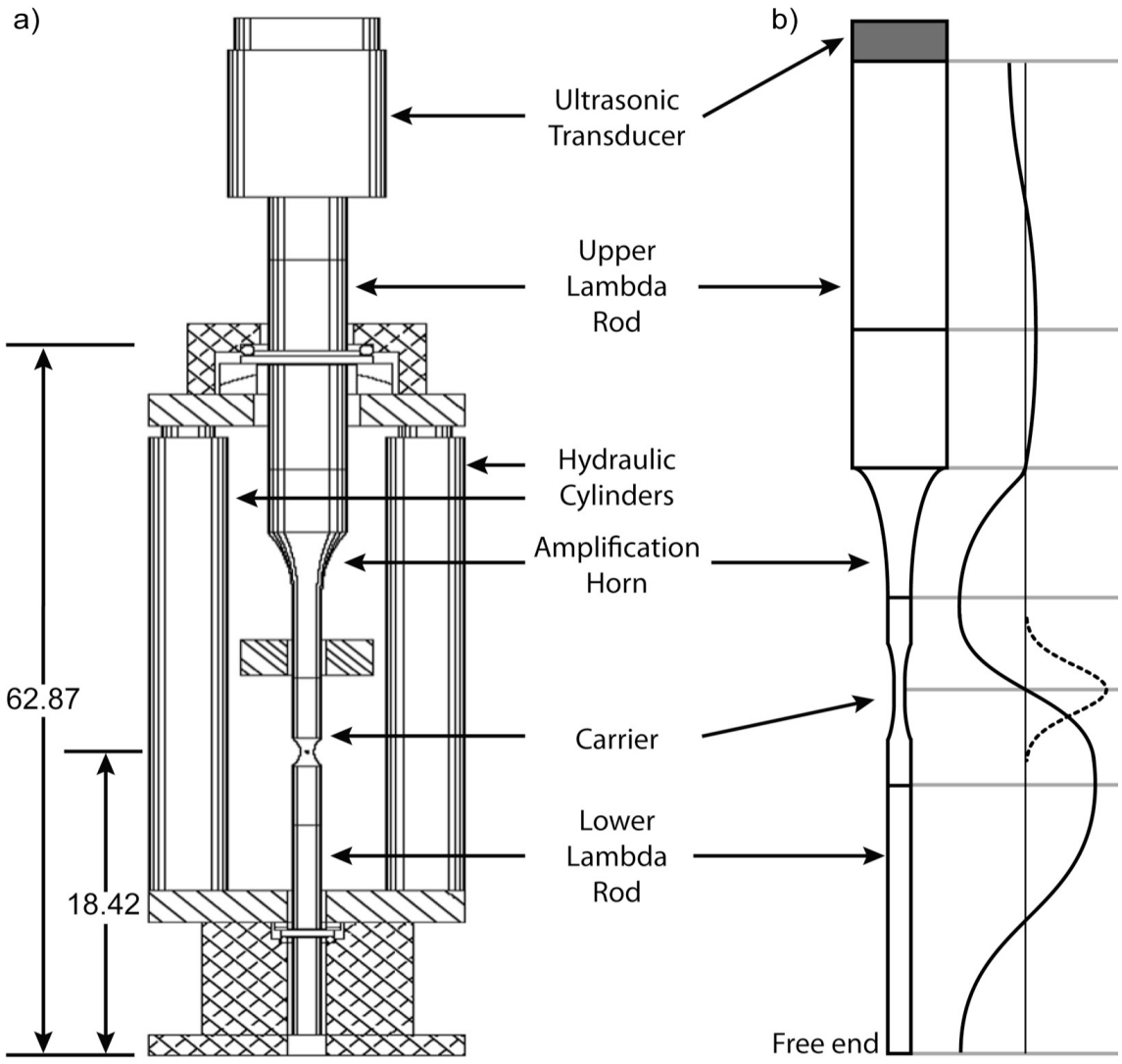


Fig. 2.3. (a) Ultrasonic fatigue apparatus with important components labeled (adapted from [12]). All dimensions are in mm. (b) Close-up of the central rod is shown on the right with a representative plot of the longitudinal-wave displacement. Strain in the carrier is shown by a dotted line with a maximum at the center of the carrier.

The sample must be cylindrical to propagate the displacement waves and maintain the resonance condition throughout the central rod; thus, a thin dogbone-shaped sample could not be mounted directly between the lambda rods. Instead, the superalloy microspecimen was rigidly screwed to a much thicker Ti-6Al-4V cylindrical carrier, whose dimensions were precisely determined by the Young's modulus and density. The two components vibrated together as one unit. With this mounting scheme, the microspecimen could have any composition or reasonable dimensions,

provided it did not interfere with resonance conditions of the carrier. A 2-mm hole was machined through the center of the carrier to prevent attenuation of the transmitted x-ray beam by anything but the specimen. Finite element analysis (FEA) showed that the stress maximum occurred in the gauge section of the microspecimen, and this stress was approximately 20% larger than in the corresponding section of the carrier (Fig. 2.4) [10]. Therefore, the carrier was therefore unlikely to fail before the microspecimen.

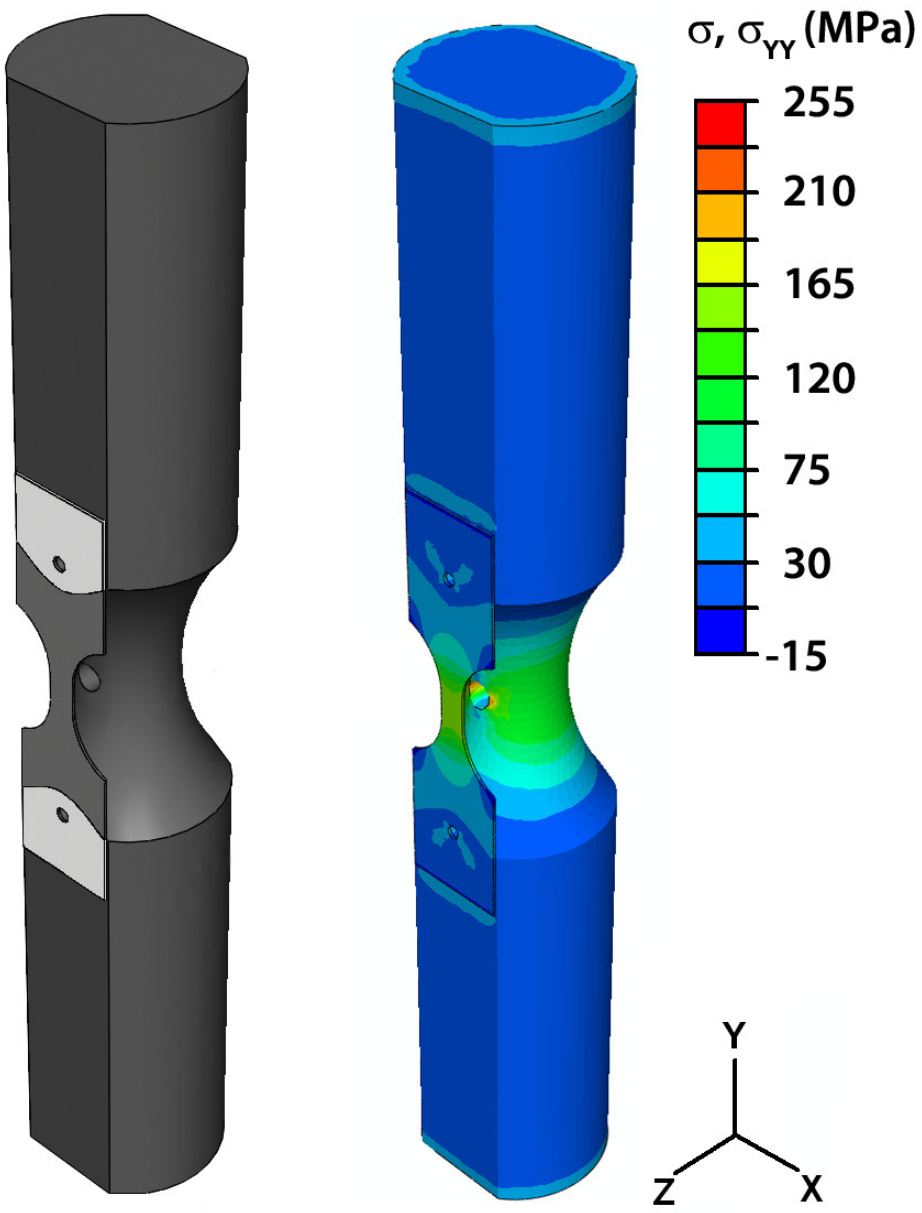


Fig. 2.4. FEA results for $\sigma_{yy}$ stress fields (MPa) within around a representative superalloy sample and the Ti-6Al-4V carrier [12].

The setup also included two hydraulic cylinders with a combined load capacity of 22 kN to supply a mean tensile stress to the sample/carrier unit, typically between 40 and 80 MPa. They were connected to the central rod at displacement nodes at the midpoints of the upper and lower lambda rod. This allowed testing at a variety of different stress ratios, $R$, defined as $\sigma_{min}/\sigma_{max}$. All tests in these studies were performed at $R$ = 0.1 (tension-tension) to prevent buckling, with typical minimum and maximum strains on the microspecimen of around 50 με and 550 με, respectively, where 1 με = $(10^{-6})$*ε.

A small furnace was placed next to the sample for high-temperature studies up to 600°C. Compressed air was heated in an alumina heater and expelled onto the sample, providing a temperature stable to within a few degrees centigrade. For even higher temperatures, a small oxyhydrogen microtorch [13] was aligned parallel to the microspecimen surface at the gauge section (Fig. 2.5). An induction coil was not used to heat the sample, because it could block the x-ray beam and also unnecessarily heat the carrier, decreasing its useable lifetime and affecting the resonance condition. The heat from the flame was tightly confined so that only the specimen and not the carrier was heated; the minor refractive-index changes from the heated air did not affect the x rays enough to see any change on the radiographs. The temperature was controlled by adjusting the torch's proximity to the surface, but since it was well above the melting point of the superalloy, the flame was never in direct contact with the sample. An infrared pyrometer focused at the center of the microspecimen monitored the temperature, which fluctuated by no more than ±10°C over a period of minutes and was uniform across the gauge length.

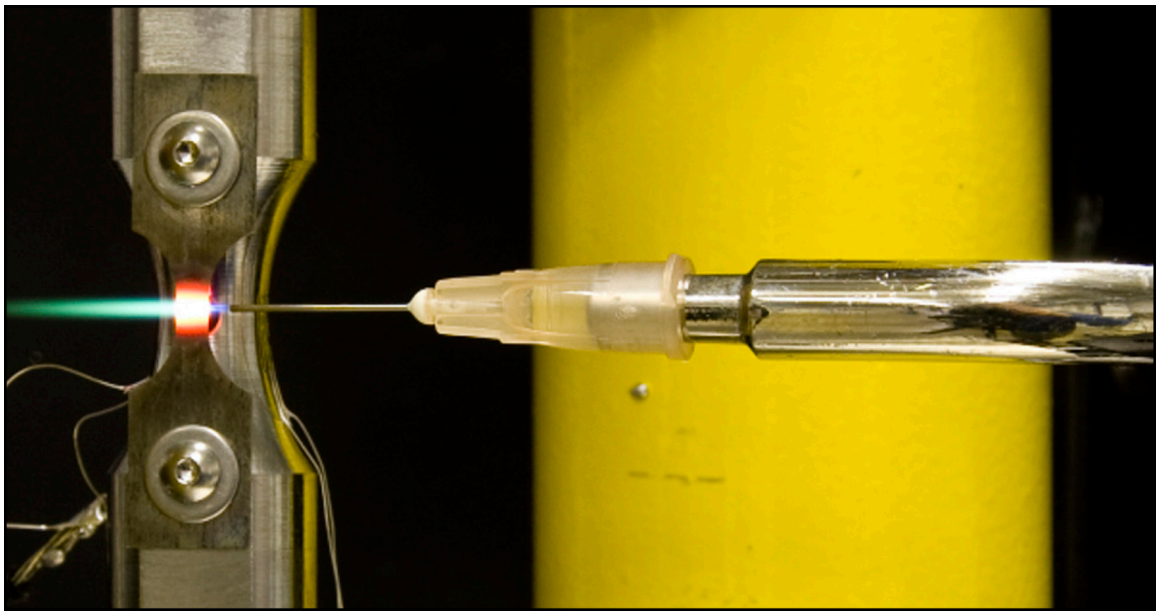

Fig. 2.5. Oxyhydrogen microtorch heating the gauge section of a microspecimen. Image courtesy of Dr. J. W. Jones.

## 2.3 Synchrotron Setup

All synchrotron work was performed at the Advanced Photon Source (APS) at Argonne National Laboratory. Static imaging, reported in Chapter 4, was performed at Sector 7-ID-C with 8.3 keV x-ray radiation. After completing this work, Sector 32-ID-C, a dedicated phase-contrast imaging beamline with specialized equipment and support staff [14], was commissioned and began accepting general-user proposals. Ultrasonic-fatigue imaging from Chapters 5 and 6 were performed at this beamline with 23 keV x-ray radiation.

### 2.3.1 Static Superalloy Imaging

Superalloy samples were mounted in transmission geometry at Sector 7-ID-C (Fig. 2.6) for static phase-contrast imaging. Very high x-ray brilliance between 6 keV and 14 keV was provided from the first harmonic of an APS type-A undulator. The x-ray photon energy was tuned by a liquid-nitrogen-cooled silicon (111) double-crystal monochromator with an energy bandwidth of $\Delta E/E \approx 10^{-4}$ and a flux of approximately $10^{12}$ photons/sec/0.1% bandwidth. For most imaging, the energy was set to 8.300 keV,

just below the nickel $K_\alpha$ edge of 8.333 keV. The second crystal of the monochromator was detuned to suppress higher-order odd-numbered harmonics, but no harmonic-rejection mirror was used. The radiation was temporally coherent for diffraction contrast and partially spatially coherent for phase contrast. The source size during normal operations at the APS was $\sigma_x \approx 270$ µm and $\sigma_y \approx 15$ µm [15]. Though this is not an ideal point source (i.e., infinitely small), it is quite sufficient for these experiments.

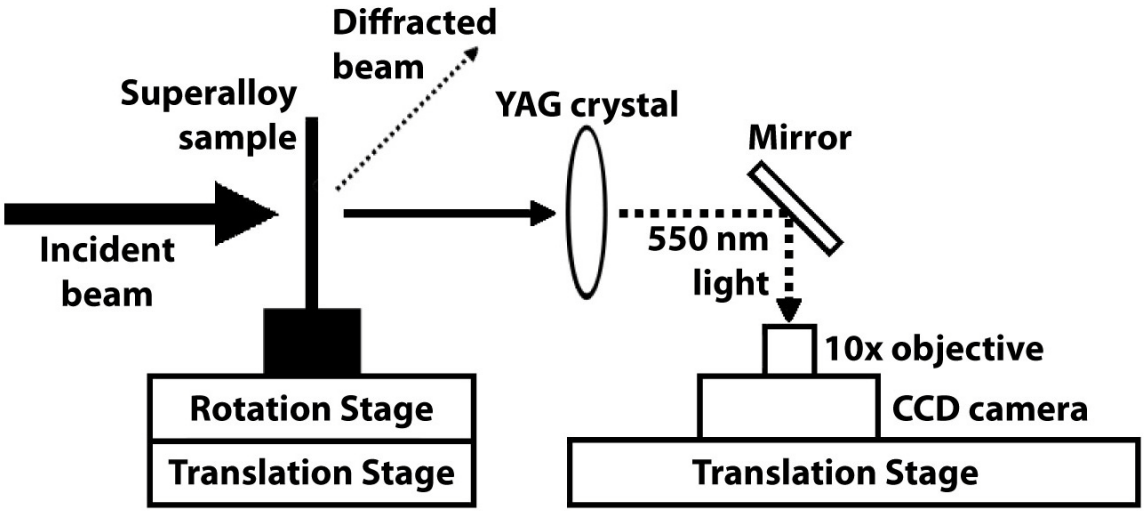


Fig. 2.6. Schematic of the static imaging setup at Sector 7-ID-C. Adapted from [16].

Superalloy coupons were attached to a post with a clip and loaded on a rotation stage atop a translation stage located approximately 65 m from the monochromator. Incident x rays traveled through an evacuated flight tube extending from the monochromator to less than a meter away from the sample. The x-ray beam propagating through the sample was attenuated according to the sample's composition and density. If a region of the sample satisfied a Bragg condition, then a portion of the beam was diffracted away from the detector assembly placed directly behind the sample, further reducing the number of transmitted photons (see Section 3.3 for more details). Beyond the sample, the x-ray beam induced fluorescence in a cerium-doped yttrium aluminum garnet (YAG:Ce) scintillator crystal. The 550-nm fluoresced light was reflected by a mirror to a 16-bit cooled charge-coupled device (CCD) camera with a 10x

objective [17]. The detector assembly was located 75 cm from the sample, which was determined experimentally to give good phase-contrast enhancement of features such as dendrites and carbides.

The x-ray beam was unfocused, though still well-collimated, for the largest possible viewing area, producing images approximately 800 μm by 500 μm in size with a spatial resolution of approximately 2 μm/pixel. These high-quality images were visible immediately, albeit with an appreciable non-uniform intensity profile that was corrected later with minor image processing in ImageJ [18] or MATLAB [19] software. Integration times were determined experimentally and depended on the sample thickness: ~0.5 seconds for 100-μm-thick samples to ~30 seconds for 300-μm-thick samples.

### 2.3.2 Fatigue-Crack Imaging

The setup for fatigue imaging at Sector 32-ID-C was similar to that for static imaging at Sector 7-ID-C with a few key differences (Fig. 2.7). Since most tests were performed with slightly thicker samples (usually around 200 μm), all imaging was done with radiation off the third-harmonic of the APS type-A undulator, tunable between 15 keV and 30 keV with $\Delta E/E \approx 10^{-4}$. The 23.000 keV photon energy was selected using a silicon (111) monochromator for a flux of approximately $10^{13}$ ph/s/0.1%bw, an order of magnitude greater than at Sector 7. This energy kept the integration times to less than a second and provided strong absorption contrast between dendritic and interdendritic regions. No harmonic-rejection mirror was used, but any higher-order harmonics, such as 38.333 keV, would pass through samples with minimal attenuation. All imaging was performed while the APS was operating in Reduced Horizontal Beta (RHB) mode, which decreased the horizontal source size by nearly half compared to normal operations to $\sigma_x \approx 120$ μm. The vertical source size at $\sigma_y \approx 15$ μm [20].

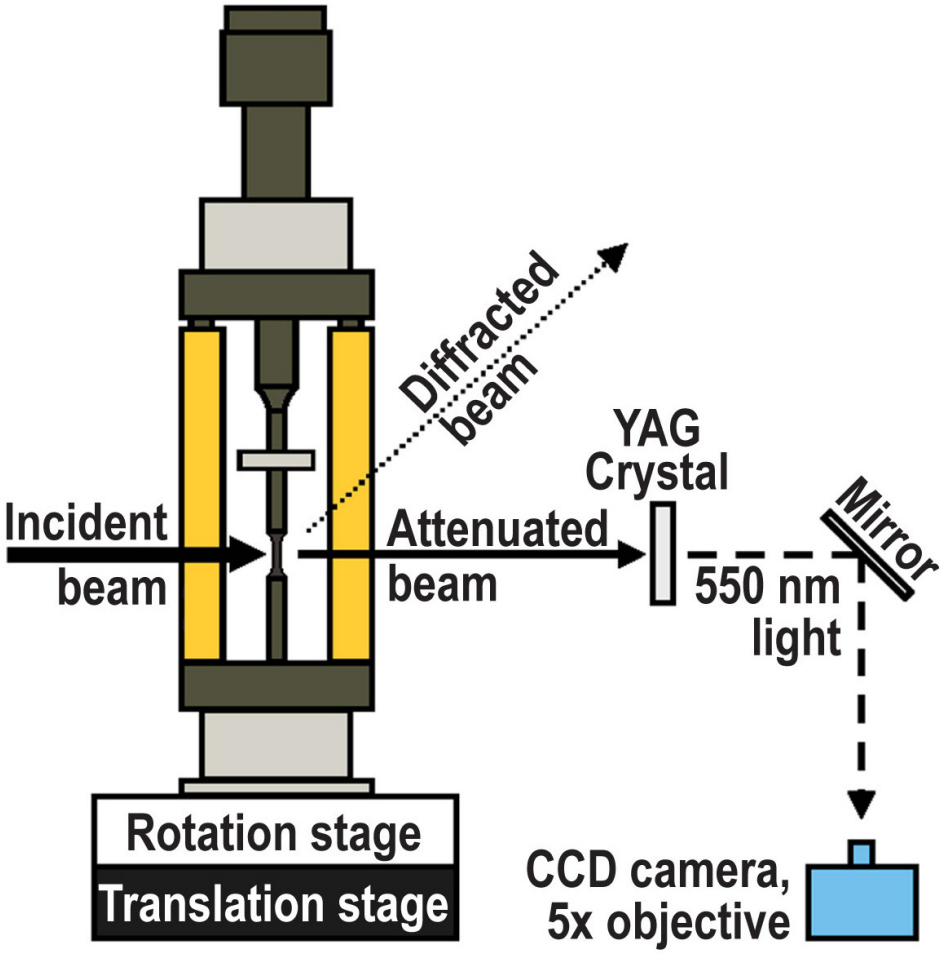


Fig. 2.7. Schematic of the ultrasonic fatigue apparatus in transmission geometry at Sector 32-ID-C.

Samples were fixed to the carrier in the ultrasonic fatigue apparatus, as described in Section 2.2, which was mounted on a rotation stage atop a translation stage located 77 m downstream from the monochromator. X rays traveled from the monochromator through an evacuated flight tube and were attenuated and diffracted as before, stimulating fluorescence in a YAG:Ce crystal located 80 cm behind the sample for optimal phase-contrast enhancement. Green light at 550 nm was imaged by a 12-bit Cooke SensiCam CCD [21] with a 5x objective for a spatial resolution of approximately 1.5 µm/pixel and field of view of about 1800 µm x 1500 µm. Again, the non-uniform beam profile was corrected with ImageJ and MATLAB. Typical exposure lengths and camera-readout times were 50-150 ms and 200 ms, respectively, for a best-case total

acquisition time of 250 ms per image and a maximum possible sampling rate of approximately 4 Hz.

## 2.4 Fatiguing Protocol

The fastest sampling rate of 4 Hz was still too slow to image multiple times along a single cycle, which would require a sampling rate greater than 80 kHz and an unfeasibly short exposure time at 23 keV for this composition and thickness. An image taken with a 50-ms exposure time during testing at 20 kHz, therefore, would superimpose 1,000 cycles worth of information**.** Though nominally at a displacement node, the minuscule changes in strain around cracks were still significant enough to cause blurring of the phase- and diffraction-contrast effects, obfuscating some of the finer details. Moreover, as cracks reached 25-50% of the gauge-section length, displacements during testing opened the crack by up to a couple microns away from the crack tip and caused the sample to bow and twist very slightly.

For temperature stability within the sample and maximum image quality, we introduced a pulsed loading regime with a 10-25% duty cycle and imaged during the rest periods (Fig. 2.8). The ultrasonic transducer produced transistor-transistor logic (TTL) wave output at the beginning of each pulse phase to a preamplifier and triggered the imaging software. Image acquisition followed a delay of 50 ms longer than the pulse duration so that exposures occurred entirely during the rest period. The duty cycle prevented excessive heating from internal friction during repeated cycling, maintaining a more constant temperature throughout testing at room temperature. The cycle-per-image rate was varied by controlling the length of the duty cycle. A typical test protocol used a 25% duty cycle when initiating cracks, which involved a 200-ms pulse with a 600-ms rest to collect images every 4,000 cycles. If the crack grew by more than a pixel (about 1.5 μm) per image, the duty cycle was reduced to 10%, or 50 ms pulse with a 450 ms pause, to take images every 1,000 cycles. Images were registered and labeled with scale bars and other information using MATLAB and then assembled into movies with ImageJ.

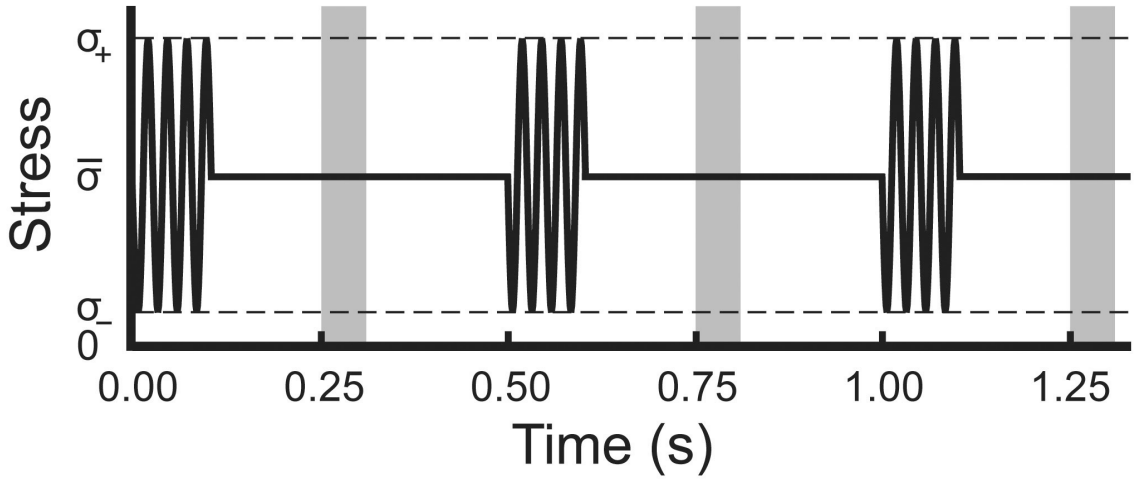


Fig. 2.8. Plot of stress versus time during testing. The duty cycle in this example is 20%, with 0.1-s pulses (2,000 cycles) every 0.5 s. The shaded regions correspond to 0.05 s exposure times during constant tensile stress. The oscillations are not to scale, with each representing 500 cycles.

The stress-intensity factor range, $\Delta K$, predicted the stress state near a crack tip or notch during loading. Since the microspecimens can be approximated initially as a horizontally-notched infinite plane, $\Delta K$ (Eq. 1.2) can be decomposed to its in-plane component, $\Delta K_I$, with $Y = 1$ for a horizontal notch:

$$\Delta K_I = \Delta\sigma\sqrt{\pi a} \qquad [2.1]$$

$\Delta\sigma$ is the stress amplitude and is directly related to the displacement amplitude applied by the ultrasonic fatigue apparatus. The stress-intensity threshold for crack initiation, $\Delta K_{th}$, is determined by a number of factors, including the superalloy composition and density, its thickness and notch length, and the ambient testing temperature. Values of $\Delta K_{th}$ were determined empirically from previous work away from the synchrotron, so that initial test parameters would not cause cracks to initiate and grow too quickly. Typical room-temperature values were between 3 and 7 MPa·m$^{1/2}$, which are consistent with thresholds found in other single-crystal superalloys [22].

Several million cycles were applied at displacement amplitudes just below $\Delta K_{th}$. If no crack initiated, the displacement amplitude was increased to cause a 20 με increase in the mean specimen strain, and then several million more cycles were applied. This

procedure was repeated until a crack initiated, after which the amplitude was kept constant. The duty cycle was decreased for a better temporal resolution if the crack grew too quickly. Cracks arrested due to microstructural features were given several million cycles to resume propagation; if they remained arrested, the displacement amplitude was raised for a corresponding increase in the specimen strain of 10 με. If at any time the amplitude limit of the system was reached and the crack remained uninitiated or arrested, $10^7$ more cycles were applied before the test was aborted.

Fatigue testing was paused periodically for rocking curves about Bragg angles for strain and misorientation information. The mean tensile stress was maintained while the sample was rotated about the vertical axis in steps of 0.005° until each dendrite diffracted strongly at least once. The sample was centered almost exactly at the axis of rotation, so that the sample experienced very little linear motion. Because of the mosaicity, the exact Bragg angle varied between dendrites [16], requiring total rotations over a few degrees, even though the Bragg peaks were typically only tenths of degrees wide or less. Diffraction studies at elevated temperatures could only be achieved using the furnace, as it provided heating stable enough for proper rocking curves. High-temperature diffraction studies with the microtorch were impossible, since even slight temperature variations caused thermal expansions and contractions significant enough to shift the Bragg conditions substantially (see Section 3.3.1).

Larger rotations for three-dimensional information could not be performed while the microspecimen was in the fatigue apparatus. The only x rays to reach the detector passed through the hole in the carrier, which provided a window of between -5° and 5° with respect to normal incidence. After all samples were tested at a particular synchrotron run, the ultrasonic fatigue apparatus was removed and samples were clipped to a pole mounted on the rotation stage, similar to that in the static-imaging setup (Fig. 2.6). Rotations were limited to extrema at -70° and 70°, where the sample thickness encountered by the x-ray beam increased by a factor of $\sec(70°) \approx 3$. Without changing the exposure time, the crack and microstructure became obscured. Additionally, at very steep angles, the 2-mm gauge section became only

$\cos(70°) \approx 0.68$ mm in the imaging plane, which was significantly smaller than the size of the detector (1.8 mm). Without the use of filters, the unattenuated x-ray produced significant light bloom at the sample edges and overwhelmed details near the sides of the sample. Because of these problems, proper tomography would require a different geometry or a less severe aspect ratio of 1:10 (0.2 mm thickness and 2.0 mm width at the gauge section).

## 2.5 References


1 General Electric Company, Fairfield, CT.

2 Cannon Muskegon Corporation, Muskegon, MI.

3 Elliott, A. J. *et al.* Directional solidification of large superalloy castings with radiation and liquid-metal cooling: A comparative assessment. *Metall Mater Trans A* **35**, (2004).

4 Pollock, T. M. & Tin, S. Nickel-based superalloys for advanced turbine engines: Chemistry, microstructure, and properties. *J Propul Power* **22**, (2006).

5 ALD Vacuum Technologies GbmH, H., Germany.

6 Kurz, W. & Fisher, D. J. *Fundamentals of solidification*. (Trans Tech Publications, 1986).

7 Brundidge, C. L., Miller, J. D. & Pollock, T. M. Development of Dendritic Structure in the Liquid-Metal-Cooled, Directional-Solidification Process. *Metall Mater Trans A* **42A**, (2011).

8 Clark-MXR, Inc., Dexter, MI.

9 Feng, Q. *et al.* Femtosecond laser micromachining of single-crystal superalloys. *Superalloys 2004*, (2004).

10 Liu, L. *et al.* In situ imaging of high cycle fatigue crack growth in single crystal nickel-base superalloys by synchrotron X-radiation. *J Eng Mater Technol* **130**, (2008).

11 Mayer, H. Fatigue crack growth and threshold measurements at very high frequencies. *Int Mater Rev* **44**, (1999).

12 Liu, L. *et al.* In situ synchrotron x-ray imaging of high-cycle fatigue crack propagation in single-crystal nickel-base alloys. *Acta Mater* **59**, (2011).

13 Okai Corportation, Union, NJ.

14 Shen, Q. *et al.* Dedicated full-field X-ray imaging beamline at Advanced Photon Source. *Nucl Instrum Meth A* **582**, (2007).

15 Borland M. *et al. APS storage ring parameters*, <http://www.aps.anl.gov/Accelerator_Systems_Division/Accelerator_Operations_Physics/SRparameters/SRparameters.html> (2010).

16 Husseini, N. S. *et al.* Mapping single-crystal dendritic microstructure and defects in nickel-base superalloys with synchrotron radiation. *Acta Mater* **56**, (2008).

17 Dufresne, E. M., Arms, D. A., Pereira, N. R., Ilinski, P. & Clarke, R. An imaging system for focusing tests of Li multiprism X-ray refractive lenses. *Synchrotron Radiation Instrumentation* **705**, (2004).
18 ImageJ, Bethesda, MA.
19 MATLAB, The MathWorks Inc., Natick, MA.
20 Fezzaa, K. Personal communication, March 8, 2012
21 Cooke Corporation, Romulus, MI.
22 Lukas, P. & Kunz, L. Specific features of high-cycle and ultra-high-cycle fatigue. *Fatigue Fract Eng Mater Struct* **25**, (2002).

## CHAPTER 3

## X-RAY IMAGING THEORY

X rays are merely high-energy electromagnetic waves, and many equations and principles well-known in classical optics and electrodynamics remain true [1]. For a monochromatic plane wave propagating in free space from a coherent, collimated source, the field, $\psi$, as a function of position, $z$, and time, $t$, is

$$\psi(z,t) = \psi_0 e^{-i(\omega t - \tilde{k}z)} \quad [3.1]$$

where $\psi_0$ is the field amplitude, $\omega$ is the frequency, and $\tilde{k}$ is the complex wavenumber. By considering Eq. 3.1 at a fixed time, the temporal component can be ignored without affecting the subsequent analysis. A familiar expression relates $\tilde{k}$ for the now-complex index of refraction, $\tilde{n}$:

$$\tilde{k} = k\tilde{n} = \frac{2\pi}{\lambda}\tilde{n} \quad [3.2]$$

Unlike in the visible part of the spectrum, the real part of $\tilde{n}$ is slightly less than 1 for x rays in media, minimizing their refraction. Thus, defining $\tilde{n}$ in terms of two positive, yet very small, dimensionless parameter – the decrement of refraction, $\delta$, and extinction coefficient, $\beta$:

$$\tilde{n} = 1 - \delta + i\beta \quad [3.3]$$

Confusingly, Eq. 3.3 is sometimes written with a minus sign instead of a plus sign before the imaginary term if Eq. 3.1 is defined instead with a positive exponential term. The convention defined in Eqs. 3.1 and 3.3 will be used throughout the dissertation. Above photon energies of 30 eV, $\tilde{n}$ can be expressed as [2]

$$\tilde{n} = 1 - \frac{r_e \lambda^2}{2\pi} \sum_i n_i (f_{i,1} - i f_{i,2}) \quad [3.4]$$

where $r_e$ is the classical electron radius, λ is the wavelength, and $n_i$ is the number of atoms of element *i* per unit volume. Atomic scattering factors $f_{1,i}$ and $f_{2,i}$ are unique to a particular element, and they are tabulated in many references (e.g., [3]) and used to determine $\delta$ and $\beta$ values. Plugging Eq. 3.2 and 3.3 into Eq. 3.1 describes an x-ray plane wave at a fixed time:

$$\psi(z) = \psi_0 e^{ikz(1-\delta+i\beta)} \quad [3.5]$$

$$\psi(z) = \underbrace{\psi_0\left[e^{ikz}\right]}_{\substack{Propagating \\ Wave}} \underbrace{\left[e^{-k\beta z}\right]}_{\substack{Absorption \\ Contrast}} \underbrace{\left[e^{-ik\delta z}\right]}_{\substack{Phase \\ Contrast}} \quad [3.6]$$

The constant and first term define a simple propagating wave, the second term is an attenuating term responsible for absorption contrast, and the final term is an oscillating phase term responsible for phase contrast. Each of these two contrast effects will be discussed independently in Sections 3.1 and 3.2, respectively. The third contrast mechanism, diffraction contrast, will be explicated in Section 3.3, though its origins are not manifest in Eq. 3.6 and must be approached differently.

### 3.1 Absorption Contrast

X rays with energies above ~10 eV are classified as ionizing radiation, because they can interact and strip electrons from atomic orbitals to create ions. A number of interactions are lumped under the umbrella of "absorption" in radiography, including photoelectric absorptions, pair production, Thomson and Rayleigh (elastic) scattering, and Compton (inelastic) scattering [4]. Scattering sends photons in all different directions, reducing the number of transmitted photons in the forward direction. At modest energies, such as the 8–23 keV energies used in these experiments, photoelectric absorption is the dominant effect and scales as $Z^3/E^3$, where *Z* is the atomic mass of the material and *E* is the incident photon energy [4]. Heavier elements, such as tantalum ($Z_{Ta}$ = 73), will attenuate x rays significantly more than comparatively lighter elements, such as nickel ($Z_{Ni}$ = 28). Compton and Thompson scattering are a couple orders of magnitude weaker in the low-keV regime than photoelectric

absorption, and pair production is only noteworthy at energies in the MeV range, so these other processes are practically negligible.

For the propagating plane wave of Eq. 3.1, the intensity is the magnitude squared of Eq. 3.6:

$$I(z) = |\psi(z)|^2 = I_0 e^{-2k\beta z} \quad [3.7]$$

Intensity has no $\delta$ dependence and can be expressed as a simple decaying exponential with the form of the Beer-Lambert Law [5]. In vacuum, $\beta$ = 0, so x rays are only attenuated when they travel through a non-vacuum medium of thickness, *T*. For that case, Eq. 3.7 can be alternately expressed in two equivalent forms:

$$I(z) = I_0 e^{-T\cdot(\mu/\rho)\cdot\rho} = I_0 e^{-T/\alpha} \quad [3.8]$$

$$\frac{4\pi}{\lambda}\beta = \left(\frac{\mu}{\rho}\right)\cdot\rho = \frac{1}{\alpha} \quad [3.9]$$

where $\rho$ is the density of the medium, $\mu/\rho$ is the mass-absorption coefficient, and $\alpha$ is the attenuation length. These last two parameters are both useful in different contexts: $\mu/\rho$ is a material constant and is independent of the state of matter, while $\alpha$ defines the thickness of a material through which x rays lose $e^{-1}$, or about 37%, of their intensity. Tables containing $\mu/\rho$ and $\alpha$ as a function of energy are readily available for elements and compounds [3,6], as no simple formulaic relationship holds for all energies. For a compound, Eq. 3.8 becomes

$$I = I_0 e^{-w_1\cdot(\mu/\rho)_1\cdot\rho\cdot T} e^{-w_2\cdot(\mu/\rho)_2\rho\cdot T} \ldots \quad [3.10]$$

$$I = I_0 \prod_i e^{-w_i\cdot(\mu/\rho)_i\cdot\rho\cdot T} \quad [3.11]$$

A compound is thus a collection of single-element slabs composed of element *i* with thicknesses scaled by the weight fractions, $w_i$. This method neglects interatomic interactions, and though it is most accurate away from absorption edges, it will still provide a reasonable estimate of the transmitted intensity [3].

Consider the attenuation of 8.3 keV x rays by two 100-µm-thick samples. One has the composition of the René N5 dendritic region given in Table 2.1 and the other with the composition of an interdendritic region. The interdendritic composition is not as well-defined as the dendritic region, though it typically has less nickel. One possible

interdendritic region has the same concentration as the dendritic regions for all elements, except less Ni (only 45%) and correspondingly more Ta [7]. The density in both regions is 8.63 g/cm$^3$ [8]. From Eq. 3.11, the transmitted intensity ratio, $I/I_0$, is 3.70 x $10^{-4}$ for the dendritic region and 7.35 x $10^{-5}$ for the interdendritic region. For the same sample at a higher energy of 23 keV, $I/I_0$ is 0.139 and 0.100 for the dendritic and interdendritic regions, respectively. Contrast is defined quantitatively as

$$C = \frac{I_{max} - I_{min}}{I_{max} + I_{min}} \quad [3.12]$$

Thus, the interregional contrast at 8.3 keV is 66.8%, while the contrast at 23 keV is 16.3%. Though weaker in contrast, the higher $I/I_0$ at higher energies means that samples can be thicker and integration times shorter. These results are summarized in Table 3.1 at the end of this section.

### 3.1.1 Absorption Edge

The absorption spectrum contains several sharp discontinuities related to photoelectric absorption that can improve the sensitivity to a particular element. These absorption edges occur where incident photon energies match the binding energies of particular core electrons, ejecting them from their energy level. For typical K-edges, this is marked by a roughly eight-fold increase in the mass-absorption coefficient immediately after the edge, or equivalent to raising the transmitted intensity ratio to the seventh power. The photon count at the detector decreases severely when moving from below to above the absorption edge [4]. The intensity change around the absorption edge provides compositional information, and this is the basis for x-ray absorption spectroscopy (XAS), which includes both extended x-ray absorption fine structure (EXAFS) and x-ray absorption near edge structure (XANES) [2].

If one element is present in some areas but absent in others, tuning the energy near its absorption edge can dramatically improve interregional contrast. In the same simulated dendrite/interdendritic case as before, Ni comprises 65% of the dendritic and 45% of the interdendritic regions. The Ni $K_\alpha$ absorption edge is at 8.333 keV, and just above, at 8.350 keV, almost all constituent elements except Al, C, and Y have a similar

attenuation length between 3 and 6 μm (Fig. 3.1). The transmitted intensity ratio $I/I_0$ is so weak ($10^{-9}$ or less) that few photons penetrate to the detector, and any contrast between regions is lost in the background noise. Below the edge at 8.300 keV, though, the attenuation length of Ni increases to 26.25 μm while the others drop slightly, and this increases the x-ray transparency of regions with more Ni compared to those with less Ni. These results are summarized in Table 3.1 later in this section.

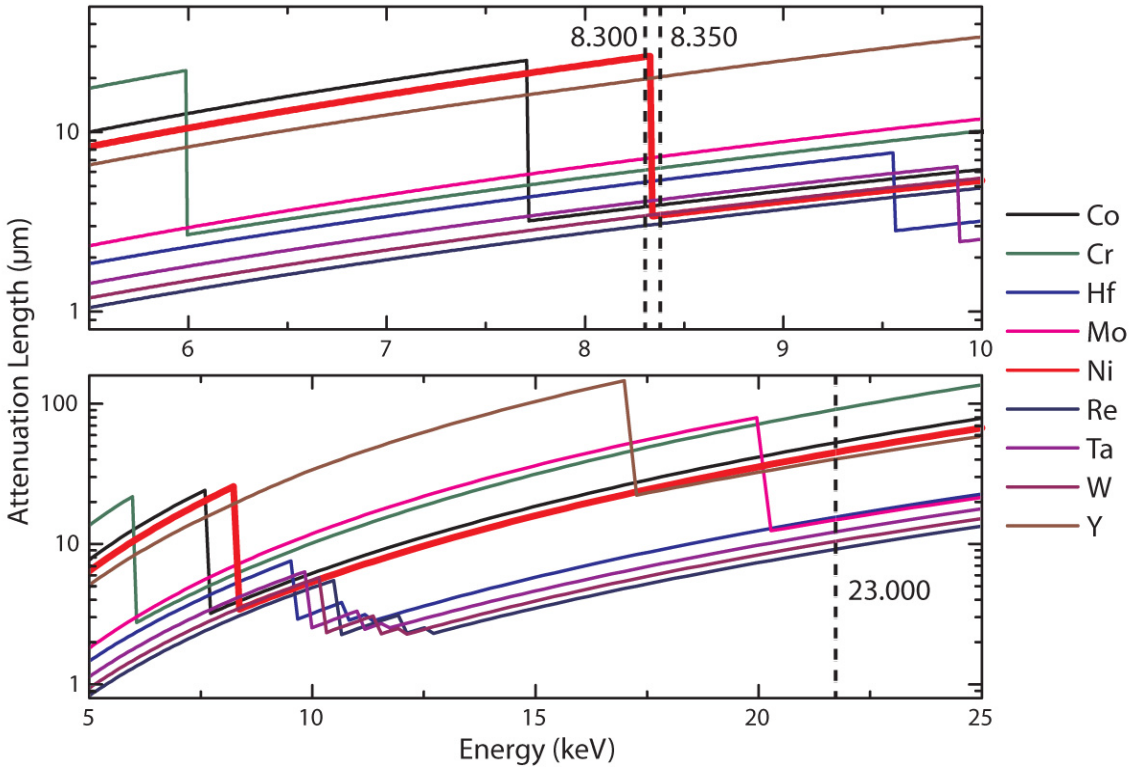


Fig. 3.1. Semilog plot of attenuation length ($\alpha$) as a function of energy. The top plot is a zoomed-in region of the bottom plot. Energies used for imaging in this work are marked with dotted lines at 8.300, 8.350, and 23.00 keV. Note the $K_\alpha$ absorption edge at 8.333 keV in the Ni curve (thick red line). Al and C are not shown, because their attenuation lengths are 10x and 100x larger than for the other elements, respectively, and would unnecessarily compress all other lines.

### 3.1.2 Crack Imaging via Absorption

Adding a crack decreases the thickness of material in the through-thickness direction, and thus the optical path length (OPL), traversed by the x-ray photons; how much depends greatly on the amount and angle of opening. Mode-I cracks (tensile stress normal to the crack plane) can open so that the OPL is 0 near the root of the crack

emanating from the notch and still less than the OPL of virgin material near the tip of a propagating crack. A small OPL of material means very little attenuation. The crack shown in Fig. 3.2 has a small degree of tortuosity and is mostly normal to the sample surface, and it can thus be easily imaged with absorption contrast alone.

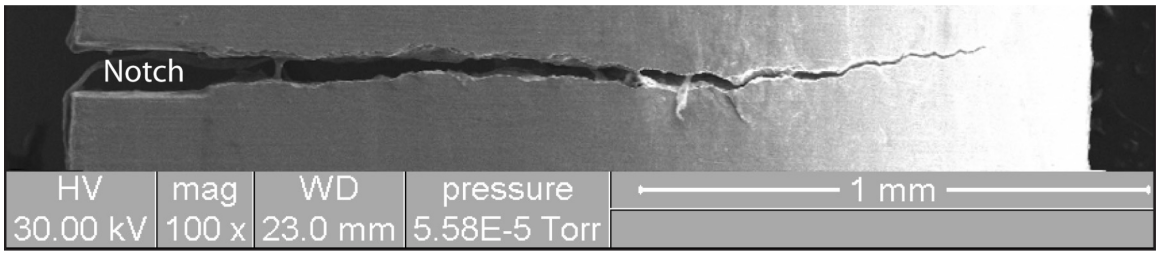


Fig. 3.2. Scanning electron micrograph of a fatigue crack grown from a notch in the polycrystalline nickel-base superalloy Haynes 282 [9]. The loading axis is vertical. Image courtesy of K. Z. Green.

Cracks in monocrystalline materials are under the influence of tensile and shear stresses and can cleave along crystallographic planes [10]. Crack opening in this case is very small and the OPL change is minuscule (see Sections 5.2 and 5.3). For example, suppose a crystallographic crack opens 0.5 μm in the 100-μm-thick René N5 example from before. It cleaves along a plane inclined 45° with respect to the x-ray beam, for a decrease in thickness as seen by the radiation of (0.5 μm)*cos(45°) ≈ 0.71 μm. Data for $I/I_0$ and the contrast at both 8.3 keV and 23 keV are shown in Table 3.1. In both cases, the contrast is very low between cracked and uncracked regions. Though appropriate for differentiating dendritic and interdendritic regions, absorption contrast alone is insufficient to image minimally opened cracks accurately, and they would be invisible without an additional contrast mechanism.

Table 3.1. Summary of $I/I_0$ ratios for uncracked dendritic and interdendritic and cracked dendritic regions at three energies in René N5. 8.333 keV is the Ni $K_\alpha$ absorption edge.

| Energy (keV) | Dendritic region | Interdendritic region | Dendritic crack | Dendrite/ interdendritic contrast (%) | Dendrite/ crack contrast (%) |
|---|---|---|---|---|---|
| **8.300** | $3.70 \times 10^{-4}$ | $7.35 \times 10^{-5}$ | $3.80 \times 10^{-4}$ | 66.8 | 1.33 |
| **8.350** | $6.99 \times 10^{-11}$ | $1.25 \times 10^{-9}$ | $7.58 \times 10^{-11}$ | n/a | n/a |
| **23.00** | $1.39 \times 10^{-1}$ | $1.00 \times 10^{-1}$ | $1.40 \times 10^{-1}$ | 16.3 | 0.358 |

## 3.2 Phase Contrast

As discussed in Chapter 1, phase-contrast imaging (PCI) was originally developed to distinguish between regions with little difference in their attenuation coefficient, the same problem encountered when locating images of minimally opened cracks in superalloys. Recall the third term of Eq. 3.6, $e^{-ik\delta z}$. For a monochromatic coherent wave propagating along the z-axis through a slab with no lateral variation (i.e., infinite length along the x- and y-axes) this term disappears when calculating the intensity even if $\delta$ is non-zero – the ubiquitous "phase problem" of x-ray science. However, for a non-uniform sample or one with some geometric variations, changes in δ cause the wave to refract slightly and interfere with unrefracted components of the same wave at the detector. The degree of refraction in the forward direction is very small (~10 μrad), so interference is strongly dependent on the sample-to-detector distance [11]. Phase contrast will be explained in more detail using the Fresnel-Kirchhoff formalism in the paraxial limit [5,12].

The lateral effects of phase contrast are explored by neglecting the propagating-wave term in Eq. 3.6 and rewriting it to include the contributions of both the real and imaginary components of the refractive index:

$$\psi(x,y,z)|_{z=z_1} = T(x,y)\cdot\psi(x,y,z)|_{z=z_0} \quad [3.13]$$

$$T(x,y) = M(x,y)e^{i\varphi(x,y)} \quad [3.14]$$

$$M(x,y) = e^{-2k\int_{z_0}^{z_1}\beta(x,y,z)dz} \quad [3.15]$$

$$\varphi(x,y) = \varphi_0 - k\int_{z_0}^{z_1}\delta(x,y,z)dz \quad [3.16]$$

$z_0$ and $z_1$ are positions along the propagation direction just before and just after the object, respectively. $T$ is the complex transmission function split into the absorption term ($M$) and the phase term ($\varphi$). The mean phase modulation of the entire wave, $\varphi_0$, does not affect the calculation of intensity, as it disappears upon squaring; it will be neglected in further calculations. The terms $\mu/\rho$ and $\delta$ are as defined before. At this point, the only assumption made is that the object is much larger than the wavelength –

easily satisfied considering the x-ray wavelengths used in this work were 1.494 Å at 8.300 keV and 0.5391 Å at 23.00 keV.

Solving these equations further without limiting assumptions is the subject of ongoing theoretical work [11,13-14]. An exact understanding of the phases and amplitudes is critical when imaging weakly absorbing objects: the detector output requires phase reconstruction before the original image can be restored from a potentially complex interference image (Fig. 3.3b). For edge-enhanced absorption radiographs (Fig. 3.3a), though, the precise phase information is not necessary. This will be explored first in a simple simulation of PCI from a slab. Then, some assumptions and their significance will be explored before exploring imaging of minimally opened cracks and small carbides.

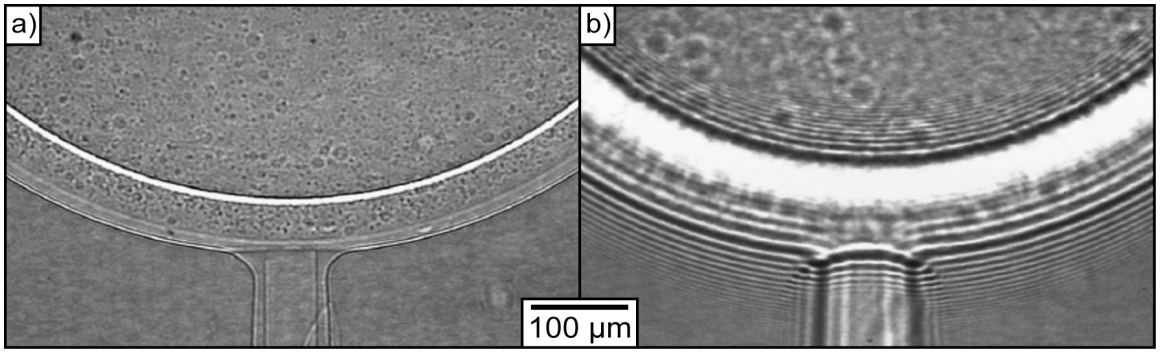


Fig. 3.3. Images of the bottom of a pair of concentric polystyrene and parylene spheres on a plastic holder with different sample-to-detector distances of (a) 0.15 m and (b) 3.08 m. Adapted from [15].

### 3.2.1 Two-Dimensional Slab

Monochromatic plane waves in vacuum are incident upon a slab of thickness, *T,* and length, *a*, and uniform $\alpha$ and $\delta$. The detector is located a distance *D* away from the sample along the z-direction. A ray trace shows qualitatively the effects of the edges on the waves (Fig. 3.4). Eqs. 3.13 and 3.14 become

$$\psi(x, D) = \psi_0 e^{ikD} \int_{-\infty}^{\infty} T(\xi)\, e^{-\frac{ik}{2D}(x-\xi)^2} d\xi \qquad [3.17]$$

$$T(\xi) = \begin{cases} 1 & \xi \le -a/2 \\ e^{-2k\beta T} e^{-ik\delta T} & -a/2 < \xi < a/2 \\ 1 & \xi \ge a/2 \end{cases} \quad [3.18]$$

with the y-direction neglected for simplicity. Plugging Eq. 3.18 into Eq. 3.17, simplifying, and including some of the integration constants in $\psi_0$:

$$\psi(x, D) = \psi_0 e^{ikD} \sqrt{\frac{\pi D}{k}} \{ [ (1 - 2C(\zeta)) + i(1 - 2S(\zeta)) ] + 2[C(\zeta) + iS(\zeta)] * e^{-T/\alpha} e^{-ik\delta T} \} \quad [3.19]$$

$$\text{where } \zeta = \sqrt{\frac{k}{\pi D}} (x - a/2)$$

The first bracketed term in the braces is the contribution from the vacuum, and the second term contains the attenuation and phase shift from the object. *C* and *S* are Fresnel integrals whose oscillations' spacings depend on *ζ*. When the sample-to-detector distance is very small ($D \approx 0$, $\zeta \to \infty$), *C* and *S* become similar to the Sign function and lose their oscillations. As *D* increases, their periods become larger, and the oscillations decrease in amplitude. X-ray energy has a similar effect: it is directly proportional to *k* and thus has the inverse effect on the intensity waveform as D. Though this option was not explored in this dissertation, the energy may be varied instead of the sample-to-detector distance when the range of possible distances is inadequate due to experimental constraints or if large ionizing radiation doses are a concern, as with medical imaging.


Fig. 3.4. Rays refracted at edges of a block with non-zero $\beta$ and $\delta$. The rays are attenuated for absorption contrast, but constructive and destructive interference at the detector highlight the edges of the block.

As with any diffraction phenomenon, the effects vary between the near field (Fresnel) and far field (Fraunhofer) [5,12]. Two useful parameters for distinguishing between the two diffraction regimes are the $n^{th}$ Fresnel-zone radius,

$$F_n = \sqrt{\frac{n\lambda\Delta D}{\Delta + D}} \qquad [3.20]$$

and the Fresnel number,

$$\mathcal{F} = \frac{a^2}{\lambda} \cdot \frac{\Delta + D}{\Delta D} \qquad [3.21]$$

where $n$ is the order of the zone, $\Delta$ is the source-to-sample distance, and $a$ is the transverse width of the diffracting object. The first Fresnel zone at $n$ = 1, or simply $F$, defines a locus of points where the additional path length from refraction exceeds the shortest path length by no more than $\lambda/2$. The Fresnel number determines where Fresnel diffraction is valid, or when $\mathcal{F}$ is approximately equal to or greater than one. Combining Eqs. 3.20 and 3.21 with the limit on $F$ for the near-field limit:

$$a \geq F \qquad [3.22]$$

If the object is smaller than the first Fresnel zone, Fraunhofer diffraction will hold. The image will be dominated entirely by phase information and bear little resemblance to

the sample. The interference oscillations will be very wide compared to the size of the object, and their amplitudes will overshadow any absorption information. For $a \approx F$, only a couple of interference features will be visible; for $a > F$, many narrow oscillations will exist [16]. The variation in interference effects with sample-to-detector distance can be quantified with a numerical example using the previously-described slab.

Consider the case of a 10-μm thick, 20-μm long block of nickel imaged at 23 keV with varying sample-to-detector distances (Fig 3.5). The edges on either end of the block are of interest, setting $a$ in Eq. 3.22 to 20 μm. When the detector is practically in contact with the sample ($F \approx 0$), the image is analogous to a pure absorption image without any phase-contrast effects. When $D$ = 0.075 m ($F \approx 2$ μm < $a$), the primary maxima and minima at the dotted lines are clearly visible and closely confined to within 2 μm of either edge. This edge-enhancement region is where the first-order extrema are most important. Higher-order oscillations decay very quickly and are tightly spaced, and they are not of sufficient magnitude to obscure the absorption image. Moreover, they disappear when considering finite-source-size effects and detector pixel sizes, as discussed in the next section. The contrast (Eq. 3.12), using the intensities of the primary maximum and minimum, increases from 18.5% in the absorption image to 72.6% in the edge-enhanced image – a nearly four-fold increase. Most of the imaging of cracks in this dissertation was performed in this edge-enhancement regime where $F < a$.

As $D$ increases so that the first Fresnel zone is of the same order as the feature size ($D$ = 7.5 m, $F \approx 20$ μm ≈ $a$), broadly spaced higher-order oscillations obscure the absorption image, but not completely. This is the holographic region, where image processing is required to completely reconstruct the original image. The highest possible contrast between interference maxima and minima occurs at $a = F$, in this case about 95%. At much large distances ($D$ = 120 m, $F \approx 80$ μm > $a$), the near-field conditions are no longer satisfied and $\mathcal{F} < 1$: this is the far-field dominated by Fraunhofer diffraction. Phase effects completely overpower absorption contrast, rendering a diffraction pattern devoid of structural details. For this reason and the prohibitively large sample-to-detector distance, very little PCI is performed in this regime.

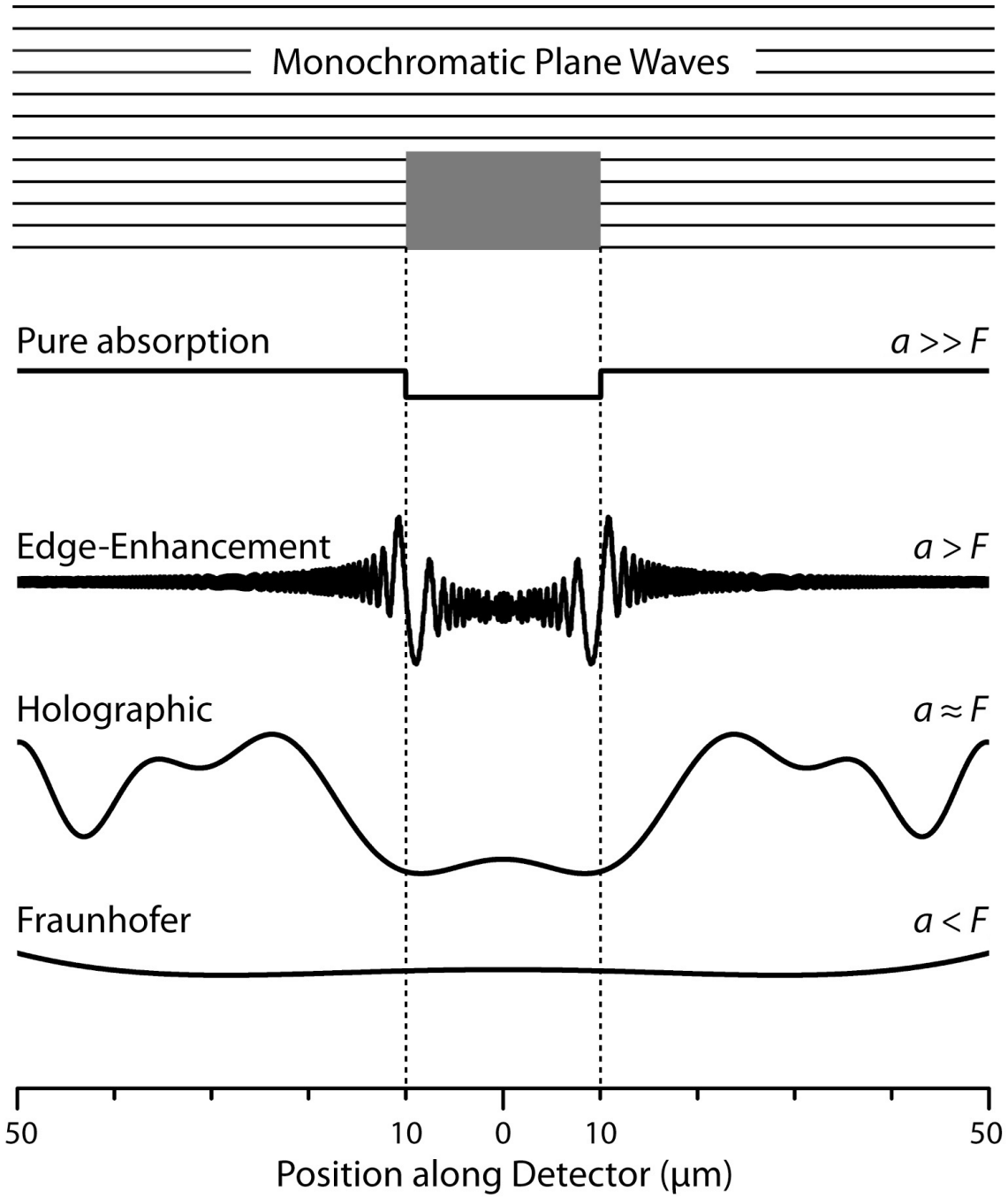


Fig. 3.5. Phase-contrast effects for a two-dimensional slab as the detector-to-sample distance, *D*, increases. *F* is the first Fresnel zone (Eq. 3.20), and *a* is the width of the slab (20 μm). The four main PCI regions are labeled, and the intensities are plotted. The absorption image is taken with the detector immediately after the sample. Edge enhancement occurs when *a* is greater than *F*. The holographic region is when *a* is approximately equal to *F*. Fraunhofer diffraction occurs for values of *a* smaller than *F*; the interference fringes are too broad to see with this x-scale.

### 3.2.2 Assumptions and their Validity

In the previous example, the limitations of coherence and the detector were not considered, and monochromatic plane waves under weak defocusing conditions were assumed. For PCI of weakly absorbing samples in the holographic region, these assumptions may impair accurate image reconstructions, necessitating a full understanding of the exact spatial and temporal coherence and energy spread of the x-ray beam, as well as the detector response. For crack imaging, which lies wholly in the edge-enhancement region (as discussed in the next section), these assumptions are adequate to model the intensity profiles accurately.

PCI in electron and optical microscopy is often performed under defocused conditions, because the contrast is at a minimum at perfect focus [12]. As the sample is defocused, the contrast increases, although the original image can be lost due to blurring. When weakly defocused, the image remains but with some contrast enhancement. The defocusing distance, DF, is defined as [5]

$$DF = \frac{\Delta D}{\Delta + D} \qquad [3.23]$$

where $\Delta$ and $D$ are, as before, the source-to-sample and sample-to-detector distances, respectively. At Sector 7-ID-C, $\Delta$ = 65 m and $D$ = 0.75 m, and at Sector 32-ID-C, $\Delta$ = 77 m and $D$ = 0.80 m; since $\Delta$ was nearly 100x larger than $D$, $DF \approx D$. The small value of $DF$ and small refraction of x rays mean that the weakly defocused condition is satisfied. Defocusing is a bigger concern for non-synchrotron PCI, where $\Delta \approx D$.

The assumption of monochromaticity is useful, but it is not an absolute requirement. The discrete wavelength, $\lambda$, can be replaced by a spectrally weighted sum of wavelengths when considering the finite energy spread, or even when using a white or pink beam [11,17-18]. In Eq. 3.19, this effect would spread the extrema in the Fresnel integral but not enough to cause neighboring local maxima to overlap for a narrow energy spectrum on par with that used in this work, $\Delta E/E \leq 10^{-4}$. Most of the imaging done in this work falls in the edge-enhancement regime and does not require image reconstruction, so the exact interference amplitudes are not necessary and any slight blurring from the narrow energy spectrum is inconsequential.

The incoming waveforms were assumed to be plane waves with perfect spatial, or lateral, coherence. However, because the source has a finite size, waves from different parts of the source will travel slightly different paths and may interfere at the object. At third-generation synchrotron sources, the source size is elongated in x-direction and contracted in y-direction due to the radiation profile from the undulator. The incoming wave fronts can be modeled as a two-dimensional (2D) Gaussian, with one-sigma widths determined by the source size, $\sigma_x \approx 120$ μm and $\sigma_y \approx 15$ μm at Sector 32 [19]. The effect on imaging from the source's penumbral angle is expressed as the projected source size:

$$\sigma_p = \frac{\sigma D}{\Delta} \qquad [3.24]$$

Given the source sizes above, $\sigma_{px}$ = 1.2 μm and $\sigma_{py}$ = 0.15 μm, and together these define a 2D Gaussian point-spread function (PSF) that is convolved with the intensity predicted from Eqs. 3.13-3.16, defined as $I_0$, to calculate the source-size-limited intensity, $I_{ss}$.

$$I_{ss}(x,y) = I_0(x,y) * PSF_{source}(x,y) \qquad [3.25]$$

The PSF will blur $I_0$ and limit the spatial resolution to approximately 1 μm in the x-direction, regardless of the spatial resolution of the detector. Since the detector in these experiments had a spatial resolution of approximately 1.5 μm, though, the finite source-size effects is not as limiting as other effects.

The lateral spacing over which complete dephasing between two waves occurs is called the transverse coherence length, $L_T$, and is given by [12,18]

$$L_T = \frac{\lambda \Delta}{2\sigma_T} \qquad [3.26]$$

$\sigma_T$ is a transverse source size, and using the projected source size values calculated above for 23 keV radiation and $\Delta$ = 77 m at Sector 32, the two transverse components are $L_{Tx}$ = 17 μm and $L_{Ty}$ = 138 μm. $L_T$ sets an upper limit on the size of features that will produce diffraction. For features larger than the coherence length, the waves at either end of the object will be uncorrelated and interfere in complicated ways at the detector. A 500-μm weakly absorbing object cannot be imaged in the holographic region, since this size is much larger than either $L_{Tx}$ or $L_{Ty}$. In the edge-enhancement regime, however,

the coherence lengths are adequate for sharp electron-density borders of cracks. Small features, such as carbides and pores of <10 μm, will diffract coherently and fall in the holographic regime.

Finally, the charge-coupled-device detector's quantum efficiency, pixel size, and bit depth imposes a limit on image quality [20-21], as does the YAG:Ce crystal scintillator. The response of the entire detector apparatus can be summarized by another PSF, and though it was not available, its effect would involve another convolution of the $I_{ss}$ given in Eq. 3.25:

$$I_d(x,y) = [I_0(x,y) * PSF_{source}(x,y)] * PSF_{detector}(x,y) \quad [3.27]$$

The new intensity at the detector after the two convolutions, $I_d$, will be blurred compared to $I_0$, possibly concealing small features in traditional absorption-based radiography without phase-contrast edge enhancement. Plots of $I_d$ in the edge-enhancement regime using the example in Section 3.2.1 would be smoother and lack many of the higher-order, low-amplitude oscillations just beyond feature edges.

### 3.2.3 Slab with a Carbide and Crack

PCI of a barely opened fatigue crack can be simulated using a modified version of the slab from Section 3.2.1. The model is again 2D for simplicity without loss of meaning. The sample is René N5 superalloy and 2,000-μm wide ($2L$) and 200-μm thick ($T$). It has a planar crack running at 45° whose length projected onto the detector axis is 200 μm ($2a$). The crack is only opened by 0.5 μm when measured normal to the fracture surface ($T_C$), and its through-thickness size as seen by the incident radiation is $T_C / \cos(45°) \approx 0.71$ μm. Away from the crack, centered at 500 μm ($x_c$) at a depth of 100 μm, is a 5-μm ($2l_c$) cubic titanium carbide. The model is shown representatively in Fig. 3.6, although for visibility, the crack is 100 times wider, and the carbide is 10 times larger.

The incoming photon energy is 23 keV, and the detector is located 0.80 m behind the object. Calculated intensity profiles were convolved with two Gaussian PSFs of full-width at half maximum (FWHM) of 1 μm and 2 μm to approximate the effects of the

horizontal projected source size and detector spatial resolution (Eq. 3.25). This is analogous to a cross-section perpendicular to the loading axis at the gauge section of a microfoil fatigue specimen, with accurate photon energy, sample-to-detector distance, and finite source size effects.

The absorption and phase effects below are required to calculate the transfer function:

$$\int_{-T}^{0}\beta(x,z)dz = 2k\beta\begin{cases} 0 & \xi \le -L \\ T & -L < \xi \le -a - T_c\cos(45°) \\ T-(\xi + a + T_C\cos(45°)) & -a - T_c\cos(45°) < \xi \le -a \\ T - T_C\cos(45°) & -a < \xi \le a \\ T-(a + T_C\cos(45°) - \xi) & a + T_c\cos(45°) < \xi \le a \\ T & a < \xi \le x_c - l_c \\ T + 2l(\beta_c/\beta - 1) & x_c - l_c < \xi \le x_c + l_c \\ T & x_c + l_c < \xi \le L \\ 0 & L \le \xi \end{cases} \quad [3.28]$$

$$\int_{-T}^{0}\delta(x,z)dz = \delta k\begin{cases} 0 & \xi \le -L \\ T & -L < \xi \le -a - T_c\cos(45°) \\ T-(\xi + a + T_C\cos(45°)) & -a - T_c\cos(45°) < \xi \le -a \\ T - T_C\cos(45°) & -a < \xi \le a \\ T-(a + T_C\cos(45°) - \xi) & a + T_c\cos(45°) < \xi \le a \\ T & a < \xi \le x_c - l_c \\ T + 2l(\delta_c/\delta - 1) & x_c - l_c < \xi \le x_c + l_c \\ T & x_c + l_c < \xi \le L \\ 0 & L \le \xi \end{cases} \quad [3.29]$$

The integrals in Eqs. 3.28 and 3.29 project the crack and carbide onto a single line along the z-axis before calculating $\psi(x,D)$. The crack's projected length along the z-direction of 200 µm, NOT the 0.5-µm opening, determines whether it falls within the edge-enhancement or holographic region of phase contrast. The opening does, however, determine the amount of phase-shift and absorption at either endpoint.

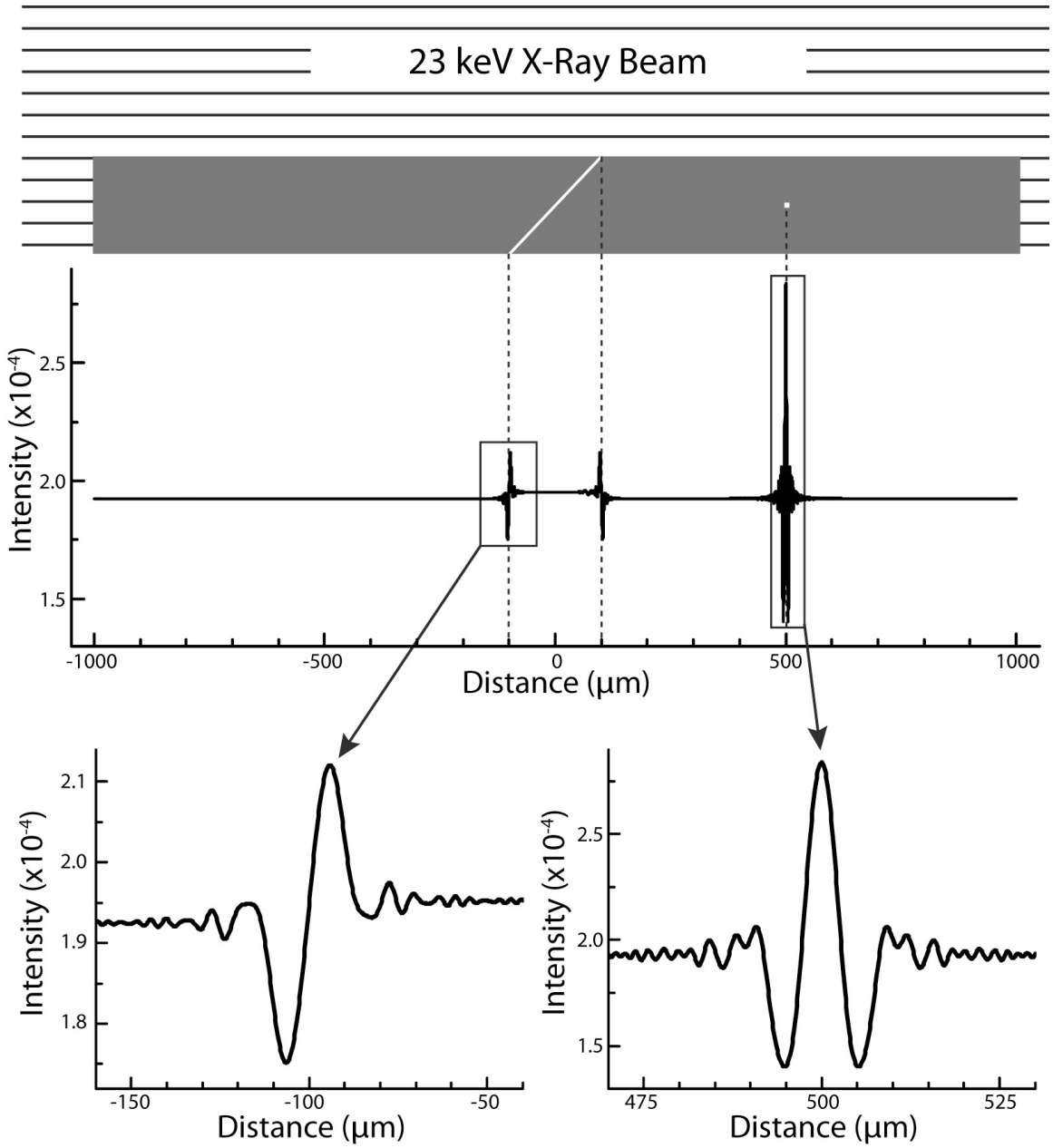


Fig. 3.6. Phase-contrast effects for a cracked, 2D slab containing a carbide. The crack opening and carbide are pictured disproportionately large for clarity. *D* is fixed at 0.8 m so that the crack is in the edge-enhanced regime and the carbide is in the holographic regime. Plots show the intensity profile as a function of distance across the block, with enlargements at one edge (lower left) and at the carbide (lower right). The effects of the slab edges are suppressed for clarity.

The edges of the sample at ±*L* are, of course, enhanced by phase contrast, but the absorption contrast alone is already very high at the border between the direct beam and any absorbing material. Furthermore, if the integration time is long enough for sufficient photons to reach the detector through the sample, the unattenuated

direct beam would saturate the detector and cause significant light bloom, obscuring the precise position of the sample edge regardless of the edge enhancement.

At 23 keV and with the sample-to-detector distance defined here, the first Fresnel zone is located at $F = \sqrt{\lambda D} = 6.36$ μm. The carbide falls within the holographic regime (Fig. 3.6, lower-right graph), since its size is approximately equal to the first Fresnel zone. While the contrast is reasonably significant with absorption alone at 3.9%, it rises to 57% with phase effects – an increase of fourteen fold. The full-width at half maximum (FWHM), 5.6 ± 0.6 μm, corresponds very accurately to the actual width of the carbide of 5.0 μm.

The crack will be in the edge-enhanced regime (Fig. 3.6, lower-left graph), since its size projected onto the imaging plane is 200 μm. Just before and just after the intersections with the surface at $\pm a$, the contrast due to absorption is only 0.70%, while with edge enhancement it increases more than twelvefold to 9.2% between the interference extrema. Table 3.2 contains contrast data for different crack openings. The spacing between the minimum and maximum peaks did not decrease significantly as the crack size decreased, so the pixel size was not a limiting factor for detection via phase contrast (aside from the contribution to the $PSF_{detector}$).

Table 3.2. Contrasts (Eq. 3.12) for various crack openings in the example of Section 3.2.3. The normal opening is the crack displacement measured normal to the fracture surface. The through-thickness opening is measured along the z-direction and equal to the normal opening divided by cos(45°).

| Normal Opening (μm) | Through-Thickness Opening (μm) | Edge-Enhanced Contrast (%) | Pure Absorption Contrast (%) |
|---|---|---|---|
| 1 | 1.4 | 18 | 1.4 |
| 0.5 | 0.71 | 9.2 | 0.70 |
| 0.1 | 0.14 | 1.9 | 0.14 |
| 0.05 | 0.071 | 0.92 | 0.070 |
| 0.01 | 0.014 | 0.18 | 0.014 |

The contrasts calculated in Table 3.2 were assuming a detector with an infinite number of bits for an infinitely fine intensity resolution. Our humble 12-bit detector lacked perfection and had a finite intensity resolution of $2^{-12}$, or 1 part in 4096. The

exposure time had to be sufficient to resolve features but avoid saturating the detector. The intensity at a single pixel on the detector can be defined as photons/second; an increase in exposure time simply scales the intensity. The constant multiplier cancels from all terms in the contrast (Eq. 3.12), and so a 12-bit noise-free detector could, in theory, resolve any feature with a contrast down to 0.02442%, or about a 2-nm through-thickness opening. Until that detector becomes available, the signal-to-noise ratio (SNR) limits the minimum resolvable crack opening without imaging processing techniques that would impair real-time diagnostics. Unfortunately, the SNR is highly dependent on several detector parameters that have not been fully characterized in our setup [19], including the linearity of the response, dead band, hysteresis, electronic noise, etc. [21]. An approximation for the SNR was, therefore, made based on experimental observations.

Consider a sample of 200-µm-thick René N5 imaged under typical conditions (23 keV, 0.2-s exposure time) at the center of the x-ray beam. The intensity of a small rectangle in the center of a dendrite had a mean intensity, $\mu$, of 2753 counts and standard deviation, $\sigma$, of 31 counts, for a SNR of $\mu/\sigma$ = 1.1%. The 1.0-µm crack, with a through-thickness opening of 1.4 µm, from the simulation would likely be the smallest crack resolvable with absorption alone, since its contrast of 1.4% is greater than the SNR of 1.1%, though its enhanced edges due to phase contrast would still be quite apparent with a contrast of 18%. Under these conditions, a crack of ~0.060 µm measured in the z-direction would have a phase-contrast enhanced contrast of 1.1%, setting a rough limit on the minimum opening for similar detector setups. This minuscule opening required is unattainable with conventional imaging techniques in this material, and provides incredible sensitivity to minimally opened cracks, particularly at the tips.

## 3.3 Diffraction Contrast

The final source of contrast comes from diffraction. Unlike the other two contrast mechanisms, diffraction does not have effects that are immediately apparent from Eq. 3.6, and it is sensitive to different aspects of the microstructure, such as strains and lattice constants. Diffraction contrast expands the spatial scale of sensitivity with x-ray radiography to the Ångstrom scale below the micrometer-scale of absorption and phase contrast.

When a plane wave is incident on a crystal, it is diffracted from the different crystalline planes according to Bragg's law [4,22-23]

$$2d\ sin(\theta) = n\lambda \qquad [3.30]$$

where *d* is the spacing between atomic layers, $\theta$ is the angle of incidence of the incoming x-ray beam, and $\lambda$ is the wavelength of the incident radiation. The variable *n* is an integer constant. When $\theta = \theta_B$ (the Bragg angle), waves from different planes will diffract in phase and add constructively at the detector (Fig. 3.7), decreasing the intensity of the transmitted beam.

The dependence on crystallographic-plane orientations in three dimensions (3D) is demonstrated by the Laue equations, a vector form of Eq. 3.30:

$$(\boldsymbol{k_0} - \boldsymbol{k_i}) \cdot (\boldsymbol{a} + \boldsymbol{b} + \boldsymbol{c}) = 2\pi(h + k + l) \qquad [3.31]$$

$\boldsymbol{k_0}$ and $\boldsymbol{k_i}$ are the outgoing and incoming wave vectors, respectively, whose difference, $\boldsymbol{\Delta k}$, is called the scattering vector; $\boldsymbol{a}$, $\boldsymbol{b}$, and $\boldsymbol{c}$ are the basis vectors of the crystal; and *h*, *k*, and *l* are integers called Miller indices [4]. All superalloys studied in this work are face-centered cubic (FCC) single crystals, and so *h*, *k*, and *l* must be all odd or all even [22]. From Eqs. 3.30 and 3.31, the Bragg angle has a discrete value for fixed λ and lattice spacing; however, for reasons discussed later in Section 3.3.2, the Bragg angle defines a broad peak with a non-zero FWHM, denoted as *B*.

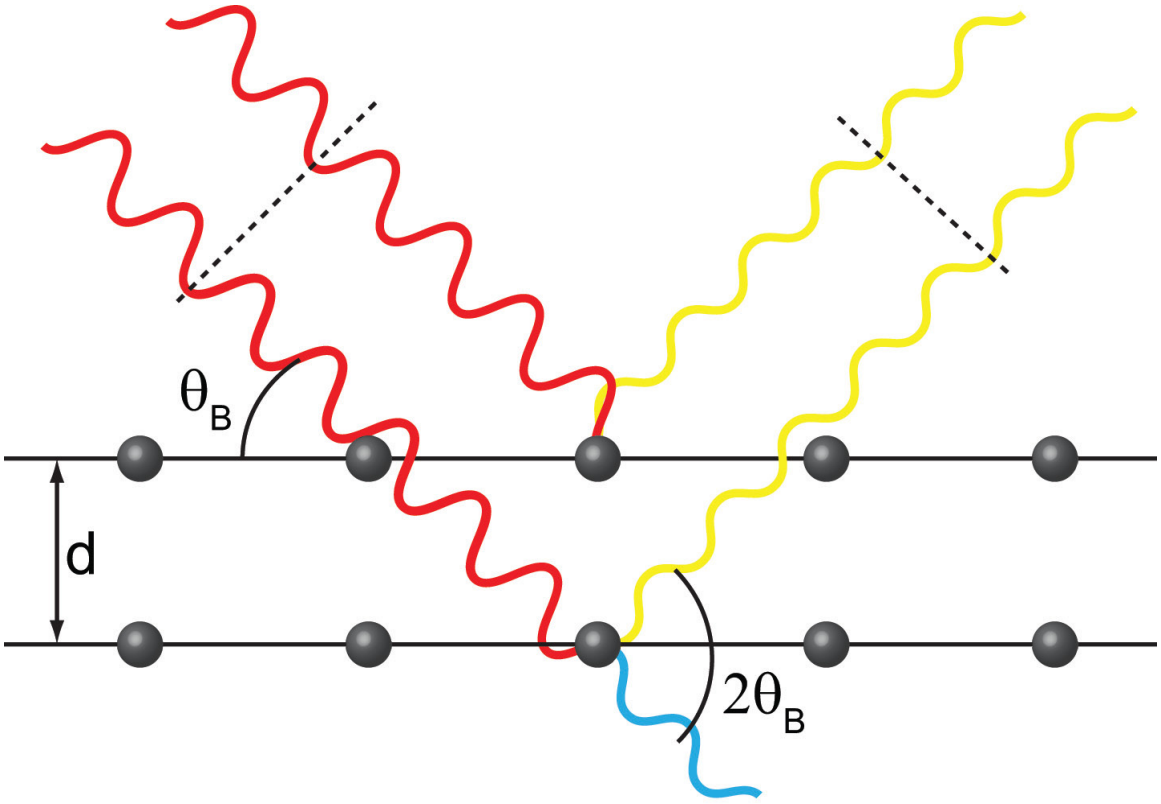


Fig. 3.7. Bragg diffraction according to Eq. 3.30, showing incoming (red), transmitted (blue), and diffracted (yellow) rays. The diffracted waves from different crystal planes are in phase at the Bragg angle, as shown by the dotted lines, leading to constructive interference at the detector. The incident wave enters at $\theta_B$ to the surface and diffracts at $2\theta_B$ with respect to the transmitted beam.

A sample plot of the intensity vs. $\theta$ around a Bragg angle, called a rocking curve (Fig. 3.8), shows that the peak in diffraction intensity is directly related to the nadir in the transmitted intensity. Rocking curves were measured near a Bragg angle for the transmitted beam only, although with only one axis of rotation and not three. The diffracted beam could not be measured directly, because the Ti-6Al-4V carrier absorbed any beam diffracted by more than a few degrees with respect to the forward direction. Measuring a diffracted peak would require significant re-engineering of the ultrasonic fatigue apparatus and a detector mounted on a diffractometer with at least two degrees of rotational freedom. Measuring the diffraction effects from the transmitted beam, however, was much more convenient and practical when radiographic details are paramount. This is in contrast to most other synchrotron diffraction experiments (e.g.,

[24-28]), where the diffracted beam is precisely determined and measured in 3D, and the transmitted beam is blocked by a beam stop or completely absorbed within the sample. Using diffraction to enhance a radiograph is called bright-field imaging, a technique familiar in transmission electron microscopy [29] but less common in synchrotron imaging, although some studies do exist [30].

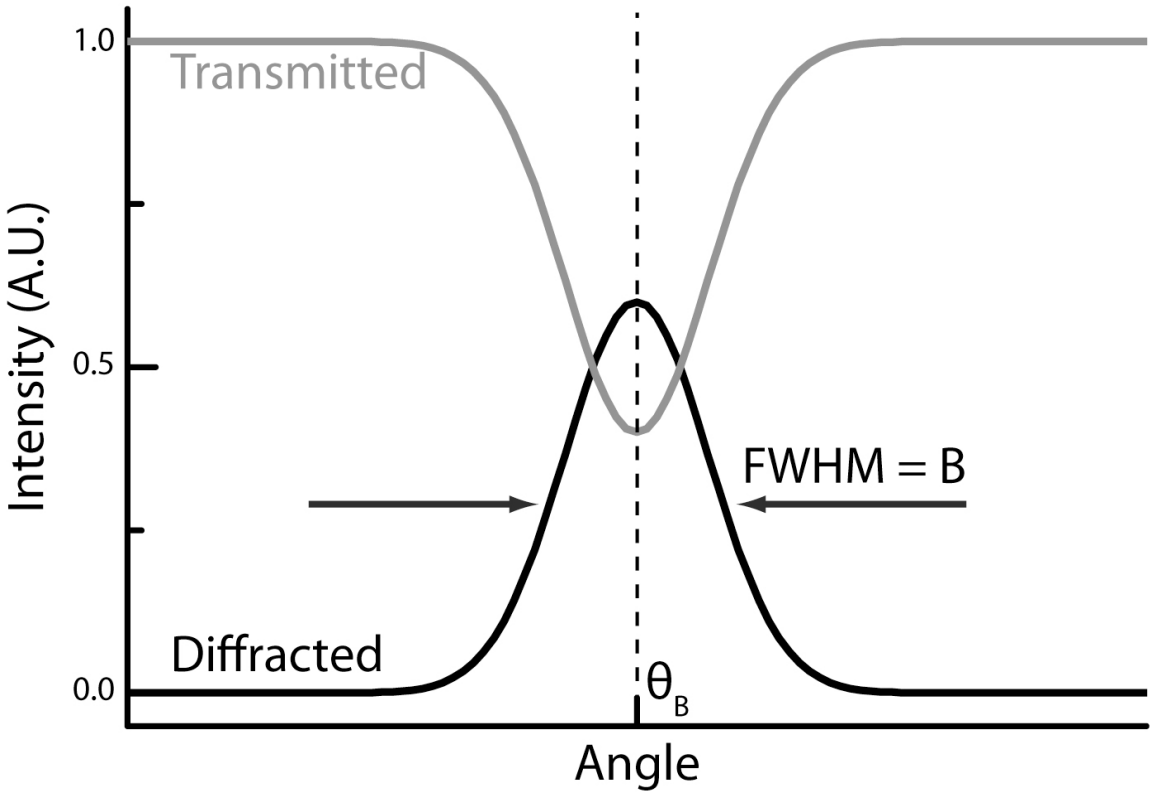


Fig. 3.8. Sample rocking curve around a Bragg angle, $\theta_B$. The intensities of the transmitted and diffracted beams have a nadir and peak, respectively, at $\theta_B$.

The following sections discuss features of the diffraction peak even though the transmission nadir was measured; this enables a simpler connection to existing literature on Bragg-angle analysis. Note the use of $\theta$, not $2\theta$, on the x-axis. Since the diffracted peak is located at an angle $2\theta_B$ from the transmitted beam direction (Fig. 3.7), it is customary to double the angle on the x-axis of rocking curves. Regardless of the nomenclature, diffraction imaging provides insight in two particular ways: Bragg-angle

shifts, which correspond to uniform strains and crystallographic misorientations, and Bragg-angle broadenings, which arise from non-uniform stresses and plasticity.

### 3.3.1 Bragg-Angle Position

Several factors determine the precise position of the Bragg angle that in turn provides useful material information. Consider a single-crystal superalloy that has two adjacent regions identical in composition but with slightly different crystallographic orientations, though still FCC with equivalent lattice parameter. The regions differ only by a slight rotation of their basis vectors (Fig. 3.9). If this crystal is rotated to a Bragg angle of the red region to satisfy Eq. 3.31, then the transmitted beam will be weakened in intensity from both attenuation (Eq. 3.7) and diffraction. The transmitted beam through the blue region, however, will be affected by attenuation alone, because its $\boldsymbol{\Delta k}$ does not satisfy Eq. 3.31 with its rotated basis vectors. The blue region appears brighter than the red region on the detector, with a slight blurring in the center where the two crystallites overlap in the through-thickness direction.

This variation in orientation within a nominally single-crystal material is called mosaicity and occurs naturally between the dendrites of superalloys. Misorientations of a couple degrees are possible, accommodated by a network of dislocations in the interdendritic regions [7,31]. Mapping the position of the Bragg angle can identify larger misorientations as well, such as those between grain boundaries in polycrystalline materials and twinned crystals. The lower limit on misorientation resolution is fixed by the intensity and width of the diffraction peak, which will be discussed later in Section 3.3.2.

A similar shift in $\theta_B$ occurs with strain, as it distorts the *d* spacing in Eq. 3.30 and the basis-vector magnitudes of Eq. 3.31. Uniform strain shifts the Bragg angle along one rotation axis, while non-uniform strain broadens the Bragg peak [4]. Superalloy samples in this work were cut along the [100], [010], and [001] directions; allowing for some slight miscuts, the {220} family of planes satisfies the Bragg condition when the beam is near normal incidence, and is, therefore, convenient for measuring rocking curves in

transmission geometry. Furthermore, a (220) reflection is about 27% as intense as the brightest reflection in an FCC crystal, the (111) reflection, as determined by the lengthy diffraction-intensity equation involving the structure factors, Lorentz polarization factor, and more (see [4] for calculation details).

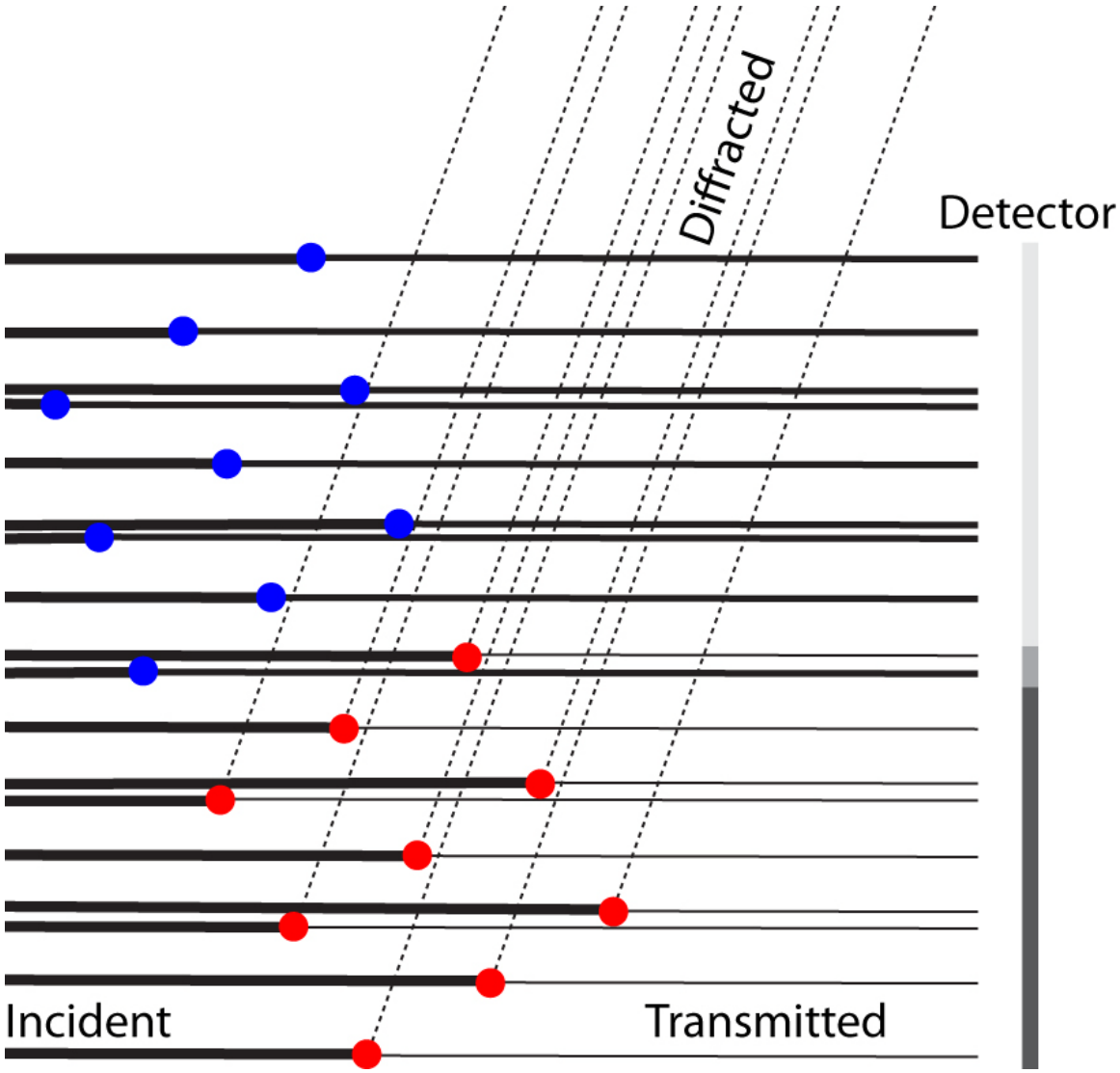


Fig. 3.9. Diffraction from two regions of the same composition but different crystallographic orientation. The red region is rotated to one of its Bragg angles and loses a part of its transmitted intensity to diffraction, thereby appearing darker on the detector than the blue region that does not satisfy a Bragg condition. The intensity at the center of the detector is affected by the overlapping regions in the through-thickness direction.

Consider the (220) reflection in a superalloy sample with a lattice parameter of 3.58 Å [32] imaged with 8.3 keV radiation. In the absence of any strain, applied or residual,

$$\theta_{220} = \arcsin\left(\frac{\lambda}{2d_{220}}\right) = 36.2° \quad [3.32]$$

where $d_{220}$ is the spacing between (220) planes given by

$$d_{220} = \frac{a}{\sqrt{h^2 + k^2 + l^2}} = 1.27 \text{ Å} \quad [3.33]$$

This Bragg angle is convenient for diffraction, because the {220} planes are oriented 45° to the surface when the sample is cut along the {100} crystallographic axes, as described in Chapter 2. Strain is defined here as $\varepsilon = \Delta d/d$, and its effects can be incorporated into Eq. 3.32 by multiplying the denominator of the arcsin term by $(1 + \varepsilon)$, which changes the calculated Bragg angle. For a difference of 1° between Bragg angles due to residual strain and not a crystallographic misorientation, the strain would be approximately 2.4% along the [220] direction (Eq. 3.32). Assuming the elastic properties of CMSX-4 and multiplying the strain by the Young's modulus, $E$, of 240 GPa along [110] [33], the stress, $\sigma$, equals 5.90 GPa. This stress value is several times larger than the ~1 GPa yield strength [8,34]. Any Bragg-angle deviations on this scale are likely not due to residual effects and instead are from crystallographic misorientations. This difference in diffraction angle could be verified alternatively by checking the reflection of a perpendicular plane for a corresponding compressive strain.

Typical mean stresses during fatigue testing were near 50 MPa along the [001] direction, so for a stress amplitude ratio, $R$, of 0.1, $\sigma_{min} \approx 9$ MPa and $\sigma_{max} \approx 90$ MPa. This loading regime produced a tensile stress in the (220) plane, and compared to the (220) reflection at the mean stress, the diffraction angle changed by approximately 0.014° during testing (Eq. 3.32). While small, this effect is still measureable, and exposures were best taken during the rests of the duty cycle. The intensity would be blurred otherwise, as the radiograph averaged over many cycles, during which some regions rocked about their diffraction angle.

Finally, any diffraction measurements were very sensitive to temperature fluctuations. Rocking curves required a few minutes to record, so any temperature changes on this time scale would introduce blurring or multiple peaks to the data. The furnace maintained a steady temperature with very slow drifts in the temperature on a time scale of tens of minutes, but the temperature produced by the microtorch would oscillate more rapidly by up to ±10°C with a period of less than one minute. With a linear thermal expansion coefficient of 8 to 18 x $10^{-6}$/°C [8] and operating at a temperature of 600 ± 10°C, the Bragg angle would shift by 0.0066° to 0.014° over the 20°C temperature amplitude, depending on the exact value of the linear thermal expansion coefficient. Though this shift was small, it was still significant enough to prevent any careful measurements of Bragg angles when using the microtorch.

### 3.3.2 Bragg-Angle Width

In the previous section, the peak broadening, *B*, was neglected, because only the position of the extremum was used. $B_{expt}$, the experimentally measured width, is determined by a number of factors, both from the instrumentation and from the sample [4,35]. These broadenings can be expressed separately as a sum:

$$B_{expt} = B_{inst} + B_{size} + B_{strain} \qquad [3.34]$$

$B_{instr}$ is due to the setup, $B_{size}$ is from finite-size effects of the coherently diffracting domain of the sample, and $B_{strain}$ is from microstrains within the sample itself. A particular peak profile as not assumed in Eq. 3.34, as the shape can be Gaussian, Lorentzian, or a complicated convolution of many peaks of each type. An alternative to measuring *B* involves the integral breadth, or the area under the peak, which can be analyzed using the Warren-Averbach method [36].

Measuring the strain quantitatively from Eq. 3.34 requires very accurate measurements of all parameters, and this is the subject of x-ray line profile analysis [25] and other diffraction techniques [37-39]. Such experiments typically require rotation about three axes and multiple accessible Bragg reflections. Given the experimental

limitations of this work, strains can still be mapped, albeit qualitatively, by subtracting the initial width before fatigue testing to a point during the test:

$$\Delta B_{strain} = \Delta B_{expt} - \Delta B_{instr} - \Delta B_{size} \quad [3.35]$$

$$\text{where } \Delta B_x = B_{x,1} - B_{x,0}$$

The subscript 0 refers to the initial state, such and the subscript 1 refers to a later state, such as after a crack has initiated or propagated. Any $B$ effects that do not change during testing can be neglected for a qualitative map of fatigue-inflicted damage.

$B_{instr}$ has numerous sources, including but not limited to non-ideal optics, slit size, wavelength, detector resolution, and source size [4]. This effect is measureable in an unstrained single crystal with no mosaicity for calibration; however, this step is unnecessary for this work, since by definition the effect is independent of the sample being imaged. Barring unanticipated problems with the beamline or synchrotron during testing,

$$B_{inst,0} = B_{inst,1} \Rightarrow \Delta B_{inst} = 0 \quad [3.36]$$

Provided $B_{instr}$ is not significantly larger than other sources of broadening, its effect can be neglected. One potentially detrimental source of instrumental broadening is a polychromatic beam, whose effect is evident in Eq. 3.30. For a white or pink x-ray beam, variation in the wavelength allows a range of angles and widens the diffraction peak. This factor is not significant with the monochromatic radiation at the APS, which has $\Delta E/E = \Delta\lambda/\lambda \approx 10^{-4}$ at both Sectors 7 and 32, and it corresponds to a broadening of less than 0.001°, which is negligible compared to other effects.

A perfect crystal, infinite in 3D, would produce an infinitely narrow peak in the absence of other sources of broadening, provided all planes diffracted coherently. The wavelength resolution, $\Delta\lambda/\lambda$, defines another parameter analogous to the traverse coherence length ($L_T$), called the longitudinal coherence length, $L_L$:

$$L_L = \frac{\lambda}{2\,\Delta\lambda/\lambda} \quad [3.37]$$

Together, $L_L$ and $L_T$ define a coherent volume element across which two waves from the same source point will completely dephase. At 8.3 keV, $L_L$ = 0.747 μm, and at 23 keV, $L_L$ = 0.270 μm; both are sufficiently long to include several atomic planes from which to

diffract coherently, but they still affect the peak-broadening term. For real crystals of finite size, $B_{size}$ is determined by either the size of the crystallite or the coherence length, whichever is smaller. In studies of single-crystal superalloys, where dendrites of equivalent crystallographic orientation are on the order of 100 µm or greater, $L_L$ is the limiting factor for diffraction coherence.

Using the Scherrer formula [40] with the coherence length as the size of the crystallite,

$$B_{size} = \frac{K\lambda}{L_L \cos(\theta)} \quad [3.38]$$

The Scherrer constant, *K*, ranges from 0.85 to 1.00 and is 0.89 for spherical crystals with cubic symmetry [4]. This equation is generally applicable to regions less than about 0.1 µm, yet it is used here for an order-of-magnitude estimate of the broadening. $B_{size}$ = 0.013° or 0.010° for the (220) reflection at 8.3 keV and 23 keV, respectively. As with instrumental broadening, this value will remain constant throughout fatigue testing in most regions, so $\Delta B_{size} = 0$. Because $\Delta B_{instr}$ is also negligible, Eq. 3.35 reduces to

$$\Delta B_{strain} = \Delta B_{expt} \quad [3.39]$$

Observed changes in the peak broadening are, therefore, practically independent of the instrumentation or diffracting-domain size effects and solely based on strain.

Distortions in the lattice define the peak broadening due to strain, including anisotropic strain, dislocations, temperature, and chemical inhomogeneity [4,25]. X-ray line-profile analysis deconvolutes these effects from the rocking curve, but as mentioned previously, the limitations of the setup preclude this. Fortunately, many of these effects do not change during crack propagation, and they can be neglected when considering the change during testing. For example, the γ phase is larger than the γ′ phase by 0.2% to 0.3% [41], resulting in a slight bimodal peak with a separation of about 0.02° to 0.06°, depending on the photon energy. The peaks are of unequal magnitude because of dissimilar volume fractions of the two phases, but this effect does not change during crack growth. Another confounding factor is the Debye-Waller temperature factor [12], which affects the structure factor and overall intensity, but it

also remains constant during testing, since the duty cycle minimizes heat buildup due to internal friction.

Anisotropic or non-uniform strains involve both tensile and compressive strains along multiple axes with different magnitudes. Consider two identical samples, one unstrained (Fig. 3.10, black) and the other with a non-uniform strain (Fig. 3.10, red). The *d* spacing on the top of the strained sample is larger than on the unstrained specimen, defining a tensile stress and a smaller $\theta_B$. The bottom arc of the strain sample has a compressive strain and a larger $\theta_B$. The arcs between the top and bottom arcs each define a shift in $\theta_B$, and the overall effect is a broader peak, still centered at $\theta_B$, but with a lower intensity. The broadening is related to the derivative of Bragg's law:

$$B_{strain} = 2\frac{\Delta d}{d}\tan(\theta) = 2\varepsilon \tan(\theta) \qquad [3.40]$$

For the (220) reflection at 8.3 keV and a reasonable strain of 0.1%, this corresponds to a width increase of 0.084°, which is significantly more than the effects of instrument broadening or coherence length.

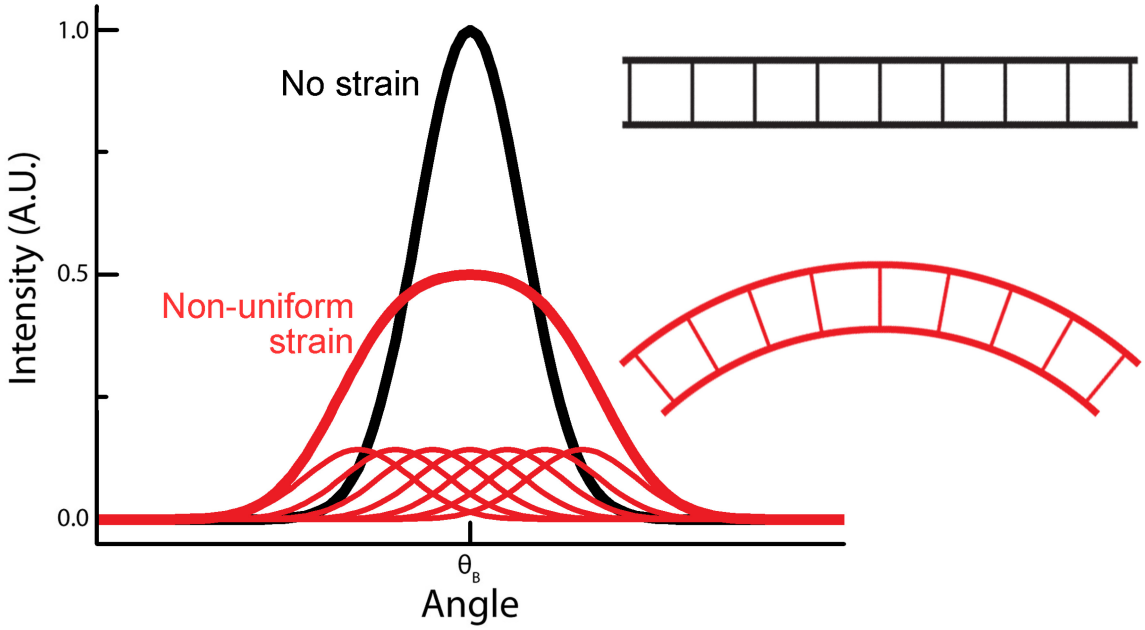


Fig. 3.10. Diffraction from a region with no strain (black) and a non-uniform strain (red). The curvature produces numerous peaks shifted slightly away from $\theta_B$, whose overall convolution is a shallower, broader peak.

Dislocations and plastic deformation cause a breakdown in the long-range order of the crystal, and as the lattice becomes imperfect, the diffraction peak broadens and decreases in intensity. This peak change happens as dislocations pile up around large defects or at grain boundaries [42]. The strain is still defined by Eq. 3.40, but dislocations can cause changes to the peak shape as well as broadening [25], further complicating the analysis. Furthermore, the amount of broadening is strongly dependent on the Miller indices of the reflection, and a proper, quantitative analysis requires rocking curves about multiple Bragg angles across three axes [35]. Nevertheless, comparing the change in the Bragg peak width at each pixel in the radiograph indicates qualitatively where this type of damage has occurred.

Before a fatigue crack grows, persistent slip bands (PSBs), or dislocation aggregates along crystallographic planes, develop and suggest possible propagation paths before any physical separation occurs [42]. In addition, as a crack grows, it is preceded by a plastic zone [42-43]. Neither effect is easily visible with the other two contrast mechanisms: the density change is very slight for absorption contrast, and no strong electron-density gradient is present for phase contrast. Thus, mapping $\Delta B_{expt}$ onto each pixel of the radiograph can explain the crack path when it changes to another crystallographic plane or when it slows down near a grain boundary. More significantly, though, this mapping can anticipate a crack before it is a physical separation between two regions. Two examples of peak-width mapping are shown for PSB growth (Fig 3.11a) and crack propagation (Fig. 3.11b). Predicting and detecting crack initiation visually, rather than with physical or statistical models, is very difficult with any other diagnostic technique beside PCI.

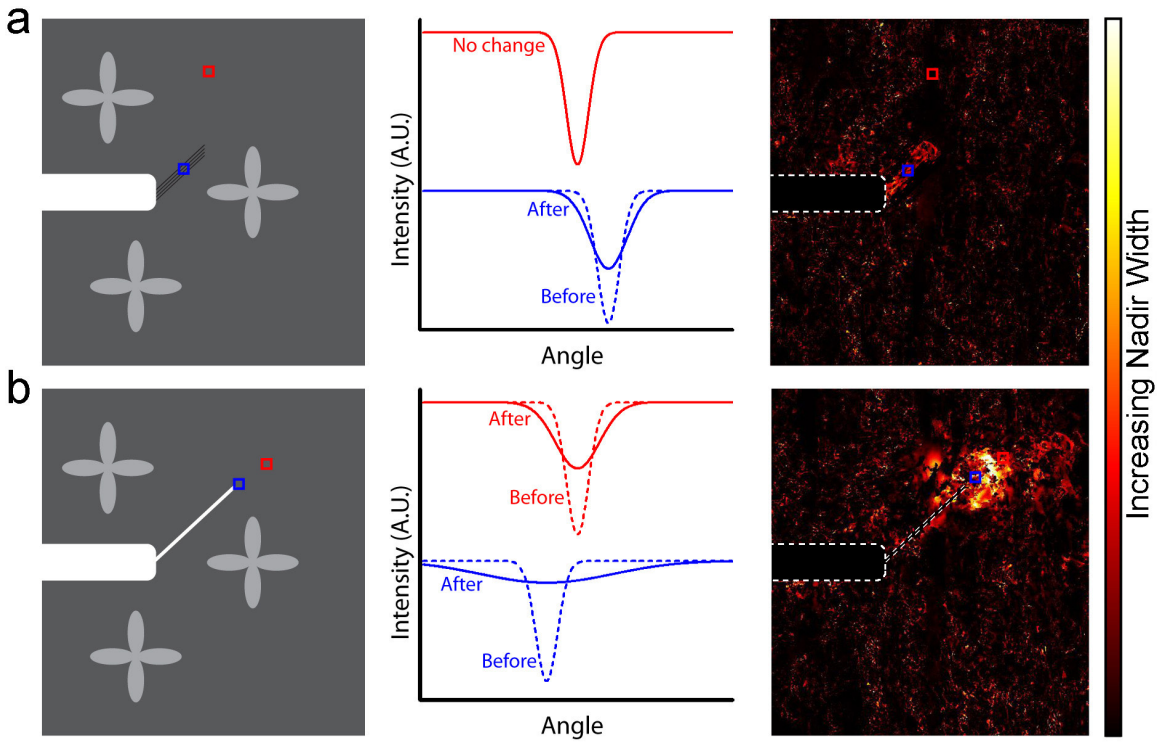


Fig. 3.11. Sample maps of nadir-width change for (a) PSBs and (b) fatigue crack emitting from a notch. The first column shows a schematic of the features, including two boxed areas of interest. The second column contains plots of the peak width in the boxed areas before any fatigue testing (dotted line) and after fatiguing (solid line). The third column is a map of the change in strain width with small amounts of random peak broadening appearing as dark-red regions; this is typically observed in real diffraction maps. The notches in (a) and (b) and the crack of (b) are outlined with a dotted white line.

## 3.4 Summary

As described in the previous sections, each contrast mechanism is uniquely suited to an important aspect of the microstructure and fatigue-crack propagation in superalloys, as summarized in Table 3.3 at the end of this section. Absorption contrast differentiates between regions of different composition and density, and the effect is quantified by $\beta$, the imaginary part of the refractive index. It reveals dendritic and interdendritic regions, carbides, and notches. It is also sensitive to geometries that change the through-thickness OPL, such as pores and cracks. Lastly, subtle compositional variation can be measured by tuning the energy about an absorption edge to dramatically alter the contrast of a particular constituent element. In general, absorption contrast is useful for feature sizes and crack openings greater than 1 μm.

Phase contrast enhances the absorption contrast with constructive and destructive interference fringes around variations in the real part of the refractive index, $\delta$. For the setups described in Chapter 2, the first Fresnel zones are 10.5 μm at Sector 7 and 6.5 μm at Sector 32. Any objects larger than these values, such as cracks and dendrites, had their absorption-contrast effects significantly enhanced at the edges. Objects on the order of the first Fresnel zone, such as carbides and pores, fell into the holographic region and were also enhanced with a single Gaussian-like waveform. Even small submicron roughness on the crack interface interfered enough to be resolvable despite the detector's 1.5-μm spatial resolution, since the spacing between interference extrema was wider than the size of the feature.

Finally, diffraction contrast provides atomic-scale information regarding lattice quality and mosaicity. A rocking curve at a single point in the detector plane provides a plot whose nadir position is determined by isotropic strain or mosaicity, and whose width is related to anisotropic strain and dislocations. The Bragg point could be totally eliminated with significant breakdown of the crystalline structure from plastic deformation. Diffraction contrast is most sensitive to aggregates with Ångstrom-to-nanometer-scale features. Together, these three contrast mechanisms span a wide range of spatial resolutions, providing details of many microstructural features critical to superalloy fatigue properties.

Table 3.3. Summary of contrast mechanisms and their sensitivity to features at particular spatial scales.

| Contrast mechanism | Sensitivity | Spatial scale (m) |
|---|---|---|
| **Absorption** | Sample geometry | $\geq 10^{-4}$ |
| | Dendritic/interdendritic regions | $10^{-4}$ |
| | Notches | $10^{-5}$ |
| | Carbides, pores, inclusions | $10^{-6}$ |
| | Cracks | $10^{-6}$ |
| | Compositional distributions | varies |
| **Phase** | All absorption features | $\geq 10^{-6}$ |
| | Surface cracks | $10^{-7}$ |
| | Interfacial crack roughness | $10^{-7}$ |
| **Diffraction** | Plastic zone | $10^{-4}$ to $10^{-5}$ |
| | Mosaicity, grains | $10^{-4}$ to $10^{-6}$ |
| | Dislocations | $10^{-9}$ to $10^{-10}$ |
| | Strain | n/a |

## 3.5 References


1 Jackson, J. D. *Classical electrodynamics*. (Wiley, 1999).

2 Michette, A. G. & Buckley, C. J. *X-ray science and technology*. (Institute of Physics Pub., 1993).

3 Thompson, A., Attwood, D., Gullikson, E., Howells, M., Kim, K.-J., Kirz, J., Kortright, J., Lindau, I., Liu, Y., Pianetta, P., Robinson, A., Scofield, J., Underwood, J., Williams, G., Winick, H. *X-ray data booklet*. 3rd edn, (Lawrence Berkeley Laboratory, University of California, 2009).

4 Cullity, B. D. & Stock, S. R. *Elements of x-ray diffraction*. (Prentice Hall, 2001).

5 Born, M. & Wolf, E. *Principles of optics: electromagnetic theory of propagation, interference and diffraction of light*. 7th edn, (Cambridge University Press, 1999).

6 Hubbell, J. H., Seltzer, S. M. *Tables of x-ray mass attenuation coefficients and mass energy-absorption coefficients from 1 keV to 20 MeV for elements Z = 1 to 92 and 48 additional substances of dosimetric interest.*, <http://www.nist.gov/pml/data/xraycoef/index.cfm> (1996).

7 Husseini, N. S. *et al.* Mapping single-crystal dendritic microstructure and defects in nickel-base superalloys with synchrotron radiation. *Acta Mater* **56**, (2008).

8 Pollock, T. M. & Tin, S. Nickel-based superalloys for advanced turbine engines: Chemistry, microstructure, and properties. *J Propul Power* **22**, (2006).

9 Haynes International, Inc, Kokomo, IN.

10 Liu, L. *et al.* In situ synchrotron x-ray imaging of high-cycle fatigue crack propagation in single-crystal nickel-base alloys. *Acta Mater* **59**, (2011).

11 Cloetens, P., Barrett, R., Baruchel, J., Guigay, J. P. & Schlenker, M. Phase objects in synchrotron radiation hard x-ray imaging. *J Phys D Appl Phys* **29**, (1996).

12 Cowley, J. M. *Diffraction physics*. (Elsevier Science B.V., 1995).
13 De Caro, L., Cedola, A., Giannini, C., Bukreeva, I. & Lagomarsino, S. In-line phase-contrast imaging for strong absorbing objects. *Phys Med Biol* **53**, (2008).
14 Gureyev, T. E. *et al.* Some simple rules for contrast, signal-to-noise and resolution in in-line x-ray phase-contrast imaging. *Opt Express* **16**, (2008).
15 Cloetens, P. *Contribution to Phase Contrast Imaging, Reconstruction and Tomography with Hard Synchrotron Radiation: Principles, Implementation, and Applications*. Ph.D. thesis, Vrije Universiteit Brussel, (1999).
16 Cloetens, P. *et al.* Observation of microstructure and damage in materials by phase sensitive radiography and tomography. *J Appl Phys* **81**, (1997).
17 Pogany, A., Gao, D. & Wilkins, S. W. Contrast and resolution in imaging with a microfocus x-ray source. *Rev Sci Instrum* **68**, (1997).
18 Wilkins, S. W., Gureyev, T. E., Gao, D., Pogany, A. & Stevenson, A. W. Phase-contrast imaging using polychromatic hard X-rays. *Nature* **384**, (1996).
19 Fezzaa, K. Personal communication, March 8, 2012
20 Knoll, G. F. *Radiation detection and measurement*. (Wiley, 1979).
21 Fraden, J. *Handbook of Modern Sensors - Physics, Designs and Applications*. 3rd edn, (Springer, 2001).
22 Kittel, C. *Introduction to solid state physics*. (Wiley, 2005).
23 Ashcroft, N. W. & Mermin, N. D. *Solid state physics*. (Holt, Rinehart and Winston, 1976).
24 Biermann, H. *et al.* Determination of local strains in a monocrystalline turbine blade by microbeam X-ray diffraction with synchrotron radiation. *Acta Mater* **48**, (2000).
25 Ungar, T. Micro structural parameters from X-ray diffraction peak broadening. *Scripta Mater* **51**, (2004).
26 Kumah, D. P. *et al.* Correlating structure, strain, and morphology of self-assembled InAs quantum dots on GaAs. *Appl Phys Lett* **98**, (2011).
27 Bruno, G., Schumacher, G., Pinto, H. C. & Schulze, C. Measurement of the lattice misfit of the nickel-base superalloy SC16 by high-energy synchrotron radiation. *Metall Mater Trans A* **34**, (2003).
28 Korsunsky, A. M. *et al.* Crack tip deformation fields and fatigue crack growth rates in Ti-6Al-4V. *Int J Fatigue* **31**, (2009).
29 Fultz, B. & Howe, J. M. *Transmission electron microscopy and diffractometry of materials*. (Springer, 2002).
30 Yi, J. M. *et al.* Bright-field imaging of lattice distortions using x rays. *Appl Phys Lett* **89**, (2006).
31 Pollock, T. M. & Argon, A. S. Creep Resistance of CMSX-3 Nickel-Base Superalloy Single-Crystals. *Acta Metall Mater* **41**, (1993).
32 Tin, S. & Pollock, T. M. Phase instabilities and carbon additions in single-crystal nickel-base superalloys. *Mater Sci Eng A* **348**, (2003).
33 Hermann, W., Sockel, H. G., Han, J. & Bertram, A. Elastic properties and determination of elastic constants of nickel-base superalloys by a free-free beam technique. *Superalloys 1996*, (1996).

34 Cavaliere, P. & Panella, F. Mechanical and microstructural behaviour of CMSX-4 Ni-based superalloy joined by capacitor discharge welding. *J Mater Process Tech* **183**, (2007).
35 Ungar, T. Dislocation densities, arrangements and character from X-ray diffraction experiments. *Mater Sci Eng A* **309**, (2001).
36 Warren, B. E. X-Ray Studies of Deformed Metals. *Prog Met Phys* **8**, (1959).
37 Benedetti, A., Fagherazzi, G., Enzo, S. & Battagliarin, M. A Profile-Fitting Procedure for Analysis of Broadened X-Ray-Diffraction Peaks .2. Application and Discussion of the Methodology. *J Appl Crystallogr* **21**, (1988).
38 Enzo, S., Fagherazzi, G., Benedetti, A. & Polizzi, S. A Profile-Fitting Procedure for Analysis of Broadened X-Ray-Diffraction Peaks .1. Methodology. *J Appl Crystallogr* **21**, (1988).
39 Warren, B. E. *X-Ray Diffraction*. (Dover Publications, 1990).
40 Scherrer, P. Bestimmung der Grösse und der inneren Struktur von Kolloidteilchen mittels Röntgenstrahlen. *Göttinger Nachrichten Math. Phys.* **2**, (1918).
41 Pollock, T. M. & Field, R. D. Dislocations and high-temperature plastic deformation of superalloy single crystals. *Dislocations in Solids* **11**, (2002).
42 Suresh, S. *Fatigue of Materials*. 1st edn, (Cambridge University Press, 1991).
43 Nicholas, T. *High Cycle Fatigue: A Mechanics of Materials Perspective*. (Elsevier, 2006).

# CHAPTER 4

# IMAGING MICROSTRUCTURE AND MOSAICITY

Fatigue is affected by many microstructural features spanning several spatial orders of magnitude, from hundred-micron-scale dendrites to micron-scale carbides and even down to atomic-scale dislocations [1]. These features were first studied with a trio of contrast modalities detailed in the previous chapter in a static, fatigue- and stress-free environment. This imaging work not only lays the groundwork for fatigue-crack results to be presented, but it also supplies new insights into the elemental distribution, mosaic character of the ostensibly single-crystal superalloy, and interdendritic dislocation densities [2]. Superalloy and setup information will be summarized briefly here but are presented more thoroughly in Sections 2.1 and 2.3.1.

## 4.1 Seeing Both the Trees and the Forest

Samples of René N5 superalloy were cut into square coupons both parallel and perpendicular to the [001] casting direction. They were 2 mm by 2 mm in the plane perpendicular to the x-ray beam and 100- to 150-μm thick. Samples were attached to a post with a clip and mounted on a translation and rotation stage at Sector 7-ID-C of the Advanced Photon Source (Fig. 2.6). They were irradiated with an unfocused 8.300 keV x-ray beam with dimensions of approximately 800 μm by 500 μm for 0.5 to 20 seconds, depending on the sample thickness. Transmitted x rays stimulated fluorescence in a YAG:Ce scintillator crystal, which produced green light that was imaged by a charge-coupled device detector. Images were viewed in real time from a computer located outside the experimental hutch and later corrected for a non-uniform beam profile. The beam position shifted slightly when the energy changed or the detector moved, and new beam profiles were unfortunately not always recorded for each new beam position.

As a result, some images were not background subtracted, and instead the images were cropped to include the flattest part of the beam and exclude the darker regions.

For microstructural imaging, absorption is the dominant contrast mechanism, with edge enhancement from phase contrast, as seen in two radiographs taken from 150-µm-thick specimens cut parallel (Fig. 4.1a) and perpendicular (Fig. 4.1b) to the dendrite-growth direction. The images contain slight horizontal striations and other minor artifacts from deformations in the beryllium windows and Kapton filters of the beamline optics, as well as some small imperfections in the YAG:Ce crystal. While reduced, these effects were not completely eliminated with post-processing background correction.

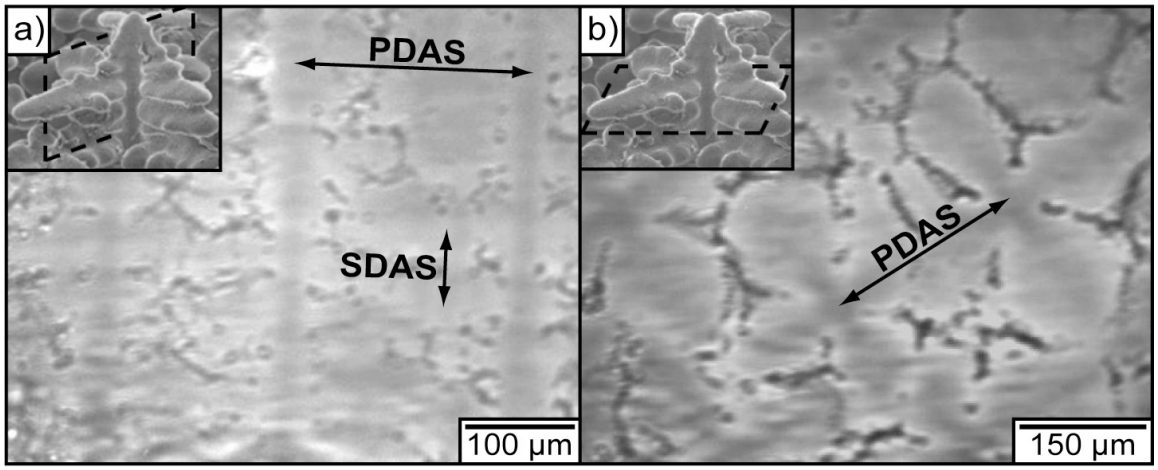


Fig. 4.1. Radiographs of 150-µm-thick René N5 taken parallel (a) and perpendicular (b) to the [001] casting direction. The scanning-electron micrographs in the top-left corners show the cross-section's relation to the three-dimensional dendrites. PDAS and SDAS are the primary and secondary dendrite arm spacings, respectively.

Dendrites appear lighter than the darker interdendritic regions, because they contain more nickel and have a longer attenuation length than the generally more electron-dense interdendritic regions. Primary dendrites are oriented vertically in Fig. 4.1a, with secondary dendrites growing horizontally. In Fig. 4.1b, the primary dendrites are oriented perpendicular to the page, with the four-fold-symmetric secondary dendrites visible in the plane. These arboresque structures are analogous to trees, with the primary dendrites as cores and secondary dendrites as branches; any

tertiary or quaternary structures would be analogous to twigs or leaves, though the superalloys studied in this work did not have these additional structures. Since the interdendritic composition is not as constant as the dendritic regions, they appear more as a series of closely spaced dots or lines than as a contiguous region of constant intensity. Only a few carbides are visible and appear as bright dots in the interdendritic regions; later figures contain more examples of these.

The primary dendrite arm spacing (PDAS), or the distance between neighboring dendritic cores in the (001) plane [3], is determined by the cooling rates during solidification. The PDAS, shown graphically in Fig. 4.1, is approximately 200 to 300 μm, depending on which dendrites are compared and where they are located in the through-thickness direction. This range matches the expected sizes based on the cooling rates [1,4]. When imaging parallel to the casting direction (e.g., Fig. 4.1a), multiple dendrites will not likely be superimposed in the through-thickness direction with thin samples of 100-150 μm thick.

The secondary dendrite arm spacing (SDAS), or the spacing between the dendrite branches along the [001] direction [3], is between 60 μm and 80 μm as measured from Fig. 4.1a. Thus, for radiographs taken perpendicular to the casting direction in 100-200 μm thick specimens (e.g., Fig. 4.1b), multiple dendrite arms may overlap, albeit in registry. They have identical composition and crystallographic orientation, and the interdendritic regions are small (~5-15 μm) compared to the secondary dendrites, so the SDAS will not affect the absorption intensity or mosaicity noticeably when the three-dimensional composition is projected onto the two-dimensional (2D) imaging plane. The radiograph will still show a single dendrite arm.

The x-ray energy was tuned to 8.300 keV, just below the nickel $K_\alpha$ absorption edge of 8.333 keV, to maximize dendritic/interdendritic contrast throughout the image. An image taken at 8.500 keV with a 20-second exposure length (Fig. 4.2a) appears washed out with very little interregional contrast, since the attenuation length throughout is very similar. Minor structural details are still visible, though. Without an upstream harmonic-rejection mirror, some third-harmonic energies at 25.500 keV

penetrated the sample and provided contrast. Carbides still appear bright because of phase contrast and not just absorption contrast. At 8.5 keV, the first Fresnel zone (Eq. 3.20) is 10.4 µm, and the carbides in Fig. 4.2 are all approximately this size or smaller. Because these features are approximately equal to or smaller than the first Fresnel zone, they fall in the holographic region, where the phase information has a significant effect on the final image beyond mere edge enhancement [5-6]. An intensity line profile through a carbide (Figs. 4.2a and 4.2c, cyan line), shows the distinctive constructive and destructive interference fringes of phase contrast. For the same region imaged at 8.3 keV (Fig. 4.2b), the nickel is significantly more transparent, and hence the required exposure time is only 1 second for an image with drastically improved interregional contrast. Again, the carbides are also visually enhanced by phase contrast (Figs. 4.2b and 4.2c, red line). All subsequent radiographs were taken at 8.3 keV.

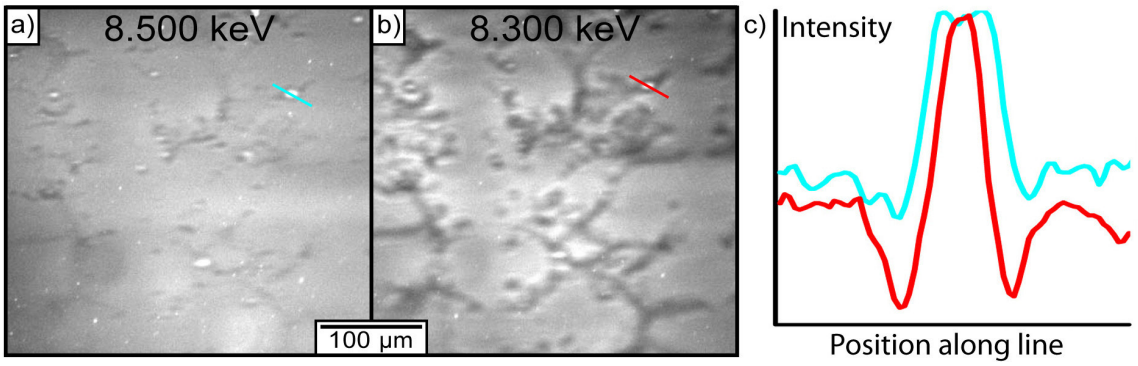


Fig. 4.2. Images taken at (a) 8.500 keV and (b) 8.300 keV, which are above and below the Ni $K_\alpha$ absorption edge, respectively, for a 100-µm-thick sample cut parallel to the casting direction. Carbides are visible in both images due to phase contrast, as shown by line profiles in (c) for a single carbide in both images.

Comparing the contrast quantitatively to any numerical predictions from Eq. 3.11 in Section 3.1 is not trivial, since the composition is more variable in the interdendritic regions than within the dendrites. Radiographs project the through-thickness details onto a single pixel, so the attenuation length may be determined by both interdendritic and dendritic regions if they overlap. Given the measured SDAS of 75 µm, this overlap is quite likely in images taken perpendicular to the casting direction.

Even when assuming a single through-thickness interdendritic region, the composition will not likely be uniform, especially over a 150-μm thickness. Qualitatively, though, the relative dearth of nickel clearly reduces the intensity and provides ample contrast to the nickel-rich dendrites, as predicted in Section 3.1.

Looking at the rightmost complete dendrite from Fig. 4.1b and adjusting the contrast to undersaturate the interdendritic regions and enhance the intradendritic contrast, phase contrast's edge-enhancing effects are manifest (Fig. 4.3). The dendrite is bordered by a fine white line from constructive interference that separates the regions. Because the interdendritic region is narrow and of weak intensity, the accompanying destructive interference fringes are absent. Some edges do not show any significant constructive interference, either (Fig. 4.3, cyan line). If the electron density, and hence the phase term of the refractive index, does not change rapidly from one region to another, then the interference effect will be diminished. Also, the x-ray beam is much more coherent in the vertical direction than in the horizontal direction; therefore, depending on the sample orientation, some line profiles may show greater phase contrast than others.

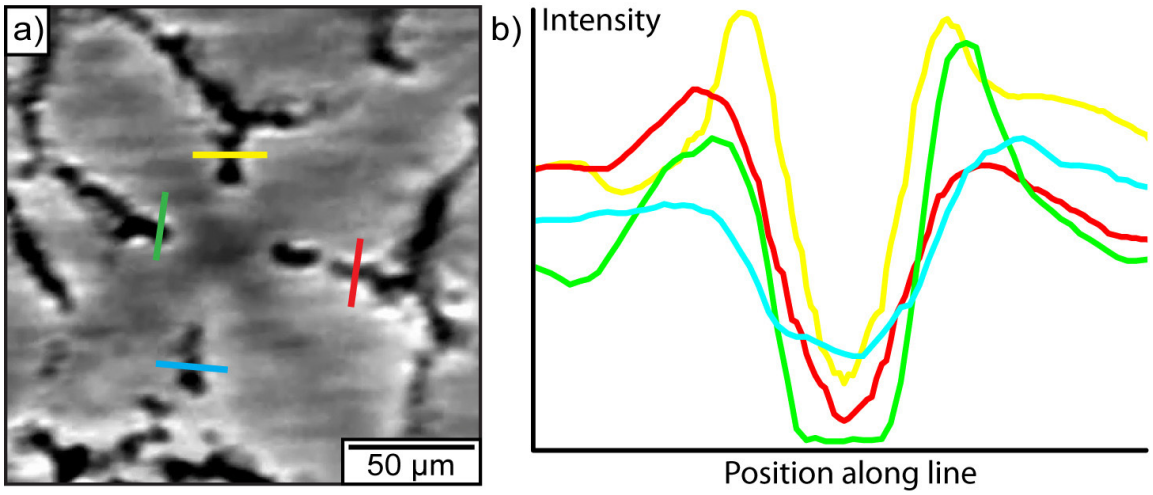


Fig. 4.3. Phase-contrast enhancement of the dendritic microstructure. (a) Rightmost complete dendrite of Fig. 4.1b with the contrast adjusted to undersaturate the interdendritic regions. (b) Plot of four intensity line profiles at the border between the dendritic and interdendritic regions.

## 4.2 Composition Mapping

The intensity across a single dendrite is not uniform (ignoring the horizontal striations), as is evident in Fig 4.1 and particularly in Fig. 4.3b due to the image's contrast settings. The dendritic core absorbs x rays more strongly than the surrounding arms, suggesting a compositional effect (Eq. 3.11). During directional solidification, heavy elements may diffuse more slowly than other elements outward from the core into the secondary dendrite arms, segregating unevenly throughout the dendrite [7]. More electron-dense material in the core would decrease the attenuation length with respect to that of the arms, and thus the intensity can be correlated to a composition change.

The elemental distribution of the dendrite shown in Fig. 4.3b was analyzed for all constituents of René N5 (Table 2.1) except C, Hf, and Y, which had negligible effects on x-ray attenuation lengths given their low concentration. Scans were performed with an electron-probe microanalyzer (EPMA) equipped with four wavelength-dispersive spectrometers (WDS) [8]. The beam current and acceleration voltage were 100 nA and 20 kV, respectively. The WDS system had eight diffraction crystals particular to the elements under investigation, and x-ray counts were measured simultaneously at various absorption edges (Table 4.1). The counts were converted to concentration values using standard correction procedures calibrated from pure-element standards, except for Al, which was compared to a 70Ni-30Al (wt.%) standard.

Table 4.1. EPMA testing details about the diffraction crystal used and absorption edge where x-ray counts were measured. TAP = thallium acid phthalate; LiF = lithium fluoride; PET = pentaerythritol.

| **Element** | **Al** | **Co** | **Cr** | **Mo** | **Ni** | **Re** | **Ta** | **W** |
|---|---|---|---|---|---|---|---|---|
| **Crystal used** | TAP | PET | PET | PET | PET | LiF | TAP | LiF |
| **Absorption edge** | $K_\alpha$ | $K_\alpha$ | $K_\alpha$ | $L_\alpha$ | $K_\beta$ | $L_\alpha$ | $M_\alpha$ | $M_\alpha$ |

EPMA scans were performed along the four arms (Fig. 4.4a) in steps of 4 μm to measure each element's concentration as a function of distance from the core (Fig. 4.4b). The arm lengths were normalized to compensate for slight differences. EPMA results showed that the concentrations of three elements, Cr, Mo, and Ta, remained roughly constant throughout the dendrite, because the p values of the linear-regression lines were statistically insignificant. Al and Co had low p values, indicating a possible linear correlation; however, the slopes suggested small compositional variations unlikely to affect attenuation noticeably, especially given their low electron density. Re decreased by 1.18 ± 0.09 wt.%, W decreased by 1.17 ± 0.06 wt.%, and Ni increased by 1.94 ± 0.13 wt.%, all of which were statistically significant ($p < 0.0001$). The intensity measured across the same four lines showed an increase of about 640 arbitrary units, or approximately 34%, also with $p < 0.0001$. The regression parameters of Fig. 4.4b are contained in Table 4.2.

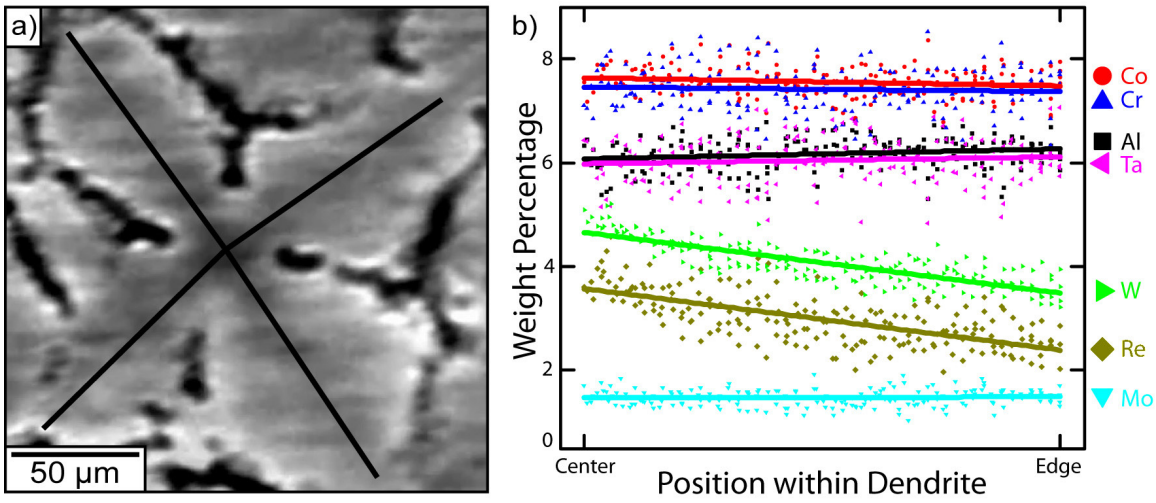


Fig. 4.4. EPMA-derived composition data along the four dendrite arms of the rightmost dendrite in Fig. 4.1b. (a) Scanned dendrite with lines showing the locations of the EPMA scans. (b) Plot of weight percentage as a function of distance from the center of the dendrite with the associated regression lines. Ni was excluded to keep the y-scale concise, and C, Hf, and Y were not measured due to their low concentration. Adapted from [2].

Table 4.2. Linear regression data for fits shown in Fig. 4.4b. Intensity intercept and slope are in arbitrary units. The element with significant regression lines of $p < 0.0001$ are highlighted in gray. SE stands for standard error.

| Element | Intercept (wt.%) | $SE_{intercept}$ (wt.%) | Slope (wt.%/pos) | $SE_{slope}$ (wt.%/pos) | p | $r^2$ |
|---|---|---|---|---|---|---|
| **Al** | 6.07 | 0.04 | 0.19 | 0.08 | 0.012 | 0.031 |
| **Co** | 7.64 | 0.04 | –0.16 | 0.07 | 0.023 | 0.026 |
| **Cr** | 7.46 | 0.06 | –0.09 | 0.10 | 0.379 | 0.004 |
| **Mo** | 1.47 | 0.02 | 0.02 | 0.04 | 0.530 | 0.002 |
| **Ni** | 64.0 | 0.12 | 1.94 | 0.13 | <0.0001 | 0.294 |
| **Re** | 3.57 | 0.05 | –1.18 | 0.09 | <0.0001 | 0.444 |
| **Ta** | 5.98 | 0.06 | 0.13 | 0.11 | 0.232 | 0.007 |
| **W** | 4.66 | 0.03 | –1.17 | 0.06 | <0.0001 | 0.677 |
| **Intensity** | 1890 | 102 | 640 | 48 | <0.0001 | 0.627 |

The change in intensity is caused by the segregation of electron-dense Re and W to the dendritic core and a corresponding drop in the Ni concentration. According to Eq. 3.11, the intensity as a function of distance from the core, *x*, is

$$I(x) = I_0 e^{-w_{Ni}(x)\cdot(\mu/\rho)_{Ni}\cdot\rho\cdot T} e^{-w_{Re}(x)\cdot(\mu/\rho)_{Re}\cdot\rho\cdot T} e^{-w_W(x)\cdot(\mu/\rho)_W\cdot\rho\cdot T} \quad [4.1]$$

where $I_0$ contains the contributions of the five constant elements, $w_i(x)$ is the weight percentage across the dendrite of the $i^{th}$ element, $(\mu/\rho)_i$ is the mass attenuation coefficient of the $i^{th}$ element, $\rho$ is the density, and $T$ is the thickness of the material. Rewriting Eq. 4.1 and using the attenuation coefficient, $\alpha_i$, instead of the mass attenuation coefficient and density:

$$I(x) = I_0 e^{-T\cdot\left(\frac{w_{Ni}(x)}{\alpha_{Ni}}+\frac{w_{Re}(x)}{\alpha_{Re}}+\frac{w_W(x)}{\alpha_W}\right)} \quad [4.2]$$

$w_i(x)$ for these three elements varies linearly, according to Table 4.2. It can be separated into its linear components with a slope, $\delta w_i$, and an intercept, $w_i$, and then inserted into Eq. 4.2:

$$w_i(x) \rightarrow \delta w_i \cdot x + w_i \quad [4.3]$$

$$I(x) = \underbrace{I_0 e^{-T\cdot\left(\frac{w_{Ni}}{\alpha_{Ni}}+\frac{w_{Re}}{\alpha_{Re}}+\frac{w_W}{\alpha_W}\right)}}_{constant} e^{-x\cdot T\cdot\left(\frac{\delta w_{Ni}}{\alpha_{Ni}}+\frac{\delta w_{Re}}{\alpha_{Re}}+\frac{\delta w_W}{\alpha_W}\right)} \quad [4.4]$$

$$I(x) = I_{center} e^{-x\cdot T\cdot\left(\frac{\delta w_{Ni}}{\alpha_{Ni}}+\frac{\delta w_{Re}}{\alpha_{Re}}+\frac{\delta w_W}{\alpha_W}\right)} \quad [4.5]$$

$I_{center}$ is the intensity at the center of the dendrite and includes $I_0$ and the exponential containing the intercept terms. Since $T \cdot \sum \delta w_i/\alpha_i < 1$, the exponential can be expanded as a Maclaurin series. Neglecting higher-order terms, Eq. 4.5 becomes

$$I(x) = I_{center}\left[1 - x \cdot T \cdot \left(\frac{\delta w_{Ni}}{\alpha_{Ni}} + \frac{\delta w_{Re}}{\alpha_{Re}} + \frac{\delta w_W}{\alpha_W}\right)\right] \quad [4.6]$$

$$I(x) = I_{center} - \underbrace{I_{center} \cdot \left(\frac{\delta w_{Ni}}{\alpha_{Ni}} + \frac{\delta w_{Re}}{\alpha_{Re}} + \frac{\delta w_W}{\alpha_W}\right)}_{constant} \cdot T \cdot x \quad [4.7]$$

$$I(x) = I_{center} + \Delta \cdot T \cdot x \quad [4.8]$$

where $\Delta \cdot T$ is the slope of the intensity profile measured from the center to the edge. According to Eq. 4.8, the intensity should vary linearly across the same region for small, linear changes in the weight percentages of Ni, Re, and W. The intensity did indeed vary linearly (Table 4.2), so $\Delta \cdot T = 640 \pm 48$, and composition values have a direct one-to-one correspondence with the intensity.

Only one dendrite was scanned with EPMA, but the results can be extended to all other dendrites. The grayscale intensities at the centers of the six dendrites in Fig. 4.1b were measured by averaging the intensity in a circle with a 20-pixel diameter; the results were statistically equivalent (Fig. 4.5). The intensity was determined purely by absorption, so all of the dendritic cores had a similar composition, barring unlikely and unexpected combinations of other elements. A 2D color-coded map of elemental concentration for Fig. 4.1b revealed a strong segregation of Re and W and rarefaction of Ni at center of dendrites, with fluctuations through the branches over a 600-µm by 400-µm area (Fig. 4.6). The dendritic/interdendritic boundaries appear bright, but here the intensity is enhanced by phase contrast and does not indicate a spike in concentration. Some interdendritic regions, such as those between the lower-right and central dendrite, had brighter intensities on the order of the dendrites. The color map assigned them a misleading composition, since their intensity is not solely based on the change in Ni, Re, and W.

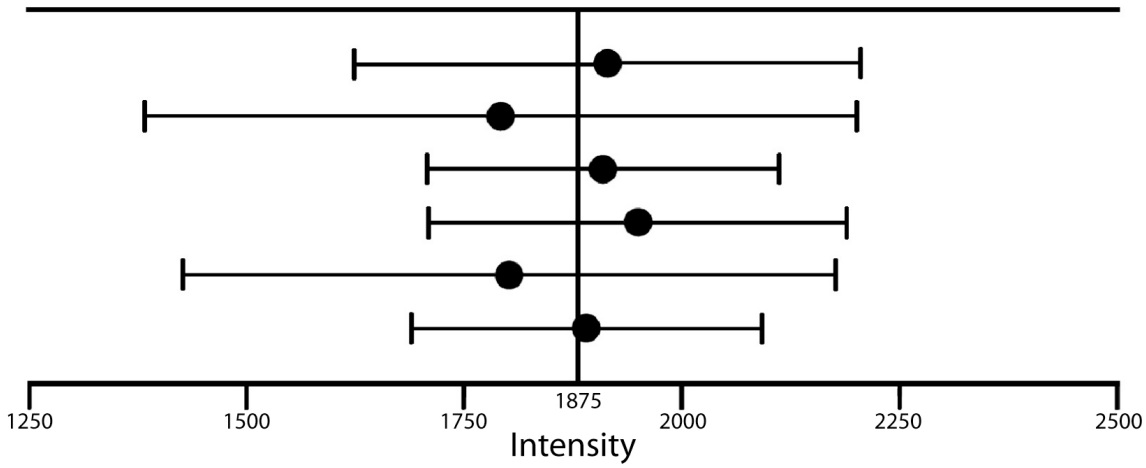


Fig. 4.5. The mean and 95% confidence intervals for the intensity of six different dendritic cores. Data were collected from a circular region (diameter = 20 pixels) at the center of each dendrite. The mean intensity did not differ significantly among the dendrites. Adapted from [2].

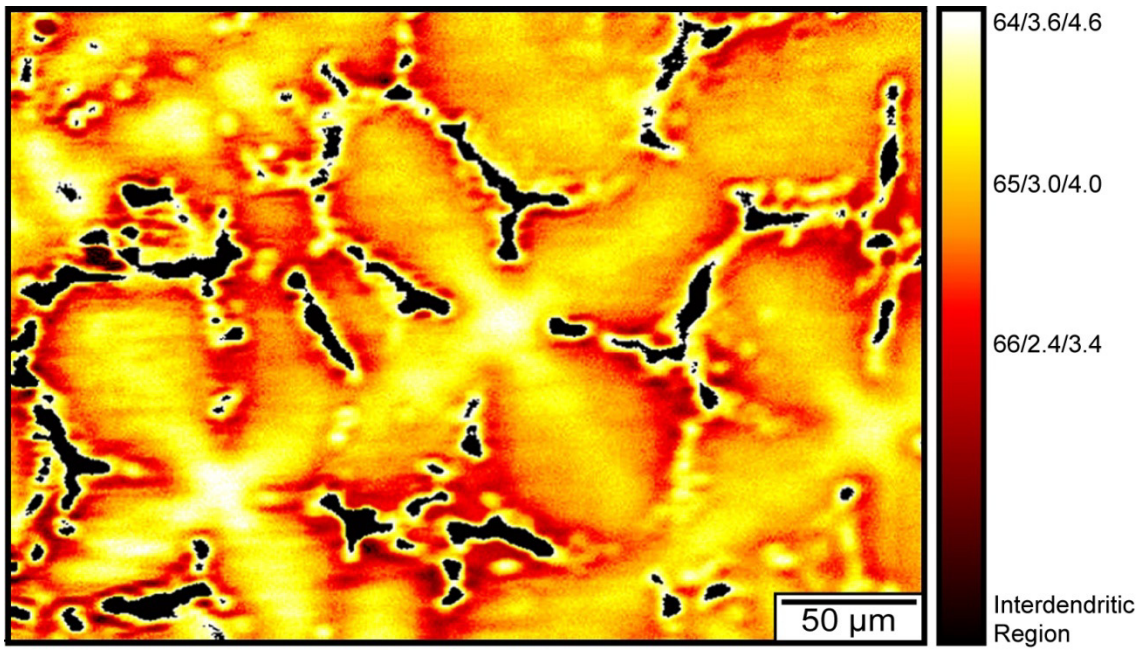


Fig. 4.6. Composition map across the dendrites of Fig. 4.1b. The scale on the right indicates the wt.% of Ni/Re/W. Re and W segregated to the core and displaced some Ni. The concentrations assigned to the interdendritic regions are not significant. Adapted from [2].

The results of the EPMA scan are not just useful for the particular superalloy sample studied. For different thicknesses of René N5 cut along the same orientation, only the thickness, T, would change and affect the slope of the intensity profile. The linear one-to-one correspondence would still exist, provided the exponential in Eq. 4.5 was small enough for a series expansion; if not, increasing the energy would increase $\alpha$ to keep the exponential small. Another superalloy type with a different composition would require a new set of EPMA scans, however, since the presence of different elements may affect the segregation characteristics. Multiple one-dimensional EPMA scans can be quickly converted into a 2D map of the composition and segregation on a scale appropriate to the dendritic microstructure.

## 4.3 Mosaicity and Dislocation Density

The dendritic cores do not necessarily solidify perfectly parallel to one another. During nucleation, dendrites may emerge from the helical starter with misalignments that persist throughout solidification. Looking at a sample taken parallel to the casting direction (Fig. 4.7a), the misalignment was 1.5° between the left and center dendrites and 0.5° between the center and right dendrites, with an uncertainty of about 0.5°. For 21 pairs of adjacent dendrites measured in this way, the median misalignment was 1.0 ± 0.5° (Fig. 4.7b). While most misalignments were less than a few degrees, some dendrites were significantly misaligned by up to 7.5 ± 0.5°. These angles do not necessarily indicate crystallographic deviations with respect to the nominal Bragg angle, but since one dendrite cannot grow through another dendrite, this may eventually lead to mosaicity. Any misorientations will be accommodated by dislocations in the last liquid metal to solidify – the interdendritic region.

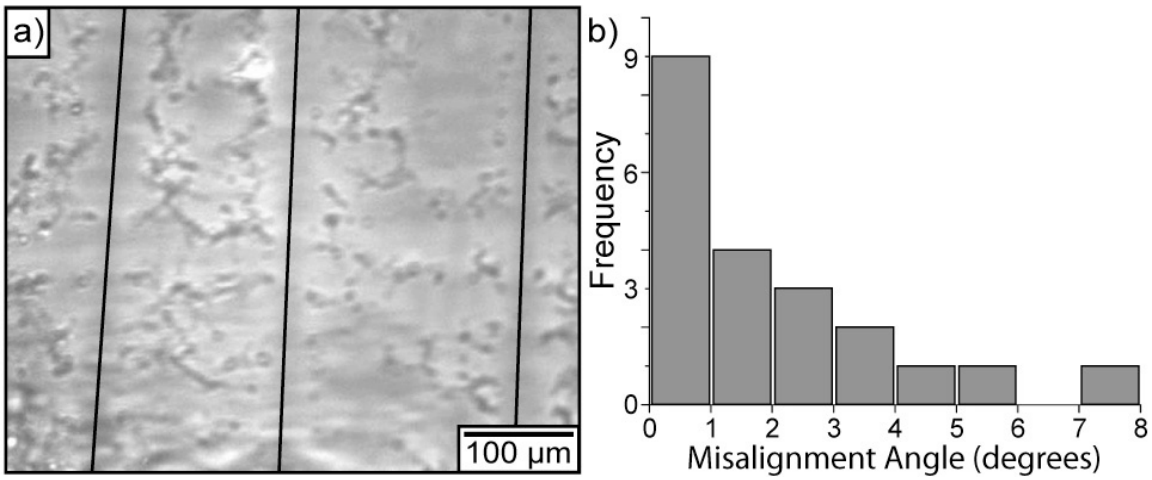


Fig. 4.7. (a) Dendritic cores viewed parallel to the casting direction. They are not perfectly parallel to one another, leading to crystallographic misorientations. (b) Misalignments for 21 dendrites from images similar to (a). The median was 1.0 ± 0.5° and the maximum was 7.5 ± 0.5°. Adapted from [2].

The crystallographic misorientation is best studied via diffraction contrast in samples cut perpendicular to the casting direction. The Bragg angle position is uniquely determined by the crystallographic orientation according to Bragg's law (Eq. 3.30) in the absence of uniform stress, so measuring the diffraction angle for adjacent dendrites is directly related to the dislocation density in the intervening interdendritic regions. The associated nadir width is a convolution of non-uniform stresses, instrumental effects, longitudinal coherence, and dislocations, as discussed in Section 3.3.2. These effects could not easily be separated, so only the Bragg angle position is considered in this section.

The now-familiar sample shown in Fig. 4.1b was rotated about the [100] axis to the expected (022) Bragg angle, $\theta_{B,exp}$, located 8.80° away from normal incidence, assuming no miscut (Eq. 3.32). The sample was rocked by ±1.50° around the Bragg angle in steps of 0.05° to measure the intensity at each pixel as a function of angle. Looking at a single dendrite and following its intensity (Fig. 4.8), at the Bragg angle the intensity dropped significantly with an appreciable nadir width of 0.17 ± 0.04°. The dendrite did not darken uniformly, but rather the shadow started on the outside and moved inward

before disappearing over four frames, or 0.15 ± 0.04. This corresponds to a lattice-parameter distortion of

$$\frac{\Delta a}{a} = \left| 1 - \frac{sin(\theta_{edge})}{sin(\theta_{center})} \right| = 0.17 \pm 0.01\% \quad [4.9]$$

This small change corresponds to the linear variation in composition of Ni, Re, W from the center out to the edge of the dendrite. The angular step size is too low to see clearly the bimodal distribution from the lattice misfit of the γ and γ́ phases, but the step size still provides sufficient information for details on mosaicity. Assuming a 0.2% to 0.3% lattice misfit [9], the second nadir should be located about 0.05° to 0.10° to the right of the minimum (Eq. 3.32), where some asymmetry is visible (Fig. 4.8b). In the rocking curves of the subsequent chapters, the step size was decreased to 0.005°.

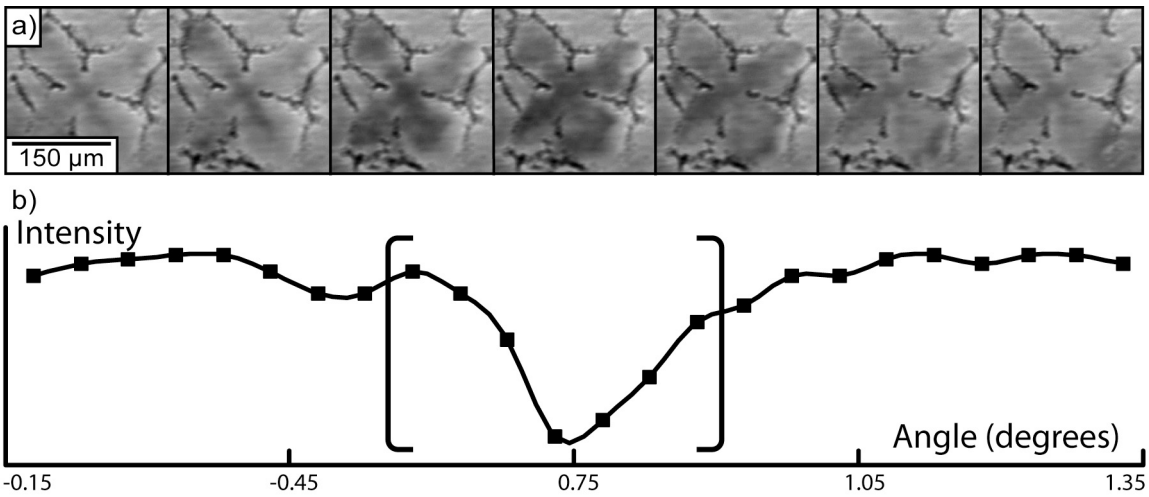


Fig. 4.8. Diffraction data for the center pixel of the rightmost dendrite of Fig. 4.1b. (a) Images corresponding to the Bragg angle and up to 0.15° on either side. (b) The intensity is plotted as a function of deviation from the nominal Bragg angle with a spline fit, and the bracket encloses the seven data points derived from the images in (a). Other images at smaller and larger angles were not shown, as the intensity did not vary much outside this envelope for that particular dendrite.

Many dendrites darkened substantially due to diffraction when the sample was rotated to $\theta_{B,exp}$; however, some remained bright, indicating tilt misorientations with respect to the [001] axis as seen in Fig. 4.7. Misoriented dendrites diffracted at $\theta_{B,dend}$, and the deviations, $\varphi = \theta_{B,dend} - \theta_{B,exp}$ , ranged from -0.25 ± 0.03° up to 1.20 ± 0.03°.

Though significant in terms of dislocation density, these boundaries are all low-angle (<10°) and unlikely to act as crack-initiation sites during high-cycle fatigue [10]. A map of $\varphi$ was superimposed onto Fig. 4.1b (Fig. 4.9b) to show the mosaicity among the dendrites. The separation is remarkably sharp, falling precisely within the interdendritic regions.

Since dislocations are known to aggregate in the interdendritic regions, the spacing of the dislocations, $d$, in a low-angle tilt boundary between two dendrites separated by $\varphi$, is given by

$$d = \frac{b}{|\varphi|} \qquad [4.10]$$

where $b$ is the Burgers vector [11]. With a slip system along <110> in a face-centered cubic crystal lattice,

$$b = \frac{a}{2}\sqrt{1^2 + 1^2 + 0^2} = \frac{a}{\sqrt{2}} \qquad [4.11]$$

where $a$ is the lattice parameter. Considering the widely spaced dendrites, a net dislocation density is

$$\rho = \frac{1}{d \cdot PDAS} = \frac{\varphi\sqrt{2}}{a \cdot PDAS} \qquad [4.12]$$

Between the center and lower-left dendrite of Fig. 4.9, P$DAS$ ≈ 225 ± 10 μm, $a$ = 3.58 Å, $\varphi$ = 1.00° ± 0.05°, and therefore $\rho$ ≈ (3.1 ± 0.2) × $10^7$ dislocations/cm$^2$. Between the center and lower-right dendrite, $\rho$ ≈ (0.7 ± 0.2) × $10^7$ dislocations/cm$^2$. These results are consistent with previous studies [12], which involved counting dislocations from very localized transmission electron microscopy (TEM) scans. Making direct measurements in this manner, though, is significantly easier and does not require careful preparation of TEM microfoils at each dendrite boundary.

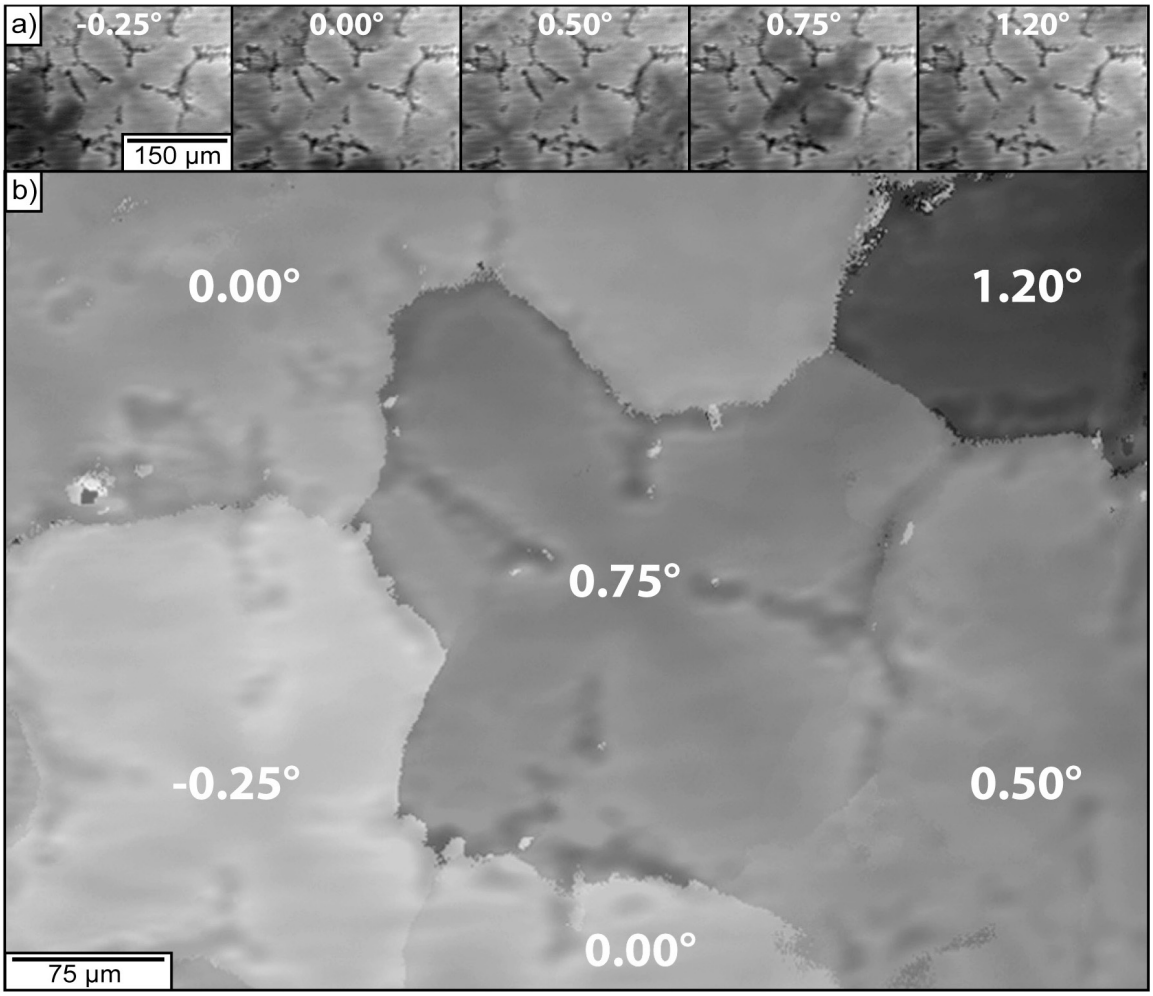


Fig. 4.9. Bragg-nadir position across five dendrites. (a) Images at the diffraction angles of the five dendrites within the same field of view. Some diffract more strongly than others. (b) Semitransparent map of Bragg angle superimposed onto a portion of Fig. 4.1b. All angles are measured with respect to the nominal (220) Bragg angle and are ±0.03°.

## 4.4 Discussion

The work presented in this chapter serves two vital functions. First, it illustrates the host of features that can be imaged non-destructively via absorption, phase, and diffraction contrast at a high-brilliance synchrotron source. With such a breadth of microstructural features spanning many length scales, much information is inaccessible simultaneously with a single conventional imaging technique. For example, scanning-electron and optical microscopy image at or very near the surface, but they cannot provide information on dislocations easily. Conversely, TEM can distinguish individual dislocations, but only after cumbersome preparation of very thin foils that are not

suited to the larger scale of the dendrites. Any internal imaging must be *ex situ* and destructive, such as serial sectioning [13], limiting the *in situ* capabilities during dynamic fatigue-crack propagation experiments. Synchrotron radiography overcomes many of these limitations, as demonstrated in this chapter, although in the current setup it cannot achieve the same spatial resolutions as electron microscopy. Emerging technologies like transmission x-ray microscopy have better spatial resolutions down to tens-of-nanometer, although they generally have a limited field of view without rastering the beam or sample [14-16]. Many synchrotron sources are upgrading imaging beamlines to expand their fields of view and spatial resolutions to compete with electron microscopy. Some of the new technological advances for imaging beamlines are discussed in Chapter 7.

Second, this chapter also discusses two important aspects of superalloys: non-uniform intradendritic composition and dislocation density. Refractory-element additives continue to push the operating-temperature limit in nickel-base superalloy engine components for even higher performance [1,17-18], and their segregation is unavoidable during growth and solidification due to thermodynamically driven partitioning to the solid and liquid phases. The intradendritic absorption contrast is consistent with the well-known concentration of Re and W to the cores in René N5, as verified with EPMA; additionally, heavy-element segregation distorts local lattice parameters across the dendrites. Since lattice-parameter misfit between the matrix and precipitate has a strong influence on directional coarsening and precipitate morphology during creep, this technique could provide new insights on the inhomogeneous deformation behavior at the dendritic scale.

Diffraction contrast proved an effective probe of mosaicity across a large field of view, from which the dislocation density within the interdendritic regions was calculated. While dislocations at low-angle boundaries on the order of single degrees have been reported previously, they have been based on very localized TEM measurements [12]. The grown-in dislocation networks affect the material properties during the early stages of creep, as they serve as sources of further dislocations that

percolate into the dislocation-free dendritic cores [12]. An *in situ* probe capable of imaging dislocations across a large area via diffraction is useful for dynamic studies of creep deformation and fatigue-crack propagation.

Lastly, carbides within the interdendritic regions are clearly visible due to enhancement from phase contrast (Fig. 4.2). Carbides often serve as fatigue initiation sites, particularly during high-cycle fatigue [19]. Techniques for *in situ* interrogation of strain localization and crack initiation near carbides are limited, particularly when the carbide is internal. Since synchrotron imaging is optimal for *in situ* dynamic studies, the results of this section will be extended into high-cycle fatigue in the coming chapters to not only visualize microstructure and strain but also crack initiation and propagation.

## 4.5 References


1 Pollock, T. M. & Tin, S. Nickel-based superalloys for advanced turbine engines: Chemistry, microstructure, and properties. *J Propul Power* **22**, (2006).

2 Husseini, N. S. *et al.* Mapping single-crystal dendritic microstructure and defects in nickel-base superalloys with synchrotron radiation. *Acta Mater* **56**, (2008).

3 Kurz, W. & Fisher, D. J. *Fundamentals of solidification*. (Trans Tech Publications, 1986).

4 Elliott, A. J. *et al.* Directional solidification of large superalloy castings with radiation and liquid-metal cooling: A comparative assessment. *Metall Mater Trans A* **35**, (2004).

5 Cloetens, P., Barrett, R., Baruchel, J., Guigay, J. P. & Schlenker, M. Phase objects in synchrotron radiation hard x-ray imaging. *J Phys D Appl Phys* **29**, (1996).

6 Cloetens, P. *et al.* Observation of microstructure and damage in materials by phase sensitive radiography and tomography. *J Appl Phys* **81**, (1997).

7 Warren, J. A. & Boettinger, W. J. Prediction of Dendritic Growth and Microsegregation Patterns in a Binary Alloy Using the Phase-Field Method. *Acta Metall Mater* **43**, (1995).

8 CAMECA SAS, Gennevilliers, France.

9 Pollock, T. M. & Field, R. D. Dislocations and high-temperature plastic deformation of superalloy single crystals. *Dislocations in Solids* **11**, (2002).

10 Miao, J., Pollock, T. M. & Wayne Jones, J. Microstructural extremes and the transition from fatigue crack initiation to small crack growth in a polycrystalline nickel-base superalloy. *Acta Mater* **60**, (2012).

11 Lalena, J. N. & Cleary, D. A. *Principles of Inorganic Materials Design*. (John Wiley, 2010).

12 Pollock, T. M. & Argon, A. S. Creep Resistance of CMSX-3 Nickel-Base Superalloy Single-Crystals. *Acta Metall Mater* **41**, (1993).

13 Echlin, M. P., Husseini, N. S., Nees, J. A. & Pollock, T. M. A new femtosecond laser-based tomography technique for multiphase materials. *Adv Mater* **23**, (2011).
14 Neuhausler, U. *et al.* X-ray microscopy in Zernike phase contrast mode at 4 keV photon energy with 60 nm resolution. *J Phys D Appl Phys* **36**, (2003).
15 Zschech, E., Yun, W. B. & Schneider, G. High-resolution X-ray imaging - a powerful nondestructive technique for applications in semiconductor industry. *Appl. Phys. A-Mater. Sci. Process.* **92**, (2008).
16 Diaz, A. *et al.* Quantitative x-ray phase nanotomography. *Phys Rev B* **85**, (2012).
17 Walston, S., Cetel, R., MacKay, K., O'Hara, D., Duhl, D., Dreshfield, R. *Superalloys*. (TMS, 2004).
18 Sato, A. *et al.* A 5th generation Ni-base single crystal superalloy designed for the combination of excellent oxidation resistance and creep strength at elevated temperatures. *J Jpn Inst Mat* **70**, (2006).
19 Nicholas, T. *High Cycle Fatigue: A Mechanics of Materials Perspective*. (Elsevier, 2006).

# CHAPTER 5
# IMAGING MINIMALLY OPENED FATIGUE CRACKS

Fatigue-crack propagation in the very high-cycle fatigue (VHCF) regime is like a heart attack: both are brought on by a lifetime's accumulation of dislocations or plaque, aggravated by stress, predictable to a degree based on history and environment, and a small but very important fraction of the total lifetime. Moreover, both can be fatal. Early detection, whether before or very soon after initiation, is essential to prevent material or cardiac failure. As demonstrated by the phase-contrast simulations of Section 3.2, coherent x rays are exquisitely sensitive to subtle crack openings; dislocations and slip bands discussed in Section 3.3 may foreshadow crack initiation and the propagation path even before fully developed cracks form. The studies described in this chapter and the following chapter exploit all three contrast mechanisms in synchrotron x-ray imaging for dynamic studies of fatigue-crack initiation, from the embryonic stages as a series of slip bands to the rapid growth regime. The results provide insight into crack growth and suggest possible field-diagnostic applications for detecting incipient fatigue damage in turbine blade materials early enough that, like a heart, it can still be treated or replaced.

## 5.1 A Crack in Time

CMSX-4, René N4, and René N5 superalloy bars were grown via directional solidification in a Bridgman-type furnace, with some René N5 samples solidified with the liquid-metal-cooling (LMC) process [1]. Dogbone-shaped microspecimens were cut parallel to the (100) plane with the [001] casting direction along the length of the specimen and [010] across the width (Fig. 2.2). A few samples were instead cut perpendicular to the [001] casting direction to see the four-branched secondary dendrite arms. All samples were ground and hand-polished to thicknesses between

about 150 and 200 μm and notched with a femtosecond laser at the edge of the 2-mm-thick gauge section. The exact notch length and height varied among the samples, but it was approximately 300-μm long and 50-μm high. Specific relevant details of the various superalloy samples discussed in this chapter are listed in Table 5.1.

Table 5.1. Superalloy samples discussed in this chapter with relevant details. The orientation specifies whether the sample is cut parallel or perpendicular to the [001] solidification direction. $\beta$ and $\gamma$ are inclination angles with respect to the notch in the (100) and (010) planes, respectively, and are illustrated in Fig. 5.10. RN4 and RN5 refer to René N4 and René N5, respectively. BM is a Bridgman-solidified sample.

| Superalloy and number | Orientation | Thickness (μm) | Notch length (μm) | Δσ (MPa) | β (°), ±1° | γ (°), ±1° | Fracture plane |
|---|---|---|---|---|---|---|---|
| CMSX-4 1 | parallel | 178 | 262 | 102.8 | 44 | 38 | $(1\bar{1}1)$ |
| CMSX-4 3 | parallel | 170 | 468 | 103.6 | 30 | 39 | $(1\bar{1}1)$ |
| CMSX-4 7 | parallel | 159 | 494 | 101.6 | 30 | 39 | $(1\bar{1}1)$ |
| CMSX-4 8 | parallel | 167 | 436 | 142.8 | 29 | 40 | $(1\bar{1}1)$ |
| CMSX-4 9 | parallel | 173 | 278 | 135.4 | 30 | 43 | $(1\bar{1}1)$ |
| CMSX-4 10 | parallel | 166 | 337 | 173.0 | 29 | 36 | $(1\bar{1}1)$ |
| CMSX-4 20 | parallel | 211 | 355 | 90.0 | 29 | 40 | $(1\bar{1}1)$ |
| CMSX-4 24 | parallel | 198 | 344 | 96.8 | 45 | 40 | $(1\bar{1}1)$ |
| CMSX-4 33 | parallel | 200 | 363 | 190.4 | 30 | 39 | $(1\bar{1}1)$ |
| CMSX-4 34 | parallel | 213 | 383 | 105.2 | 30 | 36 | $(1\bar{1}1)$ |
| CMSX-4 35 | parallel | 199 | 385 | 133.1 | 28 | 41 | $(1\bar{1}1)$ |
| RN4 BM 1 | perpendicular | 200 | 263 | 90.0 | n/a | n/a | n/a |
| RN4 BM 2 | perpendicular | 137 | 389 | 119.9 | n/a | n/a | n/a |
| RN5 BM 1 | parallel | 175 | 357 | 108.8 | n/a | n/a | n/a |

Microfoil specimens were rigidly mounted to the Ti-6Al-4V carrier and loaded in the portable ultrasonic fatigue apparatus described in detail in Section 2.2 [2]. The apparatus itself was installed in transmission geometry at Sector 32-ID-C of the Advanced Photon Source (APS) for imaging with 23-keV x-ray radiation. This is a higher energy than that used in Chapter 4, and though it does not have the nickel $K_\alpha$ absorption-edge effect, the interregional attenuation length between dendrites and interdendritic regions is still noticeably different. More importantly, this energy reduces the exposure times from greater than 1.0 seconds for 100-μm-thick samples to about 0.2 seconds or less for 200-μm thicknesses. The unfocused-beam area was over six times larger than at Sector 7, providing a field of view of approximately 1800 μm x 1500

μm with a spatial resolution of about 1.5 μm/pixel. Fatigue testing involved a duty cycle that was increased while awaiting crack initiation and decreased for fast-moving cracks accordingly to provide about one pixel of crack growth per image. All images were acquired during the rest phase of the duty cycle. Note that most images presented in this chapter are background-corrected and have their contrast and brightness adjusted from the original radiograph for easy viewing. Intensity counts and contrast values used in quantitative calculations were derived from the original uncorrected images.

Testing in the VHCF regime requires many low-stress cycles with a stress-intensity factor (SIF) range along the loading axis, $\Delta K_I$, near the initiation threshold, $\Delta K_{th}$. Room-temperature threshold values were measured between 3 and 7 MPa·m$^{1/2}$, which matched previously reported values in a similar nickel-base single-crystal superalloy, PWA1484 [3], although the occasional stubborn samples required an even higher $\Delta K$ above 7 MPa·m$^{1/2}$ for initiation. The stress amplitude at the initiation threshold was

$$\Delta\sigma = \sigma_{max} - \sigma_{min} = \frac{\Delta K_I}{\sqrt{\pi l}} \qquad [5.1]$$

where $\Delta K_I$ was assumed to be at the lowest possible threshold SIF of 3 MPa·m$^{1/2}$ for the slowest growth rate. For CMSX-4 1 with a notch length, $l$, of 262 μm, Eq. 5.1 yielded an initial Δσ = 102.8 MPa. Since all tests were in tension at a stress amplitude ratio of $R = \sigma_{min}/\sigma_{max}$ = 0.1, $\sigma_{mean}$ = 62.8 MPa. Given an elastic modulus of 115 GPa [4], these stresses corresponded to strains of $\varepsilon_{mean}$ = 546 με and $\Delta\varepsilon$ = 894 με. All fatigue tests were displacement-controlled, so $\Delta K_I$ increased as the crack lengthened.

Room-temperature crack propagation in the CMSX-4 1 sample showed several of the important features of this method (Fig. 5.1). The dendritic microstructure appeared framed by the hole through the carrier. Primary and secondary dendrites were oriented approximately vertically and horizontally, respectively, but they were slightly tilted away from the load axis by about 5° to 10°. Finite-element modeling, discussed in Section 5.4, accounted for this difference between the specimen and crystallographic coordinate systems. Scattered throughout the material in the interdendritic regions were carbides, pores, and inclusions, which produce stress concentrations at locations that might have been crack-initiation sites [5] were it not for the much larger edge notch.

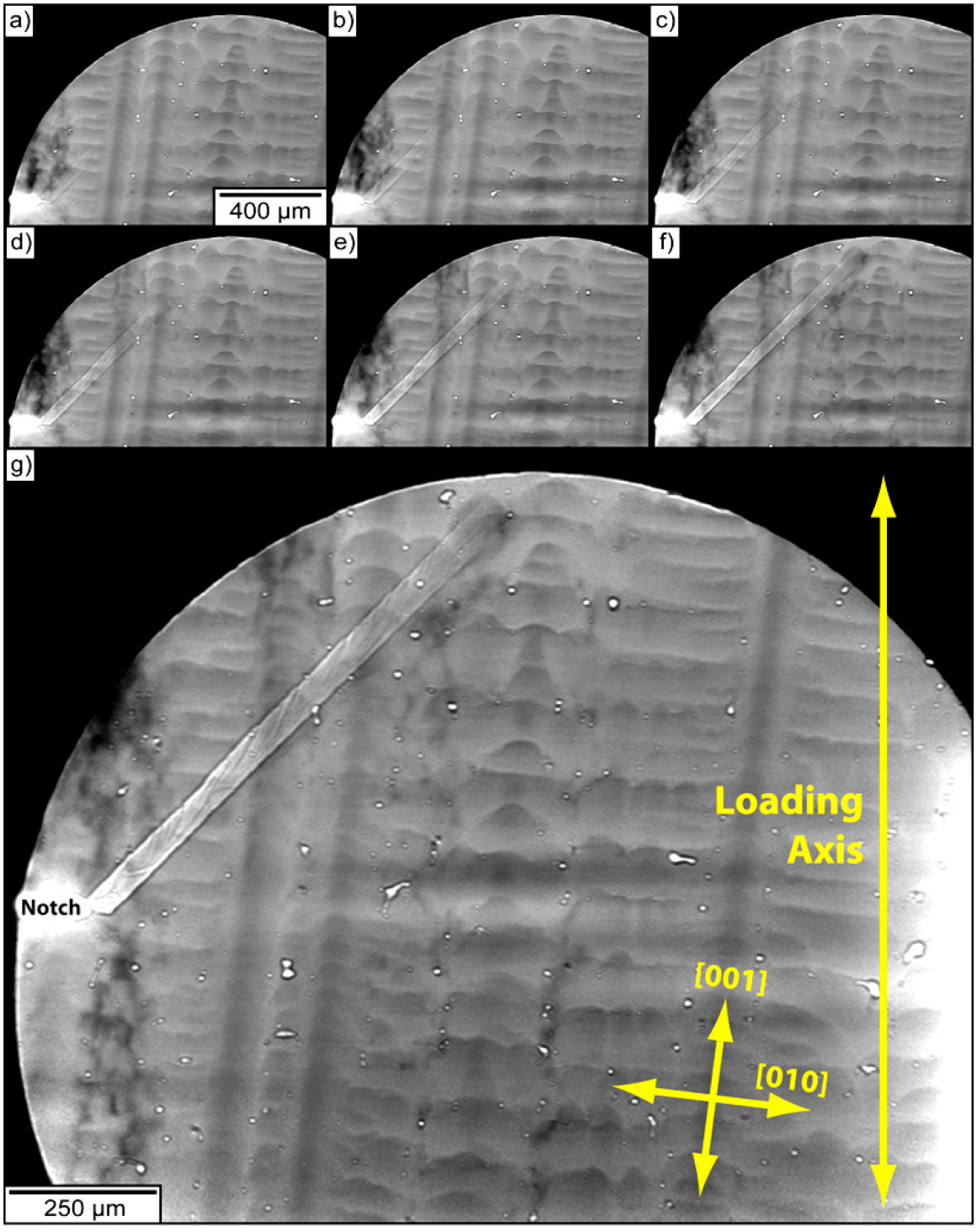


Fig. 5.1. Fatigue-crack propagation in CMSX-4 1. (a-f) The crack initiated from the notch and grew along a {111} plane over 2.01 million cycles. (g) The final image with crystallographic and loading axes labeled.

The fatigue crack in CMSX-4 1 required 1.71 million cycles to initiate from the edge notch with an initial $\Delta K_{th}$ = 3 MPa·m$^{1/2}$ and then another 2.01 million cycles to propagate crystallographically along a {111} plane to a final length of nearly 2 mm [2,6]. The growth rate and crack character were insensitive to the dendritic microstructure, as is expected at room temperature in monocrystalline materials [7]. The crack appeared as a thick line, because radiography projects the three-dimensional (3D) information onto the two-dimensional (2D) imaging plane (Fig. 5.2). The front and rear surface cracks are on either side of the line, with the interfacial roughness in between them; these features are only visible with phase contrast and will be discussed in more detail in later sections.

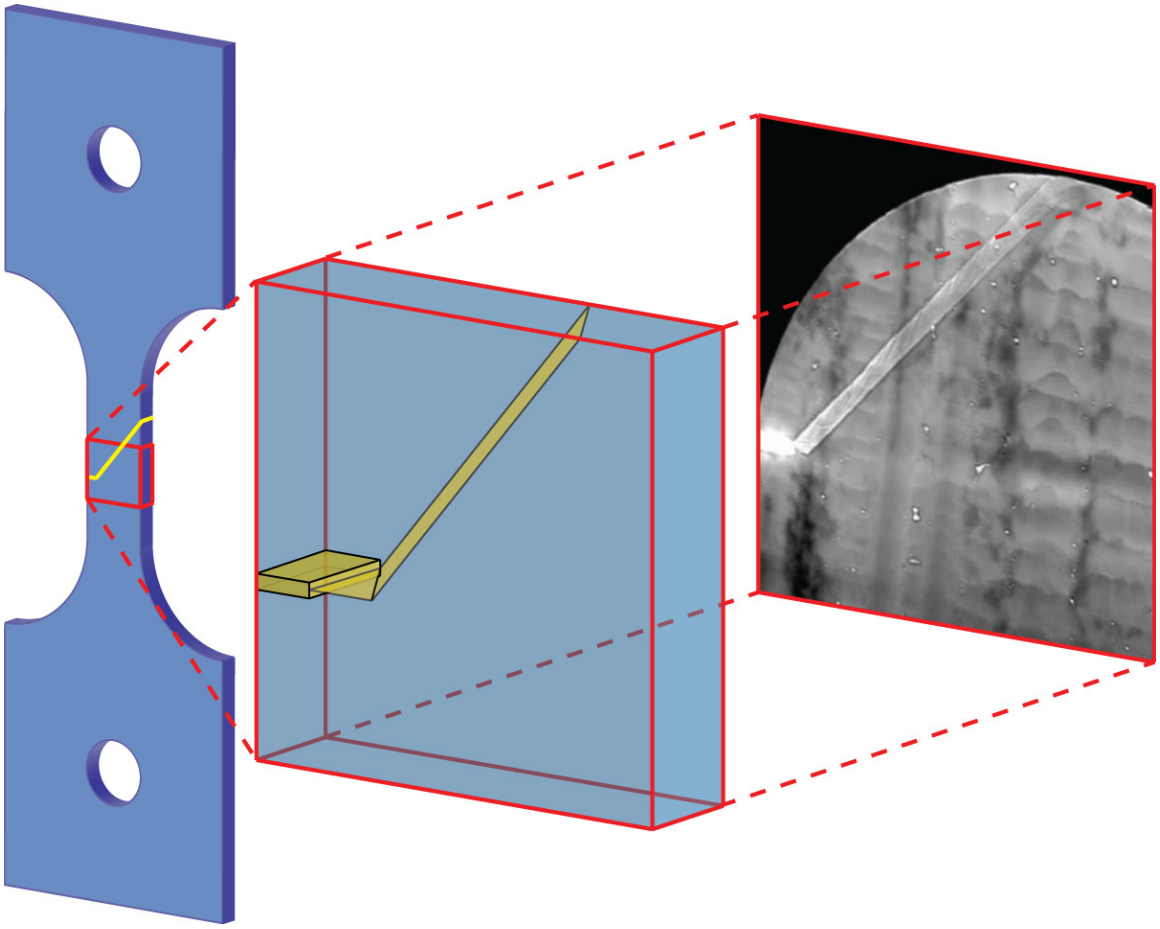

Fig. 5.2. Schematic representation of the 2D projection of the 3D crack structure. The two surface cracks are projected onto a single plane, with the interfacial roughness appearing in between them.

Exposures were captured after the 100-ms pulse phase and during the 2000-ms rest phase of the duty cycle. A total of 1,005 images were recorded in 2,000-cycle increments for micron-scale crack evolution. Real-time results displayed on the external computer facilitated dynamic control of the testing conditions. For example, if the crack grew more than a couple pixels per image, the pulse duration was decreased for a better cycle resolution; alternatively, if the crack did not initiate or ceased growing mid-propagation, the displacement amplitude was raised. If something unexpected happened, like a crack shifting planes or arresting at an inclusion, the test was paused to map fatigue-induced plasticity with diffraction contrast. This level of real-time feedback and versatile control during testing is a unique aspect of this imaging technique.

## 5.2 Crack Opening

A simplistic definition of a crack is a separation between two sections of a material, and this separation provides absorption contrast from the change in the optical path length with respect to an uncracked region. Crystallographic cracks grow as a combination of three fracture modes (Fig. 5.3), even though the loading axis is only along the Mode-I direction [2-3,8]. The contributions of shearing forces keep the total crack opening small, and thus absorption contrast alone is inadequate to image all details of a crack, particularly at the tip. The change in absorption, though, can still provide an estimate of the amount of opening, by comparing the intensity in a region before and after cracking.

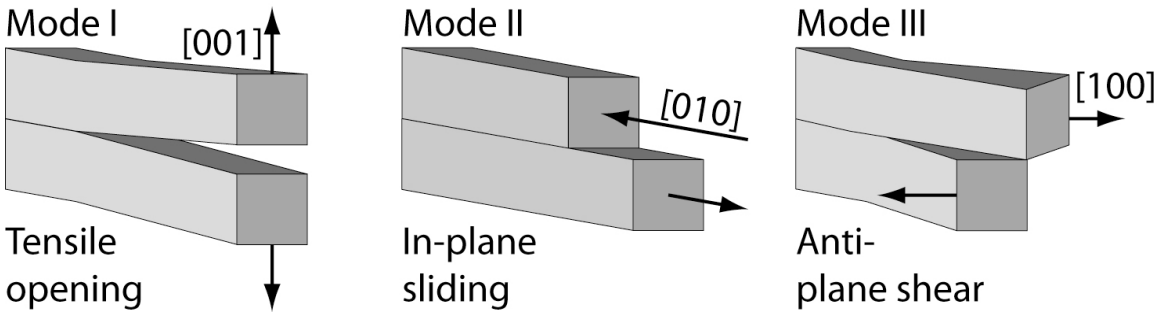


Fig. 5.3. The three fracture modes in a cubic system. A crystallographic crack grows as a combination of all three of these modes.

Looking at the radiograph in Fig. 5.1 of CMSX-4 1, the intensity near the notch between the surface cracks is clearly greater than that near the crack tip. This intensity change is an absorption effect, not a phase-contrast effect, and caused by crack opening. In an uncracked sample with no opening (Fig. 5.4a), the intensity from absorption is

$$I_{uc} = I_0 e^{-T/\alpha} \quad [5.2]$$

In a cracked sample (Fig. 5.4b), the optical path length decreases as the crack opens and the intensity increases:

$$I_c = I_0 e^{-(T-\Delta_z)/\alpha} \quad [5.3]$$

$I_0$ is the initial intensity, which remains relatively constant at a synchrotron running with a constant electron-ring current (top-off mode), such as the APS. $T$ is the thickness of the sample (178 μm), $\Delta_z$ is the opening in the through-thickness direction, and $\alpha$ is the attenuation length of the CMSX-4 superalloy (~50 μm). Combining Eqs. 5.2 and 5.3 and solving for $\Delta_z$:

$$\Delta_z = \alpha \cdot \ln\left(\frac{I_c}{I_{uc}}\right) \quad [5.4]$$

$I_c$ and $I_{uc}$ are defined as counts per second. Since the exposure time was constant throughout the test, the intensity ratio is equivalent to the pixel-count ratio.

The through-thickness angle of inclination, $\varphi$, of the crystallographic crack was determined as the arctangent of the projected distance between points A and B in Fig. 5.4b and the thickness of the sample. The crack opening, $\Delta_T$, along the transverse plane of the sample and perpendicular to the surface crack is defined as

$$\Delta_T = \alpha \cdot \ln\left(\frac{I_c}{I_{uc}}\right) \tan\varphi \quad [5.6]$$

$\Delta_T$ is plotted alongside $\Delta_Z$ as a function of distance away from the notch with intensity measured from a line midway between the two surface cracks (Fig. 5.4c). The data were smoothed with a 25-μm median filter to remove high-frequency noise. Low-frequency oscillations were due to phase-contrast effects from the roughness on the fracture surface. All measurements were performed when the sample was under a tensile stress of 62.8 MPa.

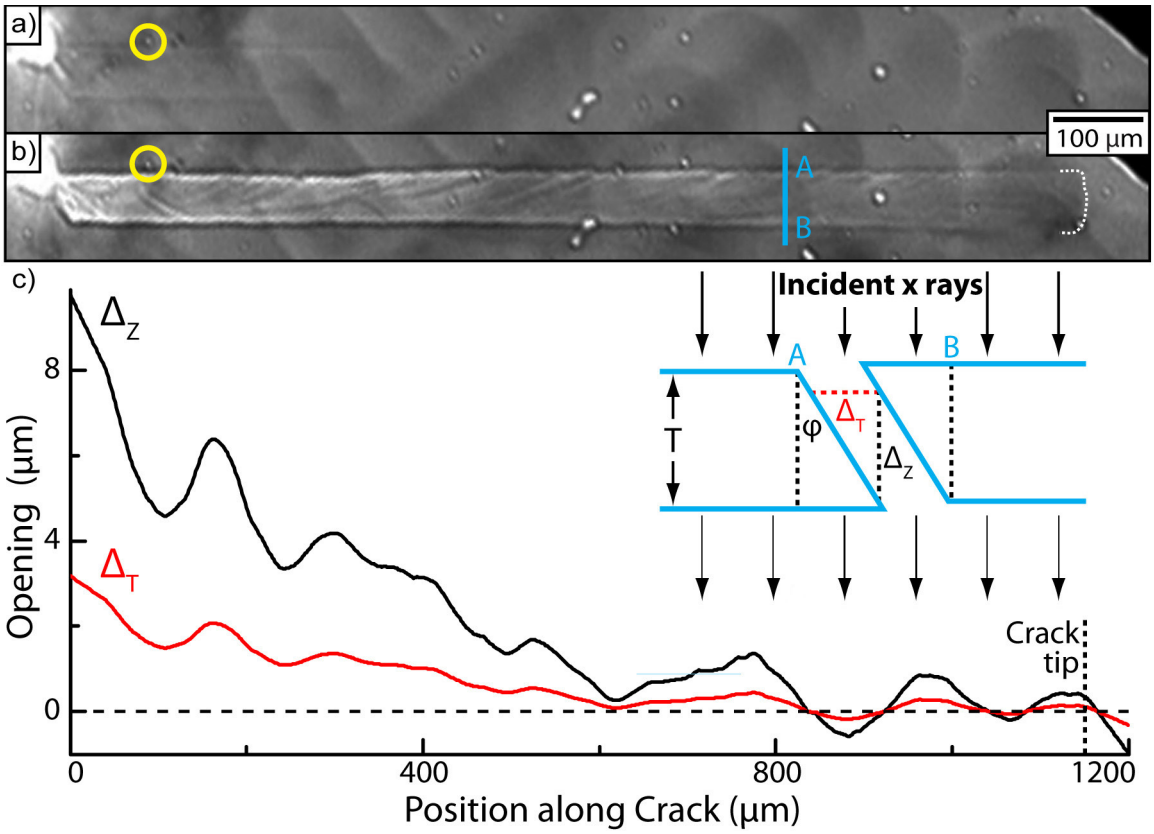


Fig. 5.4. Images taken (a) early in crack growth and (b) before the crack left the field of view for CMSX-4 1 while under a 62.8 MPa tensile stress. The crack tip is outlined in white in (b). The images are rotated by 45° compared to Fig. 5.1, so that the crack-propagation path is horizontal for easier comparison. The carbide circled in yellow moves slightly between (a) and (b) and is used for an alternate method of crack-opening measurement. (c) Crack opening as a function of position along the crack after smoothing with a median filter to remove high-frequency noise. Phase-contrast effects from the interfacial crack roughness causes low-frequency oscillations in the intensity that do not correspond to opening. The inset (not to scale) represents a cross-section along $\overline{AB}$ in (b) showing as dotted lines the sample thickness, $T$, and components of opening, $\Delta$, as well as the through-thickness inclination angle $\varphi$.

The intensity perpendicular to the propagation direction (e.g., between points A and B in Fig. 5.4b) did not change significantly; therefore, $\Delta_z$ was assumed uniform, and $\Delta_x$ provided a reasonable approximation of the transverse opening. Although some slight bowing of the sample was possible as the crack lengthened and was subjected to multiple stress components, particularly when the crack was nearly the length of the gauge section, it contributed very little to $\Delta_Z$ as seen by the x rays.

As the crack opened in the through-thickness direction, features on the surface moved in the transverse plane, providing an alternative verification of the displacement calculation from the absorptive effects. The carbide nearest the notch (Fig. 5.4a, circled) moved upward (in the perspective of the image) by 3.0 ± 0.8 μm as the crack opened (Fig. 5.4b, circled). At 90 μm from the root of the crack, $\Delta_T$ was approximately 2.5 μm when averaging between the low-frequency oscillations, which agreed statistically with the measured carbide displacement.

Sample CSMX-4 1 failed during testing, preventing scanning electron microscopy (SEM) from cross-checking the opening measurement. CMSX-4 33 was fatigued but did not fail, and it was imaged with SEM (Fig. 5.5). Intensities near the notch and tip were compared before and after cracking by averaging the intensity in a small rectangle wholly within a single dendrite. The standard deviations defined the uncertainty range via standard error propagation. From Eq. 5.6, the transverse displacement component $\Delta_T$ was 6.4 ± 0.5 μm near the notch and 0.2 ± 0.7 μm near the tip while under a tensile stress of 116.4 MPa. According to the SEM micrograph, $\Delta_T$ near the notch was measured as 8.0 ± 0.3 μm, and the tip region shown in the inset ranged from 0.2 to 1.1 ± 0.1 μm, implying a barely opened crack. These results cannot be compared exactly to the calculations from absorption for two reasons. First, the SEM data were acquired with no stress, and thus the opening would be smaller than that determined by absorption under a load. Second, microscopy was performed *ex situ*, and unscrewing the sample from the carrier, despite the extreme care taken, likely torqued the sample and expanded the crack. Still, these two independent calculation methods roughly approximate the order of magnitude of crack opening in single-crystal superalloys.

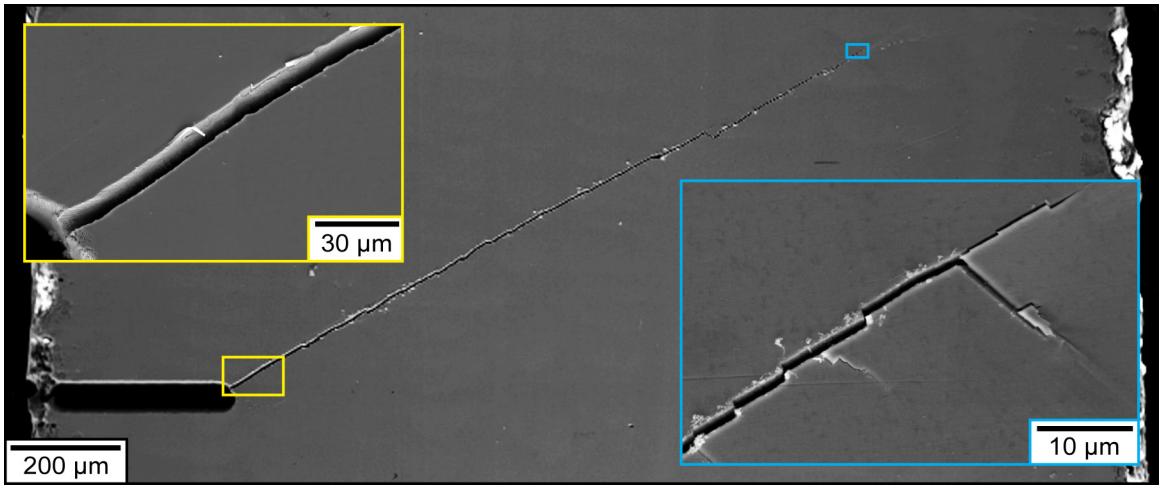


Fig. 5.5. SEM micrograph of CMSX-4 33, a sample similar to that in Fig. 5.4. Insets show close-ups of the crack near the root (yellow box) and tip (cyan box). The openings measured perpendicular to the surface in the plane of the sample, or $\Delta_T$, were 8.0 ± 0.3 µm at the root and 0.2 to 1.1 ± 0.1 µm near the tip. Image courtesy of Dr. L. Liu.

## 5.3 Phase-Contrast Enhancement

Absorption contrast can reveal a crack that has opened enough to cause a measureable change in the optical path length, more than approximately 1 µm in the through-thickness direction in a 200-µm-thick sample, as estimated in Section 3.2.3 and seen in Section 5.2. If the opening is any smaller opening, then the crack and its subtler features are virtually invisible to absorption. Phase contrast adds a much higher level of sensitivity, particularly in defining the edges of the crack, interior fracture surface roughness, and the precise position of the crack tip.

Consider RN4 BM 1, a 200-µm-thick sample of Bridgman-solidified René N4, imaged with two different sample-to-detector distances to compare an absorption image and phase-contrast image of a carbide on the sample surface (Fig. 5.6) and the last several hundred microns of a 1500-µm-long crystallographic fatigue crack (Fig. 5.7). The closest possible distance without endangering the fragile (and expensive) YAG:Ce crystal was 5 mm (Fig. 5.6a, 5.7a). At this distance, the first Fresnel zone (Eq. 3.20) decreased to 0.5 µm, and all visible features were larger than this and thus in the edge-enhancement region. The fringe intensity and spacing decreased below the sensitivity of the detector, however, rendering any phase-contrast effects invisible. The image was

effectively a pure absorption radiograph and analogous to an image from a conventional incoherent x-ray source with a long exposure time and low noise.

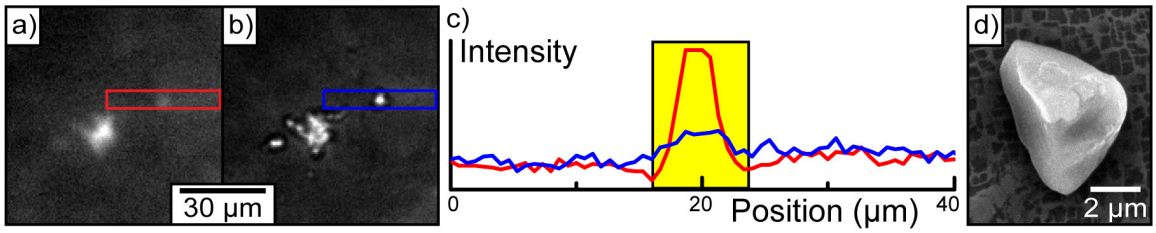


Fig. 5.6. Images of carbide located on the surface with a sample-to-detector distance of (a) 5 mm to minimize phase contrast and (b) 500 mm to enhance it in RN4 BM 1. (c) The intensity profiles of the regions enclosed by rectangles, with yellow shading to indicate the intensity around the carbide. (d) SEM micrograph of the same carbide. The bright globular feature to the left of the carbide was internal and did not appear on the SEM micrograph.

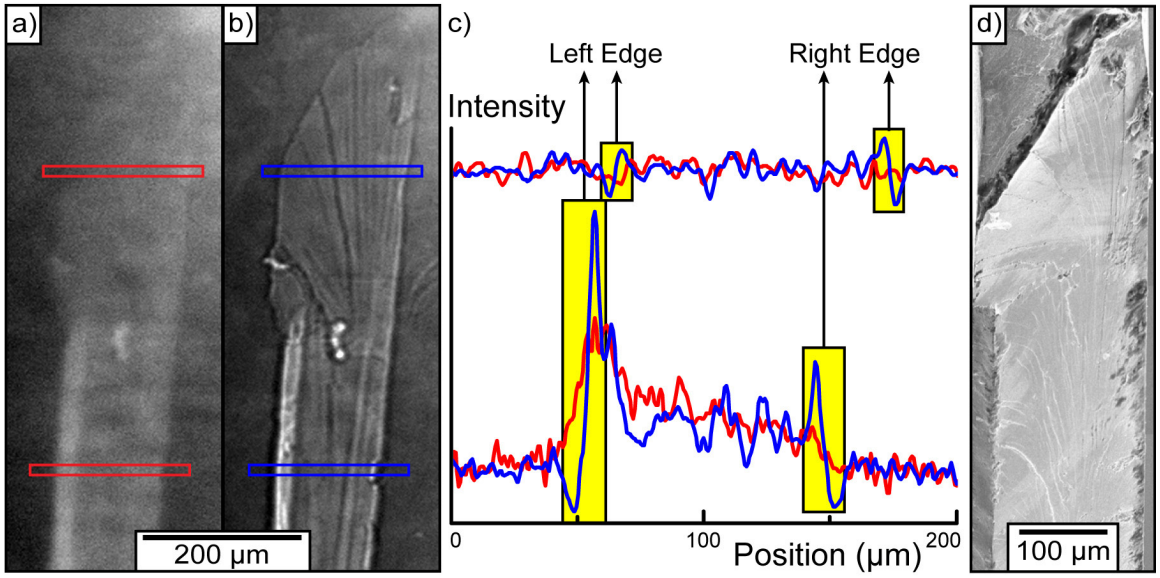


Fig. 5.7. Images of a crack tip with a sample-to-detector distance of (a) 5 mm to minimize phase contrast and (b) 500 mm to enhance it in RN4 BM 1. (c) The intensity profiles of the regions enclosed by the rectangles, with yellow shading to indicate the surface-crack intensities. (d) SEM micrograph of the crack tip.

When the sample-to-detector distance was increased to 500 mm, the first Fresnel zone increased to 5.12 μm, or approximately the width of the carbide. With these sizes roughly equal, the carbide was imaged in the holographic regime and received a substantial contrast enhancement (Fig. 5.6b). Intensity line profiles across the

carbide in both the absorption- and phase-contrast images (Fig. 5.6c) showed a fourfold increase in the intensity, and the full-width at half maximum of the peak was 3.8 ± 0.3 μm. This was similar to the size of 4 to 6 μm measured with a Hitachi S3200N SEM (Fig. 5.6d) [9].

The crack also became much more clearly defined, with previously imperceptible features in the absorption image now manifested (Fig. 5.7b). With the larger sample-to-detector distance, the interference extrema spread out farther apart than the detector's spatial resolution. The expected phase-contrast enhancement appeared for the two surface cracks, which formed sharp electron-density discontinuities between air and superalloy. The intensity was higher at the lower half of the left edge, where two crack planes overlapped. Some roughness along the interior fracture surface also appeared due to phase contrast.

Twin intensity profiles for matching regions in the absorption- and phase-contrast images of the crack are plotted in Fig. 5.7c. In the lower profile, corresponding to the more opened region, both sample-to-detector distances defined the crack, though only phase contrast showed the internal roughness definitively. Pairs of first-order interference maxima and minima were visible at each surface crack, and higher-order oscillations were lost in the background noise. The intensity decreased between the interference maxima of the two surface cracks, because the crack spanned a secondary dendrite arm whose intensities varied due to rhenium and tungsten segregation [10]. The upper line profile near the crack tip of the absorption image was only noise due to the small amount of opening, but the phase-contrast image still showed all features very clearly. Above the blue rectangle in Fig. 5.7c is the crack tip, whose exact position is discernible to within a few microns. Detecting the position of the crack tip so accurately is particularly noteworthy, because phase-contrast imaging is the only method currently available for so doing so internally and non-destructively.

Contrast values, denoted as $C$ (Eq. 3.12), were calculated quantitatively around the left surface crack (LSC) and the right surface crack (RSC) separately for both the absorption- and phase-contrast images (Table 5.2). The through-thickness crack

opening, $\Delta_z$, was then calculated from the absorption contrast by substituting Eq. 5.2 for the uncracked region into $I_{min}$ and Eq. 5.3 for the cracked region into $I_{max}$:

$$C = \frac{I_0 e^{-(T-\Delta_z)/\alpha} - I_0 e^{-T/\alpha}}{I_0 e^{-(T-\Delta_z)/\alpha} + I_0 e^{-T/\alpha}} \quad [5.7]$$

$$C = \frac{e^{-\Delta_z/\alpha} - 1}{e^{-\Delta_z/\alpha} + 1} \quad [5.8]$$

The crack opening was mere microns, and $\alpha$ was larger at approximately 50.6 µm. Expanding the exponential term as a Maclaurin series and simplifying:

$$C = \frac{1 + \Delta_z/\alpha - 1}{1 + \Delta_z/\alpha + 1} = \frac{\Delta_z}{2\alpha + \Delta_z} \quad [5.9]$$

For C expressed as a percentage and $\alpha$ in microns, and again using the fact that $\alpha > \Delta_z$:

$$C(\%) = 100 \cdot \frac{\Delta_z}{101.2 + \Delta_z} \approx \Delta_z \quad [5.10]$$

Through-thickness openings from the phase-contrast contrasts were determined using the simulation results of Section 3.2.3. The model parameters were very similar to this sample and useful for estimation.

Table 5.2. Measured contrasts for the left surface crack (LSC) and right surface crack (RSC) at the top box near the tip and the bottom box toward the root for the RN4 BM 1 sample in Fig. 5.7. Opening predictions were computed for through-thickness displacements and derived using the simulation method of Section 3.2.3. Uncertainties were calculated using standard error propagation.

| | **Absorption Contrast (%)** | | **Phase Contrast (%)** | |
|---|---|---|---|---|
| | **LSC** | **RSC** | **LSC** | **RSC** |
| **Top box** | | | | |
| **Contrast (%)** | 0.121 ± 1.582 | 0.164 ± 1.623 | 4.52 ± 1.19 | 5.54 ± 1.05 |
| **Opening (µm)** | 0.122 ± 1.605 | 0.166 ± 1.646 | 0.359 ± 0.092 | 0.428 ± 0.081 |
| **Bottom box** | | | | |
| **Contrast (%)** | 3.52 ± 1.41 | 1.93 ± 1.46 | 35.0 ± 1.4 | 25.1 ± 1.8 |
| **Opening (µm)** | 3.56 ± 1.43 | 1.96 ± 1.48 | 2.70 ± 0.11 | 1.93 ± 0.14 |

For the top line profile near the crack tip, the absorption contrast was insignificant and fell below the signal-to-noise ratio. The phase contrast was significant, though, and suggested a modest crack opening of only a few hundred microns. Both absorption and phase contrast were much more significant in the bottom box. At the RSC, both phase contrast and absorption contrast agreed statistically on an opening of nearly 2 μm. On the left side, where the crack grew along two overlapping planes, the predicted opening via absorption contrast was approximately double the opening of the RSC, as would be expected for certain pairs of {111} planes. The phase contrast value at the LSC, however, did not match the absorption contrast exactly, most likely because the junction between the two crystal planes did not match the precise geometry of the simulation.

The sample was later broken in two for SEM fractography (Fig. 5.8), where some fracture-surface features were present and corresponded to the features visible between the surface cracks on the radiographs. Surface cracks can be seen *in situ* with other techniques or even the naked eye, but no conventional technique can currently image the internal fracture surface non-destructively without substantial crack opening. The Stage-I fracture surface was fairly flat with occasional pores, eutectic regions, and carbides. On a smaller length scale were river lines and fracture steps, indicative of both normal and shear stresses during propagation [11-12]. Such features were only a couple microns or smaller, well within the first Fresnel zone and approaching the far-field Fraunhofer limit. The interference fringes broadened beyond the size of the feature itself, producing an image on the detector even though the object sizes were less than the spatial resolution of ~1.5 μm. Several such features were manifested in the intensity profile of Fig. 5.4c as broad ripples between the two surface-crack peaks. Though spreading the intensity is beneficial for imaging objects smaller than the spatial resolution, multiple river lines within a few microns could not be individually resolved, as their phase-contrast fringes became a complicated superposition of multiple interference effects.

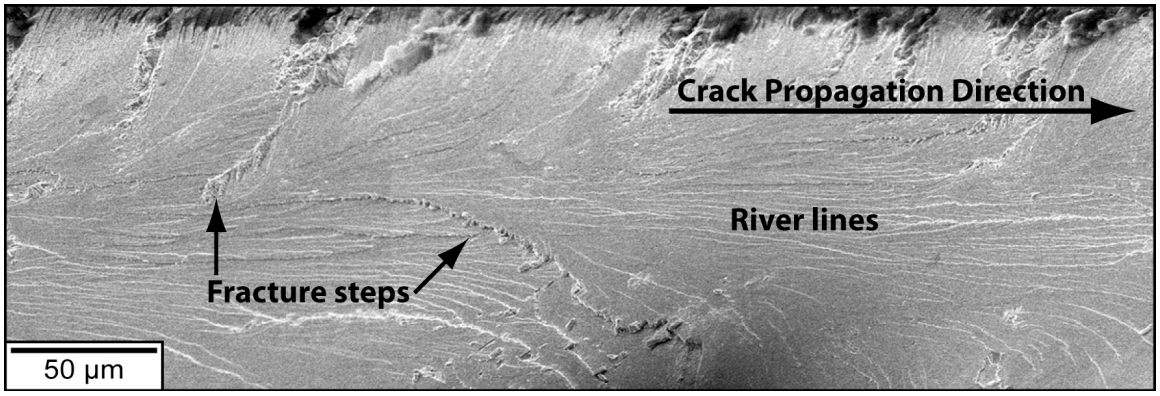


Fig. 5.8. SEM image of the fracture surface in RN4 BM 1, showing river lines and fracture steps.

The large field of view and high image/cycle ratio revealed dynamic events far from the crack tip. Some cracks, particularly in Bridgman-cooled René N5 samples, showed evidence of fretting, known to occur in high-cycle fatigue [13]. Tangential motion from shear stresses between two contact surfaces causes abrasion at asperities, such as the fracture steps in Fig. 5.8, that can eventually lead to material removal or other fatigue damage [14]. Newly exposed metal oxidizes and may be expelled from the crack and then settle on or fall off the surface of the sample (Fig. 5.9); these expulsed particles were identified as tungsten or tantalum oxides with energy dispersive x-ray spectroscopy. Fretting occurred several hundred microns away from the crack tip, even though the opening was microns in magnitude. The sample was always under tension along the [001] direction, so for any tangential motion to cause fretting, multiple axial components of stress must have driven crack propagation and the fracture surface must have had some roughness.

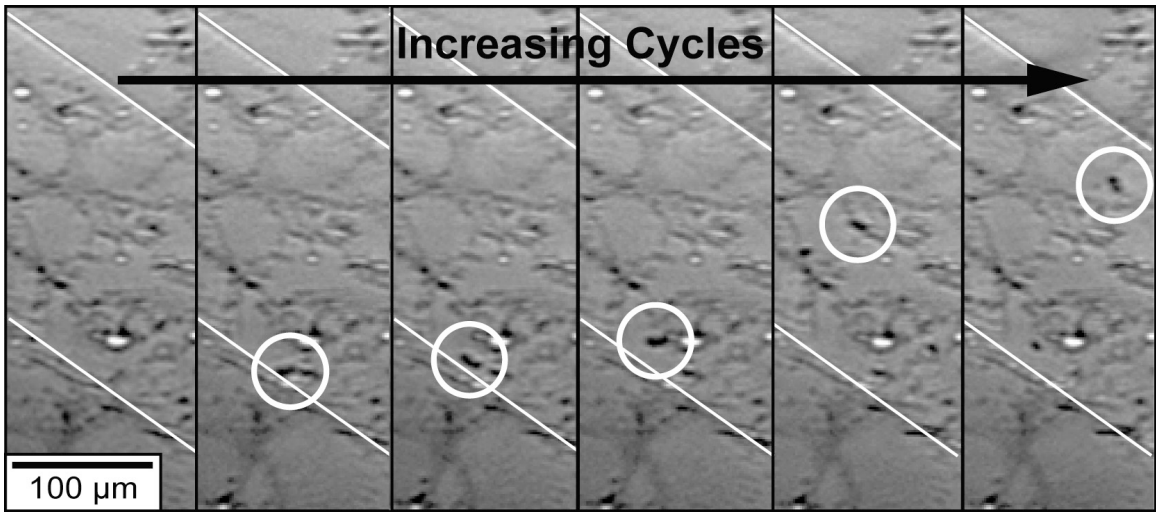


Fig. 5.9. Metal-oxide expulsion from fretting in RN5 BM 1. The oxides are circled, and the surface cracks are traced with a white line. Images are in 2,000-cycle increments.

## 5.4 Mixed-Mode Crack Growth

As shown in the previous two sections, crack opening in monocrystalline nickel-base superalloys was insufficient to cause a substantial change in the optical path length for absorption contrast, particularly near the crack tip. The crystallographic crack morphology suggested more complicated fracture mechanisms than simple tearing along the loading axis, and fretting and fracture steps provided evidence of shearing between fracture surfaces. Though $K_I$ alone was used for initiation-threshold estimates for the testing protocol, it was evidently insufficient to explain completely the observed behavior. For a thorough understanding of crystallographic fatigue-crack propagation, the other two SIF components must be considered.

Previous studies showed that plastic deformation in face-centered-cubic (FCC) crystals localized along one or more of the twelve primary octahedral {111}<110> slip planes, eventually developing into crystallographic Stage-I fatigue cracks [2-3,7-8]. These planes were inclined with respect to the uniaxial loading direction, subjecting the crack tip to more than a single stress component. Multiple stress directions led to a combination of all three fracture modes (Fig. 5.3), preventing the crack from opening significantly as it was kinked and twisted. Irreversible cyclic deformation by both shear and normal stresses advanced the crack, and careful consideration of the SIFs along

each axis was necessary to predict the preferred slip plane for initiation and propagation.

Liu *et al*. performed careful 3D finite element analysis (FEA) with ABAQUS [15] to calculate stress intensities at the crack tip during propagation for all twelve planes in the {111}<110> slip system [6]. Growth mechanisms were different for initiation from a horizontal notch versus propagation from an already-grown, inclined crack, so the two situations were considered separately. The initiation model consisted of a side notch oriented perpendicular to the loading axis. The corresponding crack-propagation model did not include a notch, since the driving mechanisms depended only on the fracture geometry. The crack was inclined in the (100) plane with respect to the horizontal notch by $\beta$, as well as inclined in the (010) plane by γ, also with respect to the notch (Fig. 5.10a).

From nine samples of CMSX-4 (Table 5.1), $\beta \approx 0°$ and $\gamma \approx 0°$ for the notch and $\beta$ = 30° ± 1° and $\gamma$ = 40° ± 4° for the crack, as measured from x-ray images (Fig. 5.10b). Also determined from radiography was the misalignment between the [001] axis in the crystal geometry and the loading axis in the specimen geometry, as seen from the orientation of the dendritic cores. Further orientation details were quantified by Laue x-ray backscattering. The elastic stiffness matrix was transformed accordingly from the crystal geometry into the specimen geometry, which is critically important given that the severe anisotropic elastic constants in single-crystal nickel-base superalloys may be three times greater along <111> than along <001> [4]. SIFs were calculated for the three fracture modes and used to calculate the stress tensor, which is defined by all three SIF components and $\theta$, the angle between the slip plane and the fracture surface [16].

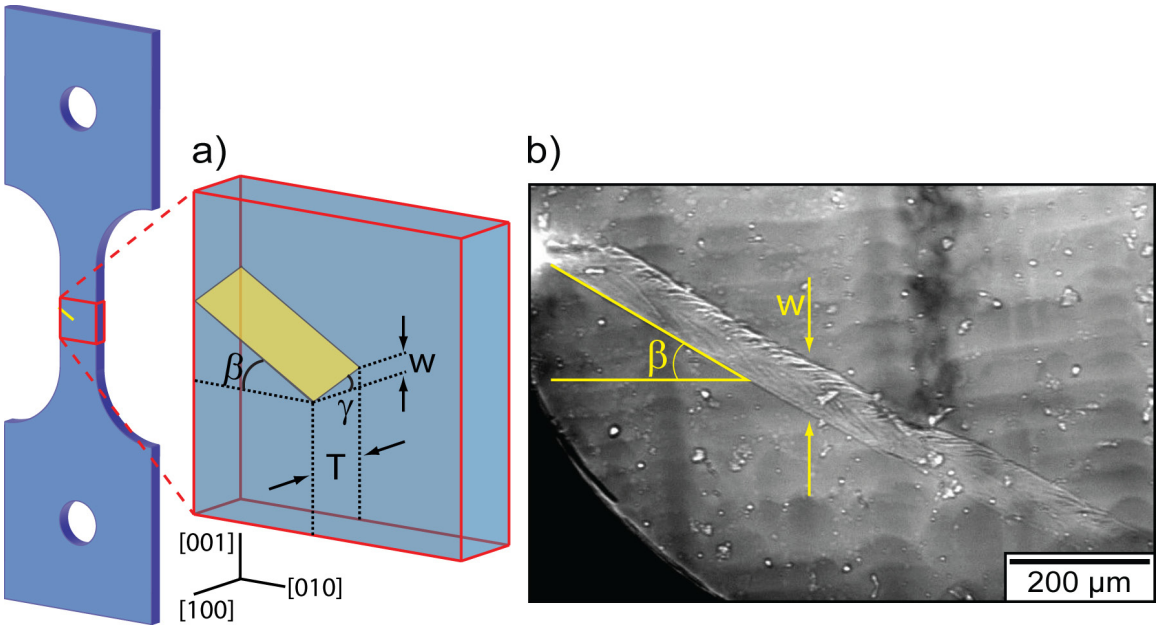


Fig. 5.10. Definition of inclination angles used in the finite element analysis of [6]. (a) Schematic showing *w* and *T* as the crack projections onto the (100) and (001) planes, respectively. (b) The radiograph of CMSX-4 10 shows how to measure $\beta$ and *w*, and $\gamma$ = arctan(*w*/*T*).

The SIFs determined at the crack tip via FEA define a trio of important parameters for the 12 slip systems: the resolved shear stress intensity coefficient ($K_{RSSIC}$), the resolved normal stress intensity coefficient ($K_{RNSIC}$), and the resolved force intensity coefficient ($K_{RFIC}$) [6]:

$$K_{RSSIC} = \frac{1}{|b_{i'}|}[b_{i'}][a_{i'j}][\sigma(K_I, K_{II}, K_{III}, \theta_s)][a_{ij'}][n_{j'}] \quad [5.7]$$

$$K_{RNSIC} = [n_{i'}][a_{i'j}][\sigma(K_I, K_{II}, K_{III}, \theta_s)][a_{ij'}][n_{j'}] \quad [5.8]$$

$$K_{RFIC} = \sqrt{K_{RSSIC}^2 + K_{RNSIC}^2} \quad [5.9]$$

*b* is the Burgers vector, $\sigma$ is the stress tensor, and *n* is the unit normal vector of the slip plane. [*a*] is the matrix of directional cosine components used to convert from the misoriented crystal coordinate system to the specimen coordinate system, defined by the primed components and unprimed components, respectively. $K_{RNSIC}$ defines the effective stress normal to the slip plane that pulls the two surfaces apart, and $K_{RSSIC}$ quantifies the effective decohesive shear stress along the slip plane. $K_{RNSIC}$ and $K_{RSSIC}$ are akin to $K_I$ and $K_{II}$, respectively, for a mixed-mode crack. When added in quadrature,

these two terms define the overall driving force, $K_{RFIC}$, which identifies the slip system most likely to develop into a propagating crack.

### 5.4.1 Finite Element Analysis of Crack Initiation

The notch was modeled as a one-dimensional edge notch with a horizontal length of 300 µm. $K_{RSSIC}$, $K_{RNSIC}$, and $K_{RFIC}$ were calculated for each of the twelve slip systems (Table 5.3). In all cases, $K_{RNSIC} > K_{RSSIC}$, so the resolved normal stress was greater than the resolved shear stress at the notch tip. Based on the largest value of $K_{RFIC}$, the crack should initiate along the $(11\bar{1})[011]$ system; however, $K_{RFIC}$ for the other eleven possibilities are similar enough that the crack could initiate on any or multiple planes simultaneously. The notch was assumed to be perfectly horizontal and one-dimensional, whereas the actual notches may have had some slight inclination and a measureable vertical thickness. Furthermore, the exact misalignment between crystallographic and specimen axes varied slightly among samples, and even these minute differences from those assumed in the finite element model could lead to propagation on other slip systems.

Table 5.3. Resolved shear/normal stress intensity coefficients ($K_{RSSIC}/K_{RNSIC}$) and resolved force intensity coefficient ($K_{RFIC}$) on the twelve slip systems for a 300-µm horizontal side notch with $\beta$ = 0° and $\gamma$ = 0°. All units are MPa·m$^{1/2}$. Significant $K_{RFIC}$ values are in boldface type. Adapted from [6].

| | **Slip System** | | | | | | | | | | | |
|---|---|---|---|---|---|---|---|---|---|---|---|---|
| | $(\mathbf{111})$ | | | $(\mathbf{11\bar{1}})$ | | | $(\mathbf{1\bar{1}1})$ | | | $(\mathbf{\bar{1}11})$ | | |
| | $[\mathbf{1\bar{1}0}]$ | $[\mathbf{10\bar{1}}]$ | $[\mathbf{01\bar{1}}]$ | $[\mathbf{1\bar{1}0}]$ | $[\mathbf{101}]$ | $[\mathbf{011}]$ | $[\mathbf{110}]$ | $[\mathbf{10\bar{1}}]$ | $[\mathbf{011}]$ | $[\mathbf{110}]$ | $[\mathbf{101}]$ | $[\mathbf{01\bar{1}}]$ |
| $K_{RSSIC}$ | 0.48 | 1.12 | 1.61 | 0.70 | 1.37 | 2.08 | 0.37 | 1.22 | 1.59 | 0.87 | 0.96 | 1.81 |
| $K_{RNSIC}$ | 3.79 | 3.79 | 3.79 | 4.10 | 4.70 | 4.71 | 4.41 | 4.41 | 4.41 | 4.68 | 4.68 | 4.68 |
| $K_{RFIC}$ | **3.82** | **3.95** | **4.11** | **4.76** | **4.90** | **5.14** | **4.43** | **4.58** | **4.69** | **4.77** | **4.78** | **5.03** |

In many cases in CMSX-4, cracks initiated uniquely along one crystallographic plane and propagated on it to the completion of the test (e.g., Fig. 5.1). However, several cases of early-stage growth along multiple planes were also observed (Fig. 5.11).

Though the exact orientations of these planes were not determined, based on their inclination angles, they were all {111} planes.

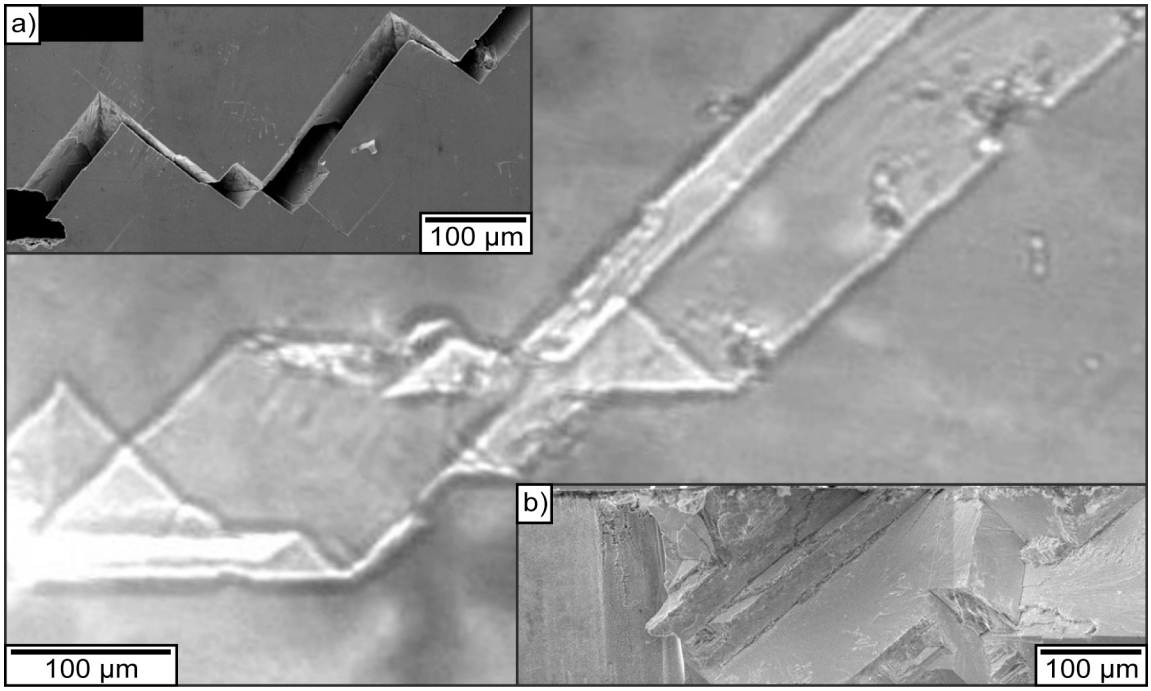


Fig. 5.11. Initiation and early-stage propagation along multiple {111} planes in the sample RN4 BM 1. The notch was located on the left-hand side. (a) SEM image of one surface and (b) the fracture surface near the notch.

### 5.4.2 Finite Element Analysis of Crack Propagation

Consider the tip of a 300-µm crack inclined by $\beta$ = 30° and $\gamma$ = 40°. At this length, the notch effects can be ignored, and the values of $K_{RFIC}$ are different across the slip systems. Because the crack showed no strong preference for a particular fracture plane at the initiation stage, its crystallographic orientation was assigned each of the four possible {111} planes, and the various resolved stress intensity coefficients were determined via FEA (Table 5.4) [6].

FEA results showed that 300-µm-long cracks grown on the $(1\bar{1}1)$ slip planes were subject to the highest $K_{RFIC}$ along that very same plane, with a slight bias toward the $[110]$ direction. Even as the crack lengthened, $K_{RFIC}$ remained highest for the $(1\bar{1}1)[110]$ direction [6]. Cracks grown on the $(1\bar{1}1)$ slip plane, therefore, tended to

grow to completion on the same plane. Cracks initiated on $(\bar{1}11)$ or $(11\bar{1})$ planes also had very large $K_{RFIC}$ components along the $(1\bar{1}1)$ slip plane and tended to change planes during growth. These findings were confirmed experimentally, where nine of the eleven cracks either initiated and grew on the $(1\bar{1}1)$ plane (e.g., Figs. 5.12a-d, 5.12f) or changed to the $(1\bar{1}1)$ plane after growth (e.g., Fig. 5.12e), as determined from the radiographs using $\beta$ and $\gamma$ and the misalignment between the crystal and specimen loading axes. This trend toward crystallographic {111} cracks at room temperature persisted in the other two types of single-crystal nickel-base superalloys tested, René N4 and René N5, regardless of the solidification method.

Table 5.4. Resolved shear/normal stress intensity coefficients ($K_{RSSIC}$/$K_{RNSIC}$) and resolved force intensity coefficient ($K_{RFIC}$) on the twelve slip systems. The initial crack is 300-μm long and located on the plane defined in the left column. All units are MPa·m$^{1/2}$. Significant $K_{RFIC}$ values are in boldface type. Adapted from [6]

| | | **Slip System** | | | | | | | | | | | |
|---|---|---|---|---|---|---|---|---|---|---|---|---|---|
| **Crack on** | | $(\mathbf{111})$ | | | $(\mathbf{11\bar{1}})$ | | | $(\mathbf{1\bar{1}1})$ | | | $(\mathbf{\bar{1}11})$ | | |
| | | $[\mathbf{1\bar{1}0}]$ | $[\mathbf{10\bar{1}}]$ | $[\mathbf{01\bar{1}}]$ | $[\mathbf{1\bar{1}0}]$ | $[\mathbf{101}]$ | $[\mathbf{011}]$ | $[\mathbf{110}]$ | $[\mathbf{10\bar{1}}]$ | $[\mathbf{011}]$ | $[\mathbf{110}]$ | $[\mathbf{101}]$ | $[\mathbf{01\bar{1}}]$ |
| $(\mathbf{11\bar{1}})$ | $K_{RSSIC}$ | 1.49 | 1.06 | 2.11 | 0.41 | 0.52 | 0.94 | 1.19 | 0.40 | 1.60 | 0.21 | 0.53 | 0.32 |
| | $K_{RNSIC}$ | 1.37 | 1.37 | 1.37 | 0.74 | 0.74 | 0.74 | 2.83 | 2.83 | 2.83 | 0.96 | 0.96 | 0.96 |
| | $K_{RFIC}$ | 2.03 | 1.74 | 2.52 | 0.85 | 0.91 | 1.19 | **3.07** | **2.85** | **3.24** | 0.98 | 1.10 | 1.01 |
| $(\mathbf{1\bar{1}1})$ | $K_{RSSIC}$ | 1.02 | 1.14 | 2.16 | 0.15 | 1.47 | 1.32 | 0.63 | 0.36 | 0.26 | 0.04 | 0.83 | 0.87 |
| | $K_{RNSIC}$ | 1.95 | 1.95 | 1.95 | 1.12 | 1.12 | 1.12 | 3.93 | 3.93 | 3.92 | 1.91 | 1.91 | 1.91 |
| | $K_{RFIC}$ | 2.20 | 2.26 | 2.91 | 1.13 | 1.85 | 1.73 | **3.98** | **3.95** | **3.94** | 1.91 | 2.10 | 2.10 |
| $(\mathbf{\bar{1}11})$ | $K_{RSSIC}$ | 0.81 | 0.77 | 1.58 | 0.26 | 0.54 | 0.80 | 1.05 | 0.25 | 1.30 | 0.91 | 0.22 | 1.13 |
| | $K_{RNSIC}$ | 0.89 | 0.89 | 0.89 | 1.13 | 1.13 | 1.13 | 1.99 | 1.99 | 1.99 | 0.72 | 0.72 | 0.72 |
| | $K_{RFIC}$ | 1.20 | 1.18 | 1.82 | 1.16 | 1.26 | 1.39 | **2.25** | **2.00** | **2.37** | 1.16 | 0.75 | 1.34 |
| $(\mathbf{111})$ | $K_{RSSIC}$ | 0.04 | 0.46 | 0.50 | 0.01 | 1.30 | 1.31 | 1.00 | 0.19 | 1.19 | 0.13 | 0.06 | 0.19 |
| | $K_{RNSIC}$ | 4.71 | 4.71 | 4.71 | 0.01 | 0.01 | 0.01 | 3.45 | 3.45 | 3.45 | 1.61 | 1.61 | 1.61 |
| | $K_{RFIC}$ | **4.71** | **4.74** | **4.74** | 0.01 | 1.30 | 1.31 | **3.59** | **3.45** | **3.65** | 1.61 | 1.61 | 1.62 |

Interestingly, for all preferred growth systems, $K_{RNSIC}$ was much larger than $K_{RSSIC}$, so stresses tended toward the opening mode over the shearing mode. This explains the opening observed via absorption contrast. The non-zero shear component justifies the

small amount of opening as compared to a pure Mode-I crack, as well as the fretting-induced metal-oxide expulsion (Fig. 5.9). Crack initiation thresholds based on $K_I$ (Eq. 5.1) provide reasonable approximations without considering any shear effects.

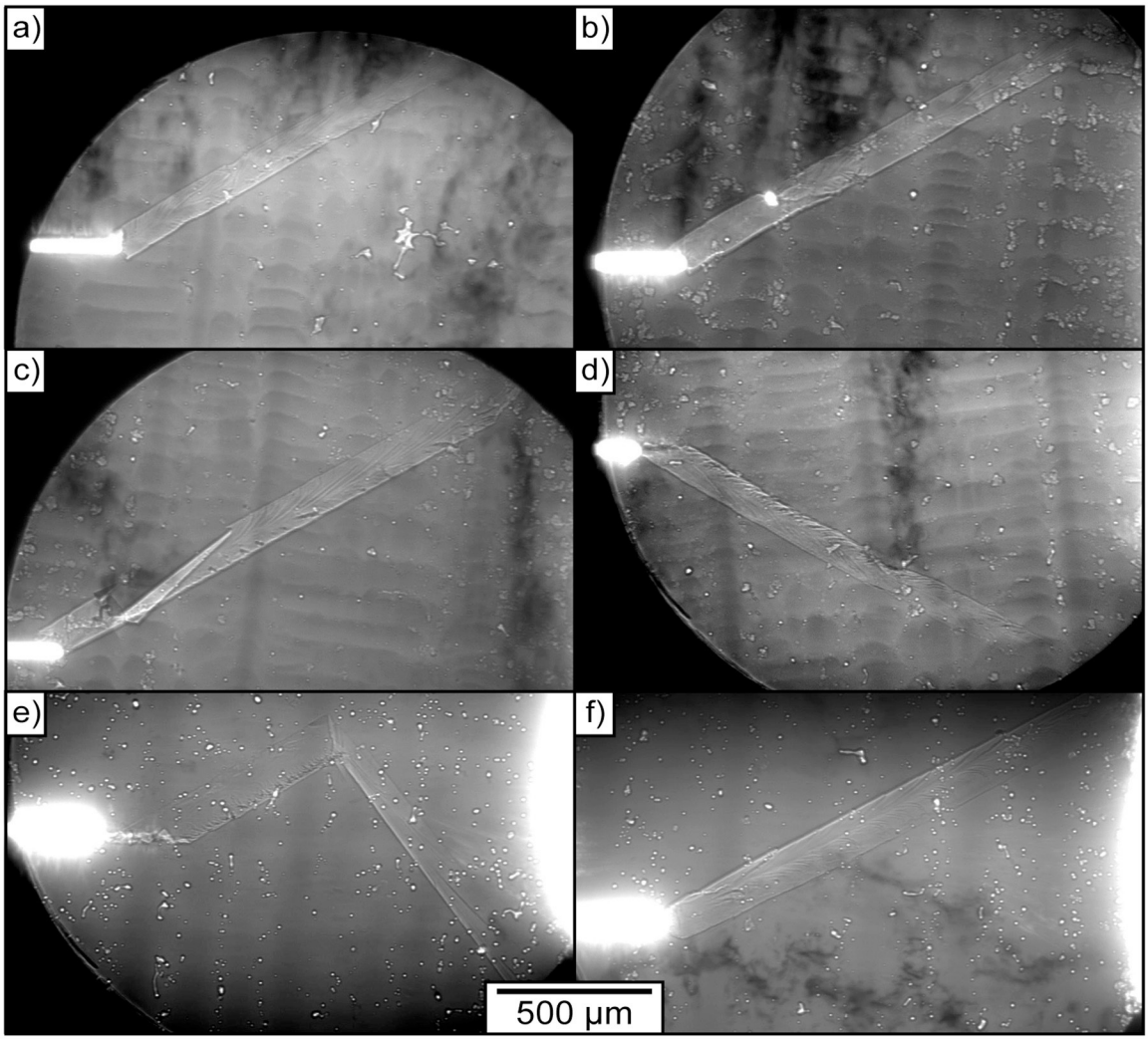


Fig. 5.12. Radiographs of six of the twelve CMSX-4 samples listed in Table 5.1. (a) – (f) correspond to samples CMSX-4 3, 8, 9, 10, 34, and 35, respectively. Note that the contrast levels differ between images.

The exceptions to the $(1\bar{1}1)$ trend were for crack propagation along another plane in the {111} set: the $(111)$ plane (e.g., Fig. 5.1). Cracks grown on this plane, unlike on the other three, had the highest $K_{RFIC}$ values along the $(111)$ plane and not the $(1\bar{1}1)$ plane, although these values were similar in magnitude. Though the sample size was

small, only two out of eleven samples exhibited this behavior. Based on the FEA of the notch (Table 5.3), initiation along the $(111)$ slip plane was the least likely of the four possibilities, so even if the crack could continue propagating on the $(111)$ plane, it might never initiate on it. Furthermore, $K_{RSSIC}$ was much higher for the $(1\bar{1}1)$ plane than the $(111)$ plane. Only $K_{RFIC}$ was considered significant for the propagating and initiating slip systems, but the shear stress component may also be important, particularly in the early Stage-I growth regime [6,8].

## 5.5 Discussion

Fatigue-crack studies are generally postmortem, with analyses performed *ex situ* with some type of optical or electron microscopy. Real-time optical imaging is *in* situ but limited to the surface of a sample if the crack does not open widely, and resistance measurements can measure crack length *in* situ but cannot see microstructure [17]. Other techniques may have 3D capabilities, such as digital-image correlation, but they focus on a particular aspect of fatigue, in this case strain fields. These techniques have significantly advanced the understanding of fatigue-crack propagation, but no technique can interrogate the range of length scales possible with x-ray imaging. Though PCI lacks the spatial resolution of SEM, the strain sensitivity of proper x-ray diffraction, or the exposure length of optical microscopy, it compensates by imaging many details simultaneously to examine their interactions with one another. No other technique can do this *in situ*, especially with cracks opened by mere microns or less.

All samples presented here were microfoils carefully polished to a mirror finish with thicknesses near 200 µm, mainly to limit the number of dendrites projected onto the imaging plane and also to avoid overly attenuating the x-ray beam. The smooth surface finish is important for fatigue studies but, from an imaging perspective, is not necessary to visualize a crack clearly. Heat-treated CMSX-4 samples sanded with 100- and 800-grit sandpaper and imaged (Fig. 5.13) showed vertical scratches, of course enhanced by phase contrast, but the crack was still clearly visible despite the surface roughness. The exteriors of operational components will be roughened from use and

other events, such as particulate ingestion [13], so a robust *in situ* field-diagnostic technique should impose as few restrictions on the sample exterior as possible.

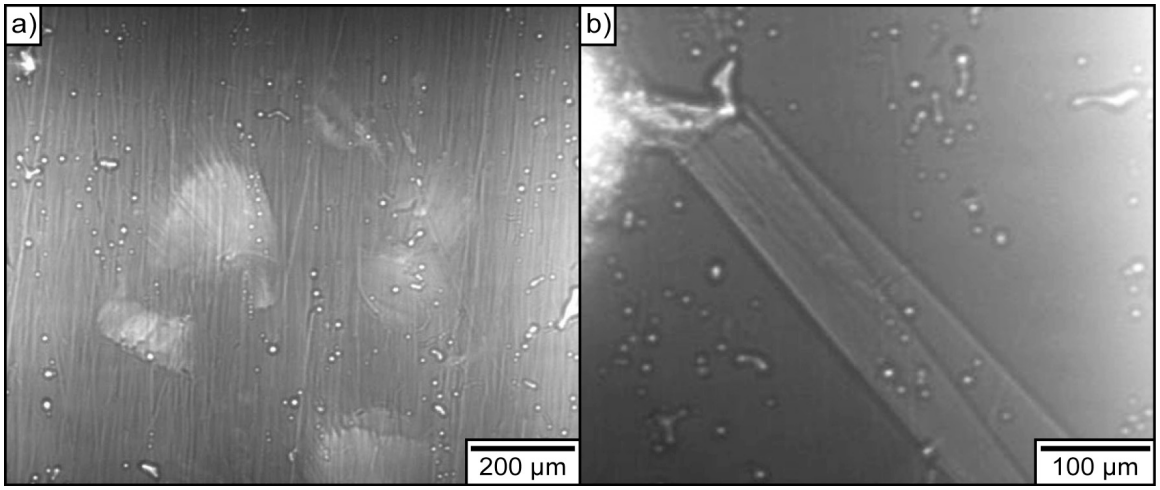


Fig. 5.13. Radiographs of heat-treated CMSX-4 smoothed with sandpaper. (a) Uncracked sample polished with 100-grit sandpaper in the vertical direction and then dented with a screwdriver; (b) cracked sample polished with 800-grit sandpaper.

Surface features aside, a significant impediment to crack detection in service components with x rays is the thickness limitation. Cracks in larger samples are detectable at 23 keV, with images successfully captured through 800 µm of CMSX-4. Photon energy off the fifth harmonic of the undulator (40 keV) at Sector 32-ID-C would penetrate approximately 5 times more material – up to 4 mm – but thicker microfoil specimens may affect the resonance conditions in the central rod of the ultrasonic fatigue apparatus during testing. Higher-energy beamlines exist for thicker and denser materials studies, and since phase contrast is used primarily for edge-enhancement with cracks and not holography, the smaller first Fresnel zone with higher energy is immaterial.

Thicker superalloy samples would be best fabricated as cylinders and mounted directly in place of the Ti-6Al-4V carrier to avoid any resonance issues from piggybacking a thick dogbone-shaped sample on a carrier. With axial symmetry, 3D tomography is possible and has proven very useful in materials analysis in low-cycle fatigue of light

elements [18-19]. In the current setup, the ~1:10 aspect ratio of the microfoils is problematic, as is the limited rotational field-of-view imposed by the carrier. The hydraulic cylinders obstruct some rotation angles as well, although they could be redesigned to be thinner and comprised of an x-ray transparent material. Alternatively, in lieu of a full 360° rotation, the beam can be split in two, and the sample imaged from different vantage points for a stereoscopic pair of images [20]. While not true tomography, 3D information on plane orientation and accurate fracture surface mapping is possible *in situ* [21]. For basic 3D visualization in this work, samples were removed from testing, mounted to a pin on a rotation stage, and rotated over about 120°; clearly, this is not *in situ*, and either tomography or stereoscopy would be useful alternatives.

For thicker materials impenetrable by x rays, neutrons have a much higher penetration depth often measured in centimeters, depending on their temperature. Phase-contrast neutron radiography is possible at coherent spallation sources or with collimated, cropped neutron beams, although the integration times required may be prohibitively long (tens of minutes to hours) and the spatial resolution too low (50 to 100 μm) [22-23]. With improvements in neutron detection, these limitations should improve significantly. Gamma rays have even greater penetration depths than x rays or neutrons, and laser-generated gamma rays, which have a brilliance greater than $10^{23}$ photons/s/0.1% bandwidth/mrad$^2$/mm$^2$, have recently been tested for PCI [24]. X rays are currently still the electromagnetic wave of choice for practical real-time imaging, due to the comparatively wide-spread availability of synchrotron x-ray sources with high spatial resolutions and short integration times.

## 5.6 References


1 Brundidge, C. L., Miller, J. D. & Pollock, T. M. Development of Dendritic Structure in the Liquid-Metal-Cooled, Directional-Solidification Process. *Metall Mater Trans A* **42**, (2011).

2 Liu, L. *et al.* In situ imaging of high cycle fatigue crack growth in single crystal nickel-base superalloys by synchrotron X-radiation. *J Eng Mater Technol* **130**, (2008).

3 Chan, K. S., Feiger, J., Lee, Y. D., John, R. & Hudak, S. J. Fatigue crack growth thresholds of deflected mixed-mode cracks in PWA1484. *J Eng Mater Technol* **127**, (2005).
4 Hermann, W., Sockel, H. G., Han, J. & Bertram, A. Elastic properties and determination of elastic constants of nickel-base superalloys by a free-free beam technique. *Superalloys 1996*, (1996).
5 Lukas, P. & Kunz, L. Specific features of high-cycle and ultra-high-cycle fatigue. *Fatigue Fract Eng Mater Struct* **25**, (2002).
6 Liu, L. *et al.* In situ synchrotron x-ray imaging of high-cycle fatigue crack propagation in single-crystal nickel-base alloys. *Acta Mater* **59**, (2011).
7 Yi, J. Z., Torbet, C. J., Feng, Q., Pollock, T. M. & Jones, J. W. Ultrasonic fatigue of a single crystal Ni-base superalloy at 1000 °C. *Mater Sci Eng A* **443**, (2007).
8 Gell, M. & Leverant, G. R. The characteristics of stage I fatigue fracture in a highstrength nickel alloy. *Acta Metall* **16**, (1968).
9 Hitachi High Technologies America, Inc., Pleasanton, CA.
10 Husseini, N. S. *et al.* Mapping single-crystal dendritic microstructure and defects in nickel-base superalloys with synchrotron radiation. *Acta Mater* **56**, (2008).
11 Hull, D. The Effect of Mixed-Mode I/III on Crack Evolution in Brittle Solids. *Int J Fracture* **70**, (1995).
12 Duquette, D. J., Gell, M. & Piteo, J. W. A Fractographic Study of Stage-1 Fatigue Cracking in a Nickel-Base Superalloy Single Crystal. *Metall Trans* **1**, (1970).
13 Nicholas, T. *High Cycle Fatigue: A Mechanics of Materials Perspective*. (Elsevier, 2006).
14 Suresh, S. *Fatigue of Materials*. 1st edn, (Cambridge University Press, 1991).
15 ABAQUS, Dassault Systèmes, Waltham, MA.
16 Anderson, T. L. *Fracture mechanics: fundamentals and applications*. 2nd edn, (CRC Press, 1995).
17 Spitas, V., Spitas, C. & Michelis, P. Real-time measurement of shear fatigue crack propagation at high-temperature using the potential drop technique. *Measurement* **41**, (2008).
18 Stock, S. R. Recent advances in X-ray microtomography applied to materials. *Int Mater Rev* **53**, (2008).
19 Herbig, M. *et al.* 3-D growth of a short fatigue crack within a polycrystalline microstructure studied using combined diffraction and phase-contrast X-ray tomography. *Acta Mater* **59**, (2011).
20 Zhou, S.-A. & Brahme, A. Development of phase-contrast X-ray imaging techniques and potential medical applications. *Physica Medica* **24**, (2008).
21 Ignatiev, K. I., Lee, W. K., Fezzaa, K. & Stock, S. R. Phase contrast stereometry: fatigue crack mapping in three dimensions. *Philos Mag* **85**, (2005).
22 Allman, B. E. *et al.* Imaging - Phase radiography with neutrons. *Nature* **408**, (2000).
23 Kardjilov, N., Lehmann, E., Steichele, E. & Vontobel, P. Phase-contrast radiography with a polychromatic neutron beam. *Nucl Instrum Meth A* **527**, (2004).

24 Cipiccia, S. *et al.* Gamma-rays from harmonically resonant betatron oscillations in a plasma wake. *Nat Phys* **7**, (2011).

# CHAPTER 6
# IMAGING INITIATION AND PROPAGATION

The previous chapter demonstrated that phase-contrast x-ray radiography could successfully image fatigue cracks, ameliorating the limitations of poor absorption contrast. This chapter will extend those results to studies at elevated temperatures, measurements of growth rates and the effect of microstructure, and finally the role of diffraction in predicting crack initiation and propagation.

## 6.1 High-Temperature Effects

All samples in Chapter 5 were examined at room temperature. The cracks grew mostly crystallographically along {111} planes; however, cracks in face-centered-cubic crystals do not always grow along {111} planes. Cyclic frequency, environment, and temperature may all have an effect on the crack morphology and, consequently, the fatigue life [1]. One of the primary applications of nickel-base superalloys is in the hot sections of turbines, where they are subjected to extreme temperatures in demanding environments. The exposed sections are frequently surrounded by a thin (hundreds of microns) ceramic thermal barrier coating (TBC), such as yttria-stabilized zirconia (YSZ). TBCs insulate the underlying superalloy from extreme heat and reduce oxidation damage and thermal fatigue [2]; nevertheless, temperatures may still reach up to 90% of the melting point and alter the fatigue-crack behavior from that predicted with finite element analysis (FEA) at room temperature.

The open, unobstructed environment of phase-contrast imaging (PCI) allowed a microtorch or furnace to heat the sample, further simulating operating conditions while simultaneously acquiring *in situ*, real-time information. Superalloy samples without TBCs were tested in the same manner as at room temperature, except they were heated

using either compressed air expelled from an alumina heater or an oxyhydrogen microtorch aligned parallel to the sample surface. The temperature at the gauge section of the specimen, ranging from 538°C to 720°C, was monitored with an infrared pyrometer. The relevant experimental details are listed in Table 6.1. Though not observed in this subset of tested samples, the initiation threshold, $\Delta K_{th}$, and hence the required stress amplitude required for crack initiation and propagation, $\Delta\sigma$, generally increased with temperature due to increasing ductility, as was previously demonstrated in René N5 [3]. The ultrasonic fatigue apparatus operated at a large enough displacement amplitude for initiation at temperatures up to approximately 750°C, but the crack character transitioned from crystallographic to non-crystallographic within the testable temperature range.

Table 6.1. Nickel-base superalloy samples studied at various temperatures. The CMSX-4 samples were heat-treated, smoothing their microstructure. LMC = liquid-metal-cooling. NC = non-crystallographic, horizontal crack propagation. Δσ = stress amplitude necessary for crack initiation and propagation. Cracks that grew along {111} planes but showed roughened surface cracks were denoted as "rough {111}".

| Superalloy and sample number | Temperature (°C) | Δσ (MPa) | Fracture plane |
|---|---|---|---|
| CMSX-4 35 | 23 | 121.2 | {111} |
| CMSX-4 36 | 550 | 71.8 | rough {111} |
| CMSX-4 37 | 600 | 45.6 | NC |
| René N5 LMC 1 | 23 | 35.2 | {111} |
| René N5 LMC 2 | 538 | 135.4 | rough {111} |
| René N5 LMC 3 | 720 | 113.0 | NC |
| René N5 LMC 4 | 580 | 53.8 | NC |
| René N5 LMC 5 | 720<br>RT | 75.2 | NC<br>{111} |

Cracks grown at 538°C (Figs. 6.1c, 6.1d) remained crystallographic along {111} planes, showing crystallographic crack propagation, but the fracture surface and surface cracks appeared rougher than those observed in room-temperature samples (Figs. 6.1a, 6.1b). For the heat-treated CMSX-4 sample lacking a well-defined separation between dendritic and interdendritic regions (Fig. 6.1c), no particular correlation of roughness

with the microstructure was observed. In the liquid-metal-cooling (LMC) René N5 sample (Fig. 6.1d), the surface cracks showed sensitivity to the interdendritic regions, with roughness running parallel to the secondary-dendrite arm direction in the [010] direction. Heated sample surfaces showed evidence of oxidation, seen by eye as discoloration along the gauge section, suggesting a possible cause for the rougher crystallographic crack morphology.

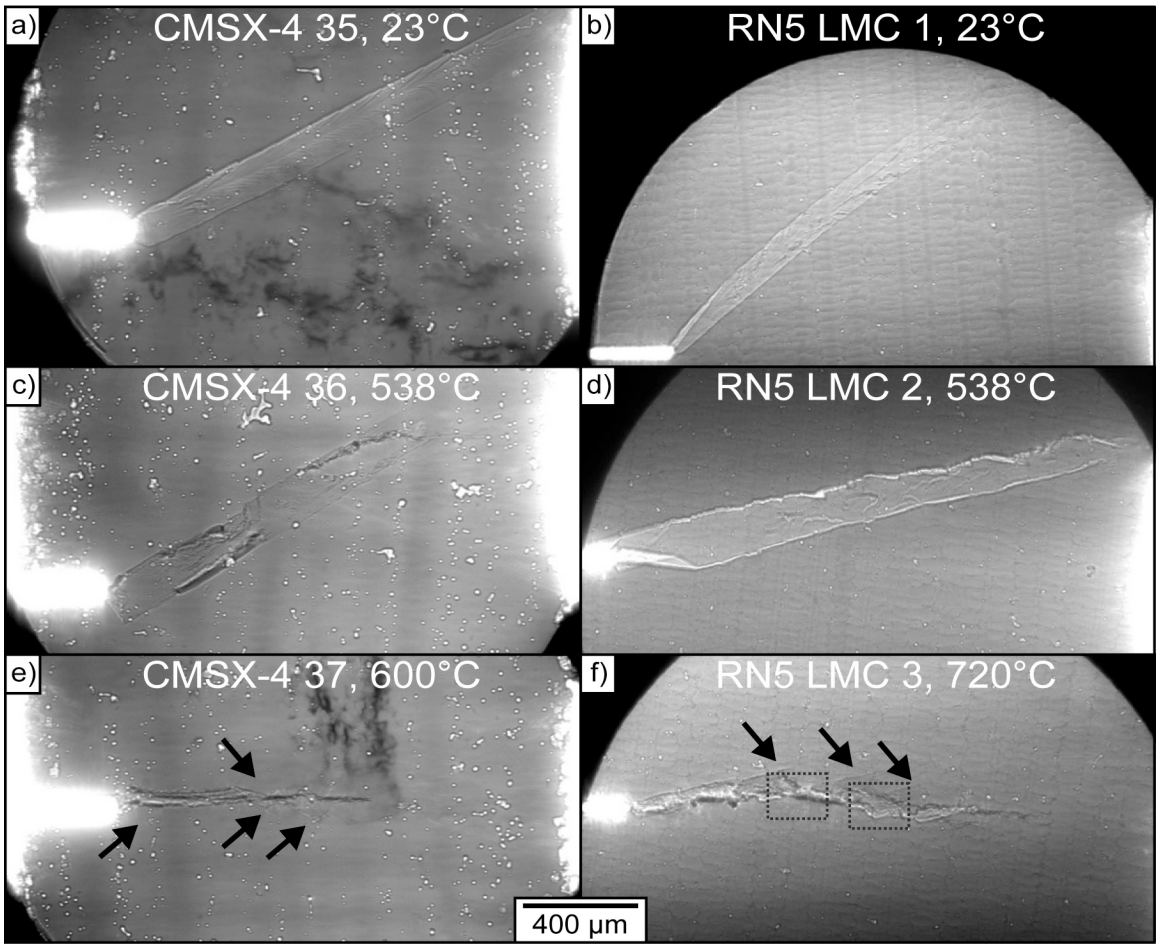


Fig. 6.1. Crack propagation at different temperatures in CMSX-4 (a, c, e) and René N5 (b, d, f). RN5 LMC = René N5 liquid-metal cooled. Arrows in (e) and (f) indicate the locations of persistent slip bands. Boxes around regions of (f) indicate the locations of scanning electron microscopy images in Fig. 6.2.

At even higher temperatures, cracks showed evidence of crystallographic deformation as persistent slip bands (PSBs), extending a few hundred microns along {111} planes. The PSBs were visible on the x-ray radiographs due to a slight change in density associated with dislocation propagation, although they were difficult to see without altering the image contrast significantly. The final propagating crack, though, was no longer crystallographic but instead primarily Mode-I (perpendicular to the loading axis) in morphology (Figs. 6.1e, 6.1f). For sample RN5 LMC 3 (6.1f), the crack grew non-crystallographically with a high degree of tortuosity, and at times it followed the interdendritic regions. This behavior was also seen at temperatures greater than 580°C in Bridgman-solidified René N5 samples, which had a much coarser microstructure. *Ex situ* scanning electron microscopy (SEM) agreed with the results of the x-ray radiographs (Fig. 6.2). These results showed PSB formation along {111} planes where the crack abruptly changed directions to follow the lighter regions corresponding to the interdendritic regions on the micrographs. The dual presence of both crystallographic and non-crystallographic fatigue effects suggested competing failure modes.

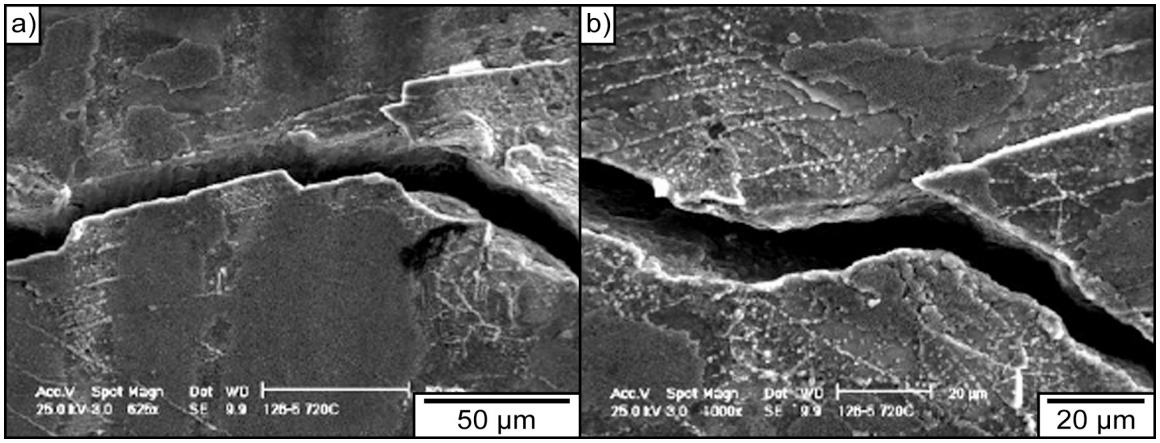


Fig. 6.2. SEM images of the (a) left and (b) right boxed regions shown in Fig. 6.1f. PSBs are visible forming crystallographically away from the crack. The lighter regions (right side of (a) and left side of (b)) are interdendritic regions. Image is courtesy of Dr. C. L. Brundidge, and adapted from [4] with added scale bars.

Crack growth at temperatures between the mixed-mode (538°C) and non-crystallographic crack (720°C) showed strong effects of the two cracking morphologies, both crystallographic and non-crystallographic. The crack in RN5 LMC 4, grown at 580°C (Fig. 6.3a), manifested both morphologies, and their presence had significant effects on the growth rate (Fig. 6.3b). During initiation in Region 1, crystallographic PSBs and a non-crystallographic crack formed simultaneously, and the crack growth rate was very slow. In Region 2, no PSBs were visible, and the crack rate accelerated dramatically, with just a single dominant fracture mode to follow. The growth rate slowed upon entering Region 3, where the crack bifurcated and formed slip bands along two sets of {111} planes. The material ultimately fractured along the lower plane, and the crack rapidly accelerated in Region 4 to failure. In regions with both morphologies (1 and 3), the growth rate was much slower than in regions with just one (2 and 4). Previous studies have shown a competition between Mode-I crack growth and {111} crack growth at lower frequencies in a similar nickel-base superalloy, PWA 1484, at 593°C [5], and the evolution of that dual crack morphology was observed *in situ* here. Again, the type of crack with the largest growth rate dominated and became the propagating crack.

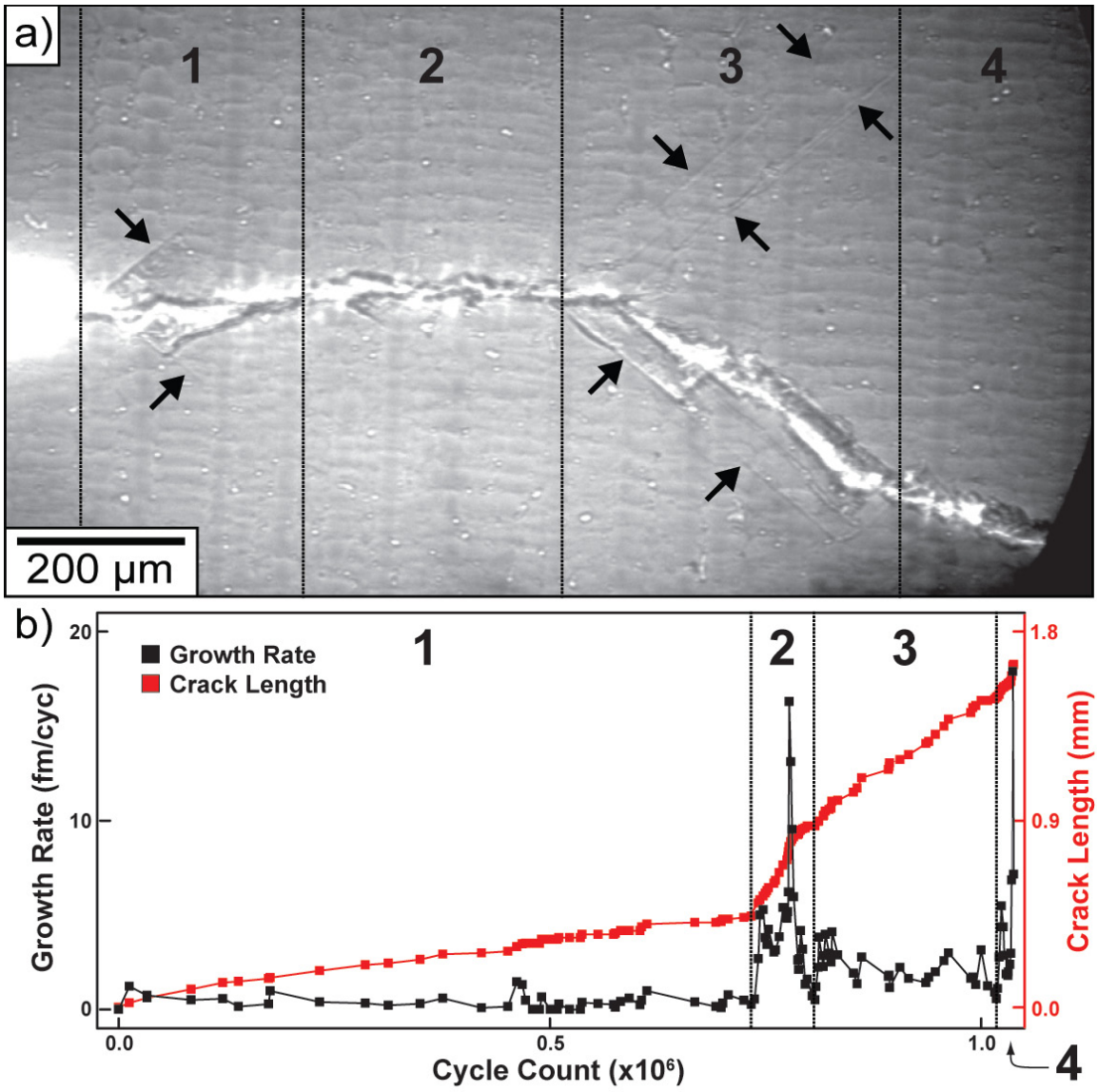


Fig. 6.3. Crack propagation in René N5 LMC 4 at 580°C. (a) The primary crack is non-crystallographic, but several regions show additional plastic deformation along {111} planes. (b) The corresponding crack-growth data show slower growth rates in the regions where both morphologies of cracks grew (regions 1 and 3) than in regions with only one mode (regions 2 and 4).

The morphological transition between crystallographic and non-crystallographic crack was reversible (Fig. 6.4). A crack in RN5 LMC 4 was initiated and grown at 720°C; after ~400 µm of non-crystallographic growth the microtorch was shut off, and the sample was cooled to room temperature. Further cracking was observed along a {111}

plane, although the crack surface appeared rougher than in typical room temperature samples.

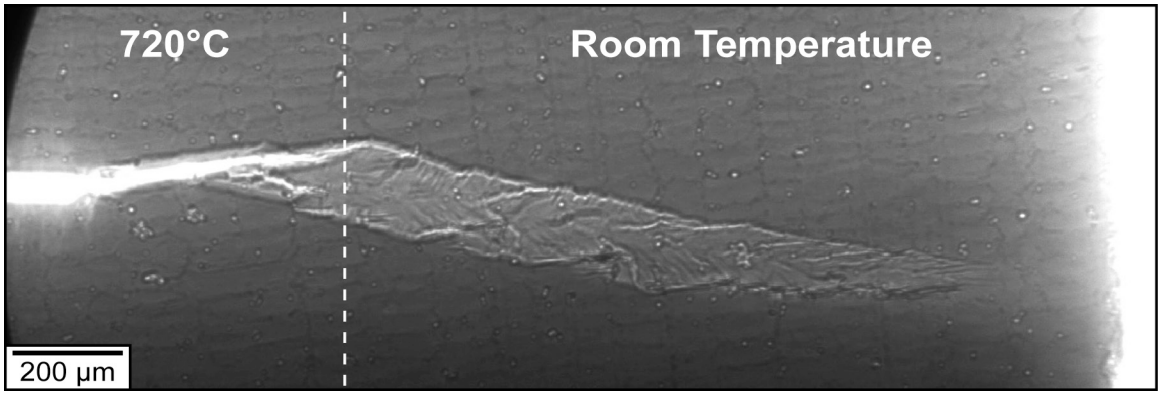


Fig. 6.4. Crack propagation at two temperatures in RN5 LMC 5. Once the torch was shut off (white dotted line) and the temperature cooled, the non-crystallographic crack transitioned into a {111}-oriented crack.

## 6.2 Real-Time Growth Rate Measurements

Measurements of crack growth rates are important for fatigue-lifetime predictions and studies of the interaction between cracks and microstructural features. Accurate measurements require the specific location of the crack tip, which is provided by phase contrast. After initiation and during sub-critical crack growth (Fig. 1.9, Regime B), crack propagation is generally considered insensitive to the microstructure [6], and the growth rates are often modeled with respect to the stress-intensity factor (SIF) range, $\Delta K$, using the Paris Law:

$$\frac{da}{dN} = C(\Delta K)^m \qquad [6.1]$$

$a$ is the crack length, $N$ is the number of cycles, and $C$ and $m$ are material constants [7]. A simple power law relationship is perhaps an oversimplified expression of a complicated process, as opined later by the eponym himself [8]. Moreover, this model may not completely describe crystallographic crack growth in monocrystalline superalloys, where anisotropy and local lattice conditions can affect propagation. Interdendritic regions, where dislocations accumulate between misoriented dendrites, for example, may have a minor effect on the crack growth rate not measureable without

data on the micron scale, particularly at elevated temperatures. X-ray radiography defines the precise location of the crack tip internally while simultaneously imaging the microstructure, enabling measurements of very small growth rates and the corresponding effects of material features (such as inclusions and voids), as well as competitive growth modes, as seen in Fig. 6.3.

Plots of crack length as a function of the number of loading cycles are shown in Fig. 6.5 for several CMSX-4 samples from Table 5.1, of which all but CMSX-4 9 and CMSX-4 10 were pre-cracked before imaging at the synchrotron. The crack length was defined to within a couple microns by the position of a particular surface crack, so that the vertical error bars were the size of the data points (Fig. 6.5a). In general, the crack length was irrespective of which surface crack was used or whether an interior part of the crack tip was measured. They may differ by a small constant, but this did not affect the growth rate, *da*/*dN*.

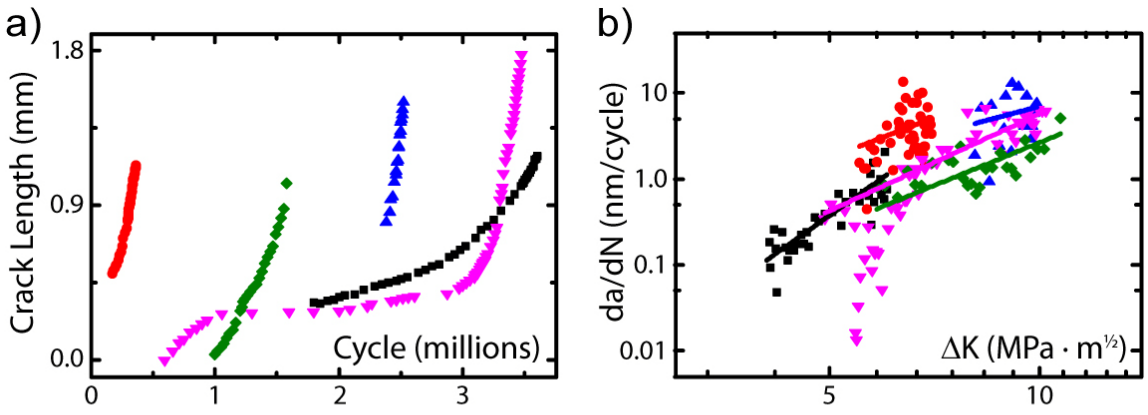


c)

**Paris Law: da/dN = C(ΔK)$^m$**

| Sample | C ± ΔC | m ± Δm |
|---|---|---|
| **CMSX-4 1** | (3.52 ± 6.24) x $10^{-14}$ | 5.76 ± 0.99 |
| **CMSX-4 3** | (1.15 ± 3.52) x $10^{-11}$ | 3.13 ± 1.60 |
| **CMSX-4 8** | (4.95 ± 2.89) x $10^{-11}$ | 2.15 ± 2.60 |
| **CMSX-4 9** | (1.52 ± 0.88) x $10^{-12}$ | 3.75 ± 0.38 |
| **CMSX-4 10** | (1.29 ± 1.80) x $10^{-12}$ | 3.31 ± 0.61 |

Fig. 6.5. Plots of (a) crack length as a function of cycles and (b) growth rate as a function of the SIF with Paris Law fits (Eq. 6.1) on a logarithmic scale. The table below the data shows the Paris Law fitting parameters from (b) and serves as a legend for the colors in (a) and (b).

Crack growth rates were calculated for fitting with the Paris Law and lifetime predictions. $\Delta K$ for an inclined, cracked specimen required a slight modification to Eq. 5.1. Each crack had an in-plane inclination angle, $\beta$, measured on the radiographs as the angle from the horizontal axis to the crack. This angle related the measured crack length to the projected length along the horizontal (001) plane and defined $\Delta K_I$ as

$$\Delta K_I = \Delta\sigma\sqrt{\pi}\sqrt{a_n + a_c\cos(\beta)} \quad [6.2]$$

where $a_n$ and $a_c$ are the notch length and crack length, respectively. Assuming pure Mode-I loading, the growth rates were plotted against the SIFs and fit with the Paris Law of Eq. 6.1 (Fig. 6.5b). Though crack growth is multi-mode in character, the $K_{RFIC}$ (resolved force intensity coefficient) from FEA and $K_I$ were quite similar. The extracted fitting parameters (Fig. 6.5c) had substantial uncertainties due to the significant scatter in the data, despite the very accurate growth rate measurements. Values of $m$ fell within published values for single-crystal nickel-base superalloys [9-10], though the value of $m$ for CMSX-4 1 was higher than that of the other four samples, even when considering the uncertainty range.

The fatigue lifetime can be predicted using the Paris Law fitting parameters in an integral version of Eq. 6.1 [11]:

$$N = \frac{1}{C\left(\Delta\sigma\sqrt{\pi}\right)^m}\int_{a_i}^{a_f} a^{-\frac{m}{2}}da \quad [6.3]$$

$$N = \frac{1}{C\left(\Delta\sigma\sqrt{\pi}\right)^m}\frac{2}{(m-2)}\left(a_i^{1-m/2} - a_c^{1-m/2}\right) \quad [6.4]$$

$a_i$ is the notch plus initial crack length projected onto the horizontal (001) plane, and $a_c$ is the critical crack length at which the material will fracture instantaneously, estimated here as the length of the gauge section (2000 µm). The calculated lifetimes (Eq. 6.4) had an enormous error range, as calculated with standard error propagation, due to the large uncertainties in the fitting parameters $m$ and $C$ (Table 6.2).

Table 6.2. Lifetime calculation (Eq. 6.4) based on the fitting parameters of Fig. 6.5 and data from Table 5.1. Samples 1, 3, and 8 were pre-cracked before imaging, while samples 9 and 10 were initiated and grown while imaging. Uncertainties in the predicted lifetimes are derived from the uncertainties in *m* and *C* using standard error propagation.

| Sample | $\Delta\sigma$ (MPa) | Initial Crack Length (μm) | Predicted Lifetime (cycles x $10^6$) | Predicted Lifetime (cycles x $10^6$) | Measured Lifetime (cycles x $10^6$) |
|---|---|---|---|---|---|
| CMSX-4 1 | 102.8 | 332 | 2.17 | 5.18 | 3.72 |
| CMSX-4 3 | 103.6 | 504 | 0.235 | 1.002 | 0.362 |
| CMSX-4 8 | 142.8 | 801 | 0.136 | 0.761 | 2.70 |
| CMSX-4 9 | 135.4 | 0 | 0.958 | 0.837 | 3.46 |
| CMSX-4 10 | 173.0 | 0 | 1.10 | 1.70 | 1.58 |

The measured fatigue lifetimes fell within the range of predicted lifetimes for three of the five samples (Table 6.2). One of the exceptions, CMSX-4 8, grew suddenly and quickly from a very long preexisting crack, so comparatively few data points were collected, possibly explaining the poor agreement between the measured and predicted lifetimes. For the other exception, CMSX-4 9, the uncertainties in the two fitting parameters were much smaller than in the other cases, and many data points were collected. The plot of crack length as a function of cycles (Fig. 6.5a) showed an initial growth period, but then extraordinarily slow propagation over two million cycles before resuming growth. The near-cessation occurred at a pore on the surface (Fig. 6.6), which not only halted crack propagation but also caused a secondary crack along another plane to initiate and grow slowly. Once the two planes converged into a single plane, the growth rate quickly accelerated until the test was halted (Fig. 6.6, inset). After the sample was fully tested, it was removed from the Ti-6Al-4V carrier, mounted on a rotation stage, and rotated over 105° to see the relationship between the two fracture planes (Fig. 6.7). Both cracks grew along {111} planes, based on the inclination angles with respect to the (100) and (010) planes.

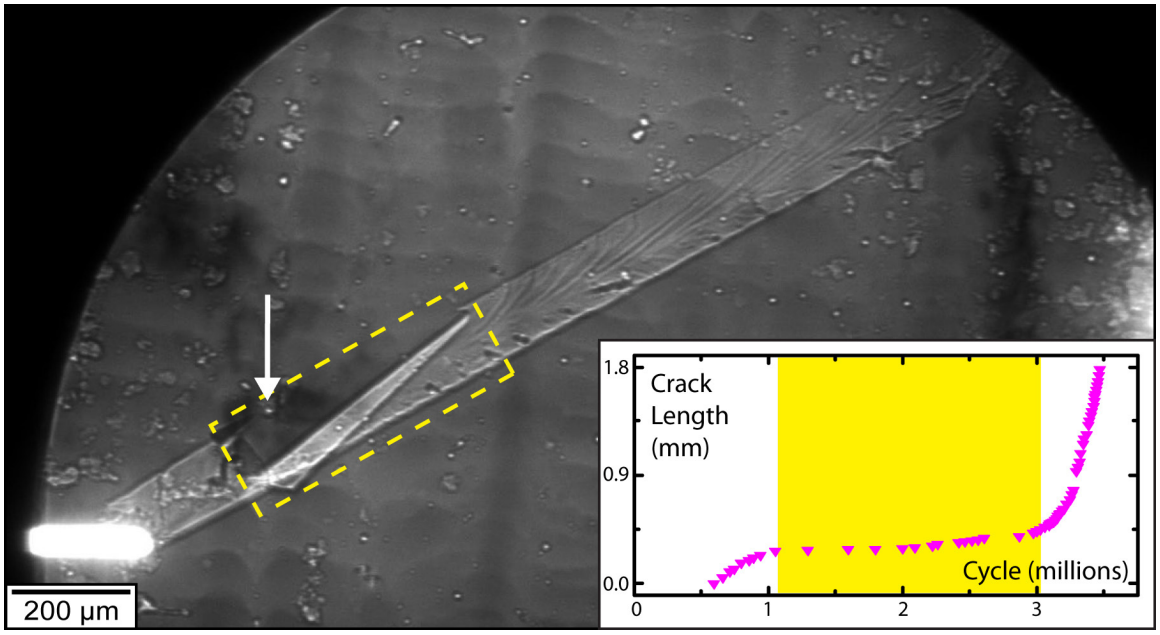


Fig. 6.6. Radiograph of crack propagation in CMSX-4 9. The white arrow shows the pore that arrested the crack for a couple million cycles and deflected the crack to another crystallographic plane. The inset shows a plot of crack length, where the yellow-shaded area corresponds to the region in the radiograph surrounded by the yellow dotted box.

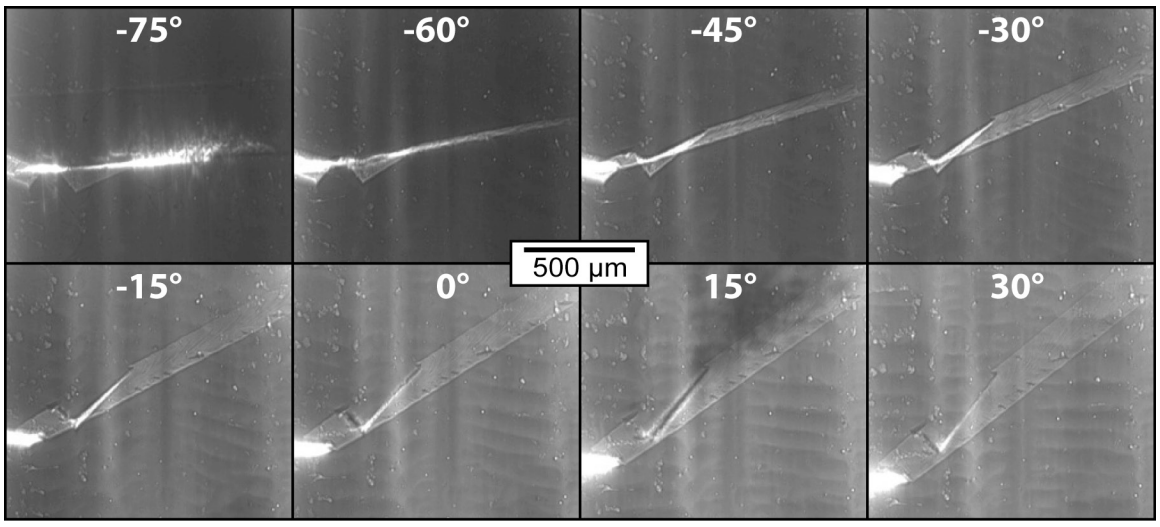


Fig. 6.7. Images of CMSX-4 9 removed from the ultrasonic fatigue apparatus and rotated over 105°. This series of images helps visualize the 3D relationship between the two crack planes without full tomography.

Because radiography can image both 3D microstructural features and crack propagation simultaneously, the two can be correlated very accurately. The dendritic and interdendritic regions had no noticeable effect at the micron scale resolution of these tests at room temperature. Cracks grew through interdendritic regions at the same rate as in the dendritic regions, and the crack morphology was equally unaffected, as expected in the intermediate growth regime (Fig. 1.9, regime B). Furthermore, crack propagation was generally unaffected by pores and carbides, with CMSX-4 9 being a notable exception. Though such features may or may not arrest a crack, they are certainly important in initiating them.

## 6.3 Imaging and Predicting Crack Initiation and Propagation

Fatigue lifetimes are based on a number of factors, including loading frequency, loading history, specimen temperature, and environmental factors [12]. The variability in microstructural details, such as pores and grain boundaries, can complicate prognostication in VCHF, where lifetimes are initiation-dominated and highly susceptible to the microstructural extremes that frequently occur internally [13]. PCI can identify potentially fatal features and see the early-stage initiation behavior, as well as provide clues to the crack's future path with diffraction contrast. This knowledge is useful for both improving materials design and damage diagnostics of operational components.

### 6.3.1 Prescient Plastic Zone

A plastic zone forms ahead of a crack tip as it propagates in a ductile material, such as a nickel-base superalloy. The crystalline lattice is distorted by the accumulation of dislocations, particularly in the interdendritic regions, which consequently affect the very sensitive Bragg diffraction condition. Assuming Mode-I loading and a plastic zone less than the thickness of the material and, following the Irwin approximation [11], the plastic-zone radius, $r_p$, is determined by the Mode-I SIF and the yield strength, $\sigma_y$:

$$r_p = \frac{1}{2\pi}\left(\frac{K_I}{\sigma_y}\right)^2 \qquad [6.5]$$

From the radiographs, the crack in CMSX-4 34 grew crystallographically, and the fatigue test was paused for a rocking curve about a Bragg angle when the crack reached a projected length of approximately 900 μm with respect to the horizontal (001) plane. Though the tip was subject to mixed-mode loading, the resolved normal stress intensity coefficient ($K_{RNSIC}$) ≈ $K_{RFIC}$ ≈ $K_I$ because of the weak shear stress component [14]. Using the FEA results for $K_{RNSIC}$ of a 900-μm crack along the $(1\bar{1}1)$ and $\sigma_y$ for CMSX superalloys [15], the calculated plastic-zone radius was $r_p$ = 85 μm.

Dislocations broaden and decrease the intensity of the diffracted Bragg peak, and consequently broadening and increasing the intensity of the transmitted Bragg nadir. As discussed in Section 3.3, quantitative strain or dislocation-density calculations are impossible without more rocking curves about multiple axes, which are not possible with the current setup focused on phase-contrast imaging. Instead, the change in lattice quality was mapped qualitatively for CMSX-4 34 by rotating the sample, while under a mean tensile stress, about the single available axis and comparing the nadir width before and after crack propagation. Rotations showed a ~200-μm plastic zone ahead of the crack tip (Fig. 6.8), in reasonable agreement with the results of Eq. 6.5. Nadir broadening occurred near the end of the notch and along the propagation path, because the growing crack deformed the superalloy as its plastic zone advanced. Aside from an isolated spot near the root of the crack, the degree of broadening was generally less significant than at the crack tip, since the tension under which the sample was held during the rotation was concentrated at the tip. High-temperature samples showed significant deformation ahead of the crack tip as well (Fig. 6.9). Where PSBs formed (Fig. 6.9a, black arrows), more nadir broadening was observed.

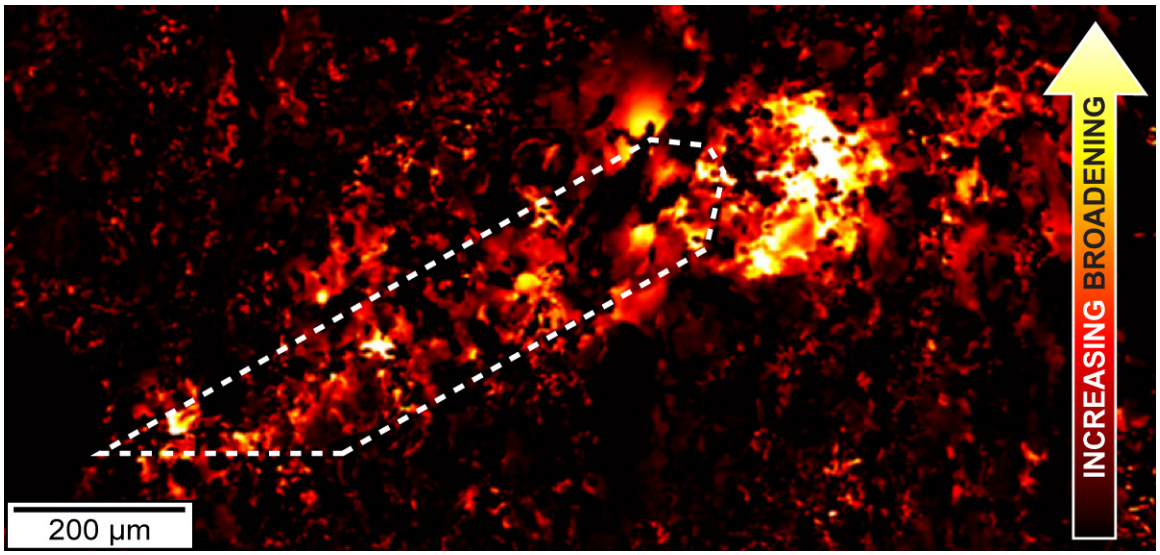


Fig. 6.8. Map of Bragg-nadir broadening due to crack propagation in CMSX-4 34 (Fig. 5.12e) around a crack, which is outlined with a dotted white line. The plastic zone, indicated by the bright region, extends approximately 200 µm ahead of the crack tip.

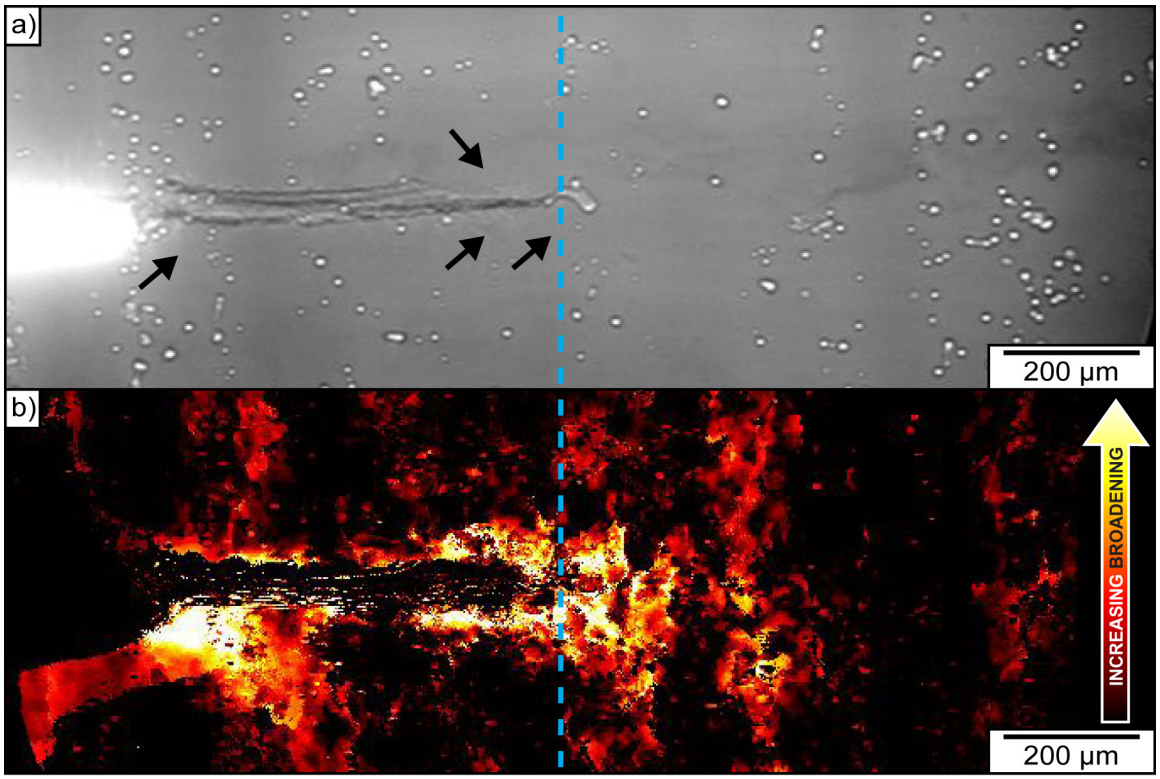


Fig. 6.9. (a) Original radiograph of CMSX-4 37 with PSBs visible (indicated by black arrows but difficult to see with the contrast settings shown here). (b) Map of Bragg-nadir broadening due to crack propagation, showing significant broadening along PSBs and ahead of the crack tip. The blue dotted line indicates the crack tip, as seen from (a).

As the sample was rotated, the projected lateral thickness of the sample decreased slightly, which was enough to decrease the spatial resolution to 3 to 5 μm, depending on the size of the rotation. Since the interdendritic regions were small and had a less uniform nadir width than the dendrites, they erroneously appeared red in Fig. 6.8 without any change in strain in that particular region. Varying the x-ray energy instead of the angle would eliminate geometric changes from rotation, although a rotation of 1° requires a change in energy of several hundred eV. Depending on the particular beamline and its monochromator, a change in the energy could significantly alter the incident intensity and require time to stabilize at a particular temperature with $\Delta E/E \approx 10^{-4}$.

Dislocations ahead of the crack indicate a potential growth direction, whether as a plastic zone or as PSBs; thus, anticipating the direction of a crack is possible before any physical separation occurs between fracture surfaces. Mapping the Bragg nadir requires halting the fatigue test and rotating the sample about 2° or 3° in 0.005° increments and requires about 5 minutes depending on the exposure times. Although still *in situ*, the technique is no longer real-time. Diffraction contrast can still provide details about the plastic zone at the crack tip during normal fatigue testing without a rocking curve if the sample is rotated so that the region ahead of the crack satisfies a Bragg condition. The preceding plastic zone distorts the crystalline lattice and brightens that region into which the crack is about to enter, anticipating the propagation path.

As an example, consider a single frame from crack propagation in CMSX-4 3 (Fig. 6.10). The 500-μm crack had a ~90 μm plastic zone, as calculated using Eq. 6.5 with FEA results for the SIF [14]. The crack tip was well defined by phase contrast (Fig. 6.10, yellow line), and as it grew, it dispersed the Bragg-diffraction shadows with an ever-growing plastic zone (Fig. 6.10, blue line). By rotating the sample to the Bragg angle, no rocking curves or pauses are required; this method can serve as a real-time alternative to the rocking curve for damage detection at the crack tip.

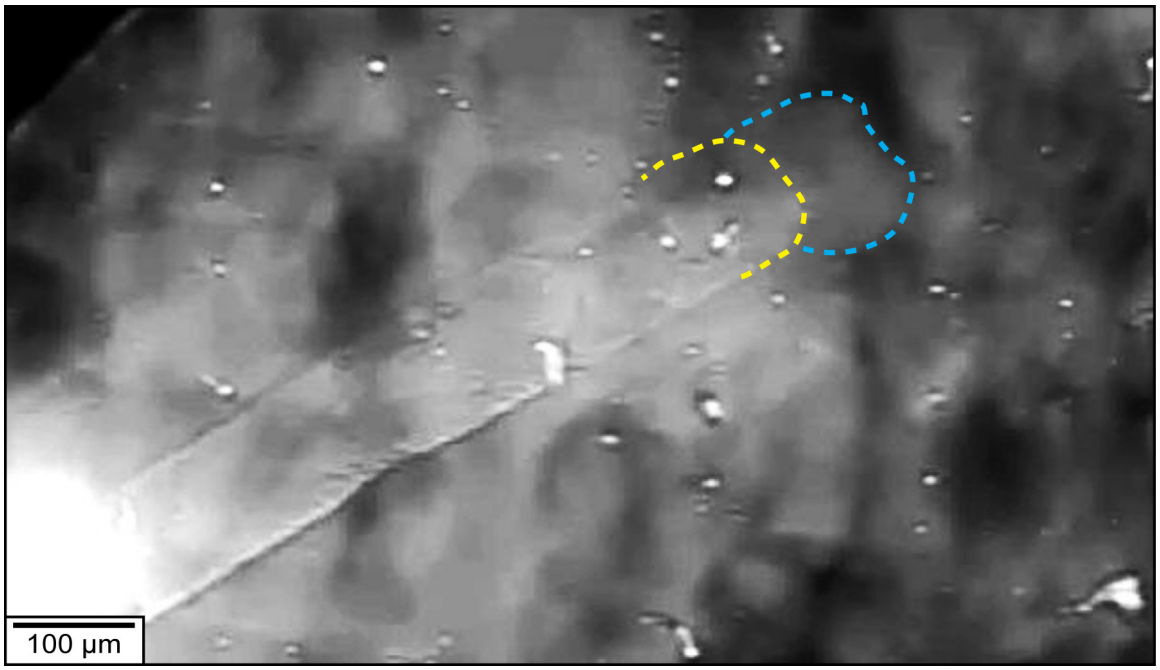


Fig. 6.10. Using diffraction to anticipate the crack path in CMSX-4 3. The plastic zone (blue line) extending approximately 90 µm ahead of the crack tip (yellow line) altered the diffraction condition. The diffraction-contrast shadows were absent in the plastic zone along the direction of crack propagation.

### 6.3.2 Nascent Crack Imaging

Internal crack initiation is impossible to see with non-penetrating imaging techniques. Even detecting the presence with non-imaging techniques, such as nonlinear ultrasonics [16], is very difficult during the initial tens of microns of growth. Phase contrast is extraordinarily sensitive to minimally opened crack tips, as was seen in Fig. 5.7, and can detect the initial distortion emanating from the notch. In RN4 BM 2, a small crack initiated horizontally from the notch at 88,000 cycles along a multitude of planes (Fig. 6.11). It appeared in the holographic regime of PCI, much like the carbides in Fig. 5.6. Secondary extrema beyond the usual primary extrema suggested that the vertical size of the crack at an early stage was even less than the first Fresnel zone. SEM fractography showed a very rough surface with several micron-scale facets that would produce phase contrast on the detector (Fig. 6.12). PSBs along a {111} plane activated at 244,000 cycles (indicated by arrows) while crack growth continued horizontally. Ultimately, the fatal crack grew crystallographically through the previously activated slip

planes before changing directions onto another {111} plane, leaving behind some debris near the inflection point.

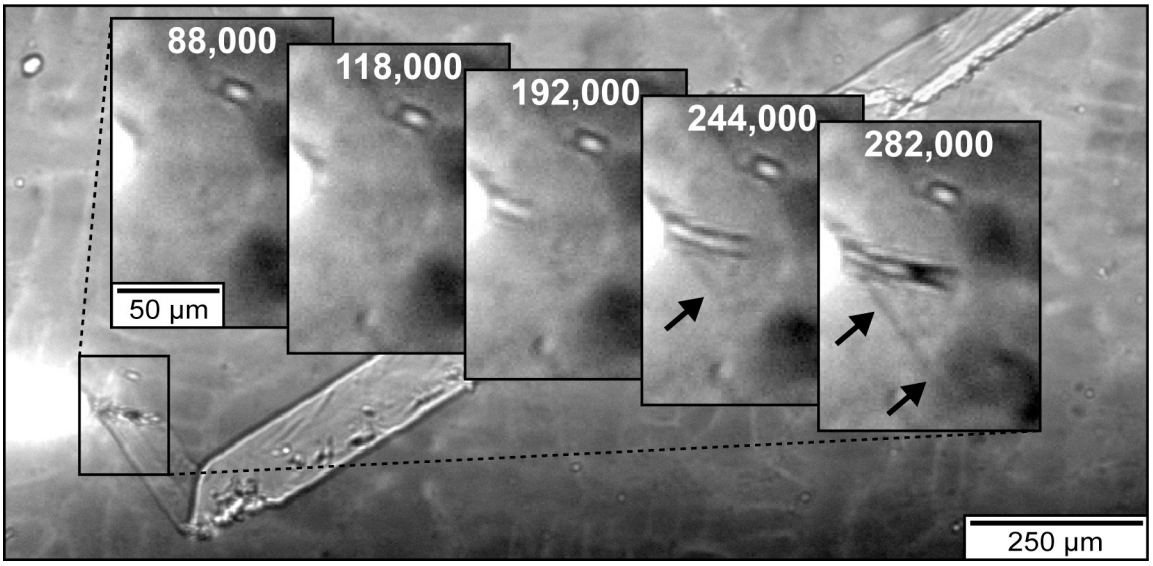


Fig. 6.11. Radiographs showing a crack in RN4 BM 2 grown over 1,167,000 cycles. The five insets show the progression of crack initiation at different cycle counts. The number at the top of each frame indicates the number of elapsed cycles. The crack initially grew horizontally while activating slip planes, indicated by arrows. Eventually, the slip planes became a through-thickness {111} crack.

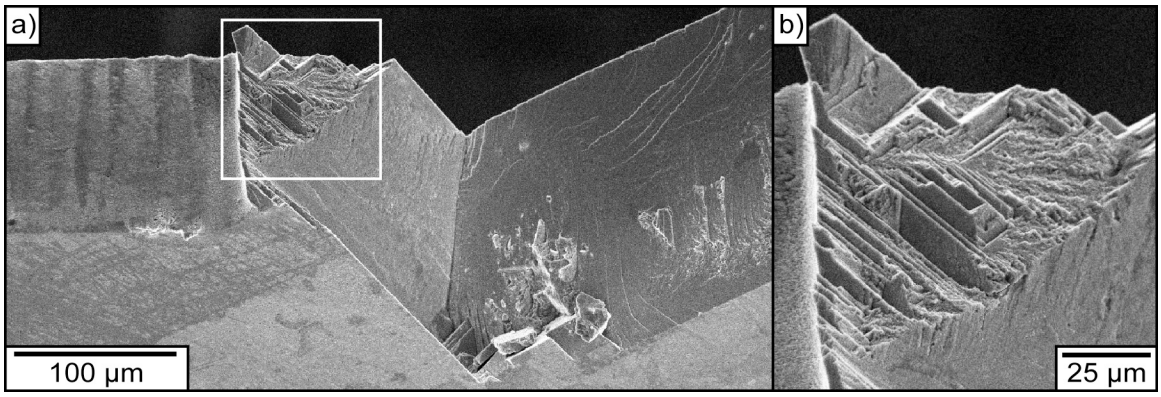


Fig. 6.12. SEM micrographs of RN4 BM 2 near the notch. (a) The crack grew roughly initially until it developed into a through-thickness crystallographic crack; (b) Enlargement of the rough, boxed region of (a).

## 6.4 Discussion

Perhaps the most important feature of an in-line phase-contrast radiography setup is its relative simplicity and flexibility. Air scatter, a problematic source of noise in very sensitive diffraction experiments, is negligible when looking at the very strong transmitted beam; thus, evacuated flight tubes before and after the sample are not required. No restrictive loading chamber is necessary, as in electron microscopy. The experimental table is spacious and modular for additional instrumentation, such as compressed-air jets for cooling or optical cameras for digital image correlation, provided they do not obstruct the beam. An x-ray-transparent enclosure around the fatigue apparatus made of acrylic or plastic can be evacuated or filled with gases or liquids to simulate different environments. Since radiographs require minimal post-processing, the effects of test conditions can be monitored in real time and changed at will.

Reliable and efficient testing methodologies are lacking for high-temperature, high-frequency fatigue tests [1], which is particularly distressing given the normal operating conditions of turbine blades. High-temperature imaging results were presented in Section 6.1, and they agree with prior studies on similar single-crystal superalloys that showed a change in failure mode from crystallographic to Mode I with increasing temperature [10,17]. In these studies, this effect was attributed to oxygen diffusion from the crack-tip region into dislocations, causing oxidation embrittlement and crack-tip blunting. Considering the oxidation visible on the sample surfaces tested at elevated temperatures, this explanation is plausible for the crack behavior in the current experiments, as well. When the torch was deactivated to return the sample to room temperature, once the crack grew beyond the oxidized region, it returned to a {111} crystallographic crack (Fig. 6.4).

The high-temperature tests could be repeated using an x-ray-transparent enclosure under vacuum or other environmental conditions to further study the effects of oxygen. Once all of the associated mechanisms are understood, FEA could be repeated to simulate the SIFs associated with these factors to further understand high-temperature crack propagation. Furthermore, coated superalloys, as they are found in

turbines, could be assayed for their fatigue behavior. YSZ, a typical TBC formulation, has an attenuation length similar to nickel-base superalloys. Real-time imaging would allow detailed studies of growth rate and crack morphology in more realistic operating conditions.

Since the initiation phase is such an appreciable fraction of the high-cycle fatigue (HCF) and VCHF lifetimes, and fatigue damage only occurs very close to failure, components are currently removed from service well before expected failure [12] (e.g., at 3σ from the mean lifetime, or when 0.1% of materials are expected to fail [18]). Routine diagnostics with a technique capable of detecting fatigue damage internally before it becomes catastrophic would, therefore, reduce costs incurred by frequently replacing components that are most likely undamaged and still viable. As demonstrated in Section 6.3, PCI can image micron-sized cracks and persistent slip bands, whether they are internal or at the surface. Internal initiation is common in HCF, so optical or electron microscopy would not detect cracks of this size. Even acoustic techniques, such as ultrasound or non-linear ultrasonics, cannot detect such small cracks [16,19].

Presently, x-ray imaging is the sole technique that can directly and non-destructively image a crack nucleating and slip planes activating. Even greater untapped potential exists for crack prognostication. Before a physical separation between crystallographic planes develops, strain and dislocations build up ahead of the crack tip during fatiguing. These events are seen along crystallographic planes as PSB formation (Fig. 6.11), or more diffusely as plastic zones (Fig. 6.8, 6.9). Before a crack has nucleated from the notch, diffraction contrast should be able to detect the accumulated damage in either of these two forms. If the sample is rotated so that the region ahead of the notch satisfied a Bragg condition, then damage detection would be real-time, as demonstrated in Fig. 6.10. For a more detailed, but not real-time, analysis of damage evolution, the Bragg-nadir broadening could be measured as a function of cycle count around the crack tip using a rocking curve. Identifying crack initiation before any propagation will be the subject of future studies.

On a much shorter time and length scale are the Rayleigh-speed or faster spurts of crack growth [20], nearly 100,000 m/s, as calculated from the elastic modulus and density. This atomic-scale growth regime is presently inaccessible with the current setup, as the spatial and temporal resolutions are too low, although the setup could be modified with existing technology. A higher magnification objective on the camera would improve the spatial resolution, albeit at the expense of the field of view; however, a smaller field of view is unimportant when the site of crack initiation or propagation is known, as in notched samples. Newly developed transmission x-ray microscopy (TXM) provides energy-dependent resolutions of tens of nanometers and exploits all of the contrast mechanisms discussed in Chapter 3 [21-22]. Current TXM designs do not accommodate large testing equipment, such as the ultrasonic fatigue apparatus, but could do so with further development.

For improved temporal resolution, high-speed cameras are available with frame rates of more than 100,000 frames per second [23]. They cannot sustain this for extended durations, since the camera buffer fills rapidly, depending on the image resolution. Imaging must be stopped to read out the data and clear the buffer. A trigger mechanism must activate the camera when crack growth occurs; otherwise, the camera may collect an inordinate number of identical images. Detectors are not the only limitation, though, since the sample thickness limits the exposure time. The shortest exposure time in this work for 100-µm-thick nickel-base superalloys was 100 ms, limiting a camera to 10 Hz assuming no readout time. Samples must be significantly thinner and imaged at a higher x-ray energy to decrease the exposure time down to 10 µs for a 100,000 Hz camera. With improved temporal and spatial sensitivity, radiography could enable studies in a much faster regime of crack propagation that are completely inaccessible to any other technique, complementing the numerous studies described in this chapter.

## 6.5 References


1 Yi, J. Z., Torbet, C. J., Feng, Q., Pollock, T. M. & Jones, J. W. Ultrasonic fatigue of a single crystal Ni-base superalloy at 1000 °C. *Mater Sci Eng A* **443**, (2007).

2 Padture, N. P., Gell, M. & Jordan, E. H. Materials science - Thermal barrier coatings for gas-turbine engine applications. *Science* **296**, (2002).

3 Yablinsky, C. A., Flores, K. M., Mills, M. J., Williams, J. C. & Rigney, J. *Fatigue behavior in monocrystalline Ni-based superalloys for blade applications*. (Minerals, Metals & Materials Soc, 2008).

4 Brundidge, C. L. *Development of a Processing-Structure-Fatigue Property Model for Single Crystal Superalloys*. Ph.D. thesis, University of Michigan, (2011).

5 Chan, K. S., Feiger, J., Lee, Y. D., John, R. & Hudak, S. J. Fatigue crack growth thresholds of deflected mixed-mode cracks in PWA1484. *J Eng Mater Technol* **127**, (2005).

6 Suresh, S. *Fatigue of Materials*. 1st edn, (Cambridge University Press, 1991).

7 Paris, P. C., Erdogan F. A critical analysis of crack propagation laws. *J Basic Eng*, (1963).

8 Paris, P. C., Tada, H. & Donald, J. K. Service load fatigue damage - a historical perspective. *Int J Fatigue* **21**, (1999).

9 Mercer, C., Soboyejo, A. B. O. & Soboyejo, W. O. Micromechanisms of fatigue crack growth in a single crystal Inconel 718 nickel-based superalloy. *Acta Mater* **47**, (1999).

10 Lerch, B. & Antolovich, S. Fatigue crack propagation behavior of a single crystalline superalloy. *Metall Mater Trans A* **21**, (1990).

11 Anderson, T. L. *Fracture mechanics: fundamentals and applications*. 2nd edn, (CRC Press, 1995).

12 Nicholas, T. *High Cycle Fatigue: A Mechanics of Materials Perspective*. (Elsevier, 2006).

13 Miao, J. S., Pollock, T. M. & Jones, J. W. Crystallographic fatigue crack initiation in nickel-based superalloy Rene 88DT at elevated temperature. *Acta Mater* **57**, (2009).

14 Liu, L. *et al.* In situ synchrotron x-ray imaging of high-cycle fatigue crack propagation in single-crystal nickel-base alloys. *Acta Mater* **59**, (2011).

15 Cavaliere, P. & Panella, F. Mechanical and microstructural behaviour of CMSX-4 Ni-based superalloy joined by capacitor discharge welding. *J Mater Process Tech* **183**, (2007).

16 Kumar, A., Torbet, C. J., Jones, J. W. & Pollock, T. M. Nonlinear ultrasonics for in situ damage detection during high frequency fatigue. *J Appl Phys* **106**, (2009).

17 Sengupta, A., Putatunda, S. K. & Balogh, M. Fatigue-crack growth-behavior of a new single-crystal nickel-based superalloy (CMSX-4) at 650°C. *J Mater Eng Perform* **3**, (1994).

18 Engine Structural Integrity Program (ENSIP), MIL-HDBK-1783B,

19 Kumar, A., Torbet, C. J., Pollock, T. M. & Jones, J. W. In situ characterization of fatigue damage evolution in a cast Al alloy via nonlinear ultrasonic measurements. *Acta Mater* **58**, (2010).
20 Abraham, F. F. & Gao, H. J. How fast can cracks propagate? *Phys Rev Lett* **84**, (2000).
21 Yi, J. M. *et al.* Bright-field imaging of lattice distortions using x rays. *Appl Phys Lett* **89**, (2006).
22 Advanced Photon Source Upgrade Conceptual Design Report (Rev. 2). (2011).
23 Photron USA, San Diego, CA.

# CHAPTER 7

# CONCLUSIONS AND FUTURE WORK

## 7.1 Conclusions

The objective of this work was to develop a novel imaging tool for the real-time, *in situ* characterization of industrial materials used in applications of very high-cycle fatigue. Synchrotron x-ray radiography was utilized to image single-crystal nickel-base superalloys using three powerful and versatile contrast modalities – absorption, phase, and diffraction contrast. These three mechanisms provided a wealth of critical microstructural and compositional information about hierarchical superalloys across a breadth of length scales with a single short exposure.

Absorption, determined by the electron density of the material, revealed the dendritic microstructure and intervening interdendritic regions, as well as faintly illuminating small inclusions. Intensity changes within a single dendrite decreased toward the center, enabling the two-dimensional mapping of elemental composition over the entire field of view. This approach revealed the segregation of rhenium and tungsten to the dendritic cores that occurs during solidification.

Absorption contrast also exposed propagating cracks, and the change in intensity associated with absorption quantified the amount of crack opening in the through-thickness direction. These openings do not need to be very large: only 1 μm in a 200-μm-thick sample for the monocrystalline superalloys studied in this work. The small displacements measured in crystallographic cracks suggested mixed-mode crack propagation, which was explicated by finite element analysis. Cracks grew as a combination of all three fracture modes, favoring the {111}<110> slip system and particularly $(1\bar{1}1)$ planes at room temperature. For higher temperatures around 538°C,

they still grew along {111} planes, but they showed evidence of roughness aligned with the interdendritic regions. At even higher temperatures above ~600°C, both crystallographic slip bands and Mode-I non-crystallographic cracking were observed simultaneously, though the Mode-I crack ultimately dominated. When both crack morphologies grew simultaneously, the growth rate slowed substantially. Therefore, absorption contrast with synchrotron x-ray radiography provided detailed information about the morphology of crack propagation in real time.

Phase contrast enhanced the sensitivity of absorption contrast and revealed even smaller crack openings and minuscule microstructural defects invisible to incoherent laboratory x-ray sources. The borders between regions of different composition were marked by strong constructive and destructive interference fringes. Cracks opened by mere hundreds of nanometers were resolvable, along with the internal interfacial roughness. Phase contrast revealed the precise position of crack tips to within the micron-scale spatial resolution of the detector, allowing accurate measurements of crack-growth rates and Paris Law fits. It also identified the earliest stages of crack initiation that grew horizontally from a notch along several small steps, which occurred before the crack developed into a through-thickness {111} planar crack. This nascent crack growth, when nucleating internally, cannot be imaged *in situ* with any other non-destructive technique. To our knowledge, this work is the first to report on real-time x-ray phase contrast studies of fatigue-crack dynamics.

Diffraction contrast examined details of the crystallographic structure by mapping mosaicity, strains, and dislocations. Dendrites in these materials had slight tilt misorientations with respect to one another of 1° to 2°, with the interdendritic regions containing dislocation densities measured between 1 and 3 x $10^7$ dislocations/$cm^2$. The change in nadir broadening before and after cracking revealed strained and plastically deformed regions, such as those shed by the advancing crack, as well as the hitherto inaccessible region ahead of the crack tip. The advancing plastic zone ahead of a crack tip, when imaged with diffraction contrast, anticipated the crack path. This modality, particularly in concert with phase contrast, promises the capability for determining both

when cracks will develop and the course they will traverse through the material. This information would be invaluable in industrial applications to evaluate the single-crystal nickel-base superalloy materials and predict when they should be retired from duty before catastrophic failure.

This dissertation has shown that synchrotron x rays are sensitive to many features simultaneously, and the movies of three-dimensional crack propagation are, to our knowledge, the first of their kind. Given the success of the experiments in the previous chapters and the excitement shown by scientists and engineers to see what happens in real time rather than *ex post fracto*, this tool could see widespread use in the future in several applications.

## 7.2 Future Work

Some possible future directions have been described in the discussion sections of Chapters 4-6. These include studies of high-temperature creep damage; three-dimensional tomography of cylindrical samples; thicker samples in different environments, such as vacuum or corrosive gases; and detailed imaging of crack initiation and the preceding dislocation evolution. This work has shown phase-contrast imaging (PCI) of fatigue damage in single-crystal Ni-base superalloys, but several different classes of materials deserve further attention, and improving imaging technology augurs well for the future of real-time, *in situ* diagnostics with x rays.

### 7.2.1 Different Metals

All materials described in this dissertation were single-crystal Ni-base superalloys. While these metals are critical constituents of turbine engines operating at high-temperature, other important superalloys have different advantages and are the basis of ongoing research. Single-crystal cobalt-base superalloys, for example, have recently been fabricated to have a γ/γ′structure for improved fracture toughness [1]. Compared to their Ni-base cousins, cast Co-base superalloys, such as Co-9.4Al-10.7W (with possible additions of Ta and Cr [2]) are comparable in strength at 900°C and have

better corrosion and oxidation resistance [1,3]. Some have even higher melting points than Ni-base materials, making them less susceptible to thermal stresses in high-temperature applications. From an x-ray imaging perspective, Co-base superalloys are very similar to Ni-base superalloys, with a similar attenuation coefficient (depending, of course, on the x-ray energy). X-ray imaging techniques, similar to those of Chapter 4, could use the Co $K_\alpha$ absorption edge of 7.7 keV to study the solidification characteristics and mosaicity, and higher energies would require shorter exposure times during imaging of fatigue-crack propagation. As the temperature limits of current Ni-base superalloys are reached, Co-base superalloys are promising candidates for future high-temperature applications in turbine blades and elsewhere.

In lower-temperature applications, polycrystalline materials are common in situations where their higher susceptibility to creep and fatigue-crack initiation at grain boundaries compared with single-crystal materials is not as detrimental. Preliminary work on the polycrystalline Ni-base superalloy Haynes 282 [4] has shown that crack propagation is still clearly visible (Fig. 7.1), particularly because the crack path is transgranular along a horizontal, Mode-I path. This crack morphology increased the opening in the through-thickness direction much more than did the multi-mode crystallographic cracks observed with single-crystal materials, making the crack and its path much more visible with PCI.

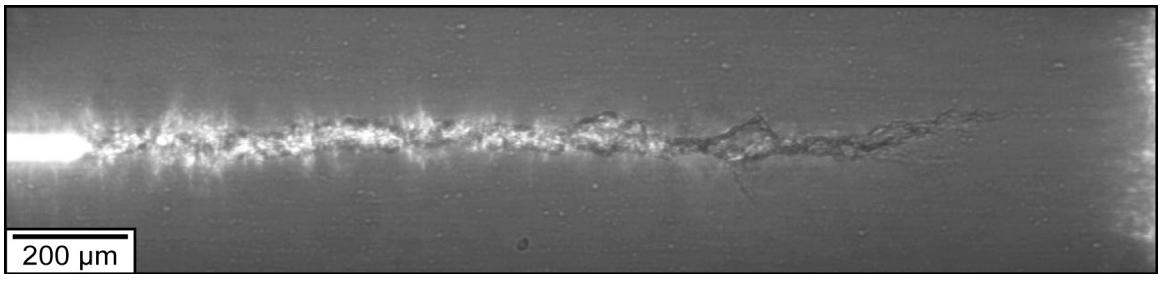


Fig. 7.1. Crack propagation as a transgranular Mode-I crack in polycrystalline Haynes 282 superalloy.

For materials with simpler composition, such as pure Ni annealed at 960°C for an average grain size of ~400 µm, crack growth was again Mode-I and easy to image

accurately (Fig. 7.2). Grain boundaries were identified by rotating the sample through several angles and mapping the angles at which they diffracted (Fig. 7.2a). This method was possible because the grain sizes were generally greater than the thickness of the sample, although grain boundaries were assumed to be oriented perpendicular to the sample surface, which is most likely an oversimplification. Maps of grain boundaries are analogous to the mosaicity maps of dendritic microstructure, though they cannot easily identify the precise crystallographic orientation of each grain without knowing which Bragg angle is diffracting. Overlaying the grain boundaries on the radiograph of crack propagation revealed how the tortuous path wended both transgranularly and intergranularly. Understanding crack propagation and initiation with respect to grain boundaries is of interest not only in polycrystalline materials but in single crystals as well, where low- and high-angle grain boundaries may occur during fabrication or when forming complicated geometries [5].

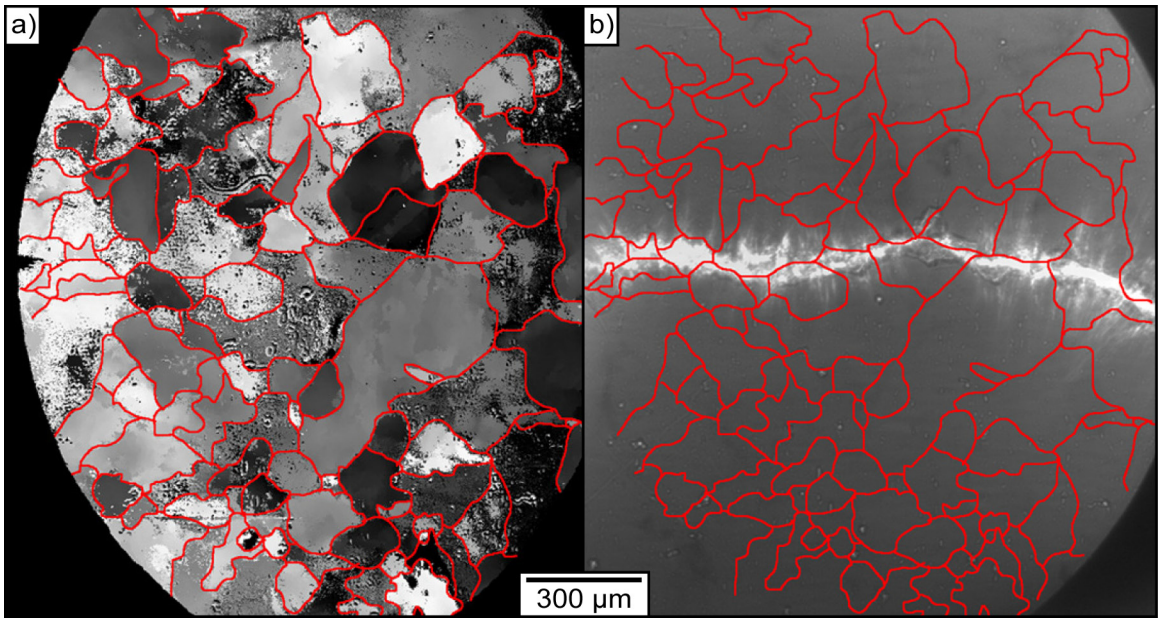


Fig. 7.2. (a) Map of Bragg diffraction nadirs with grain boundaries outlined in red. (b) Crack propagation in a sample of pure nickel annealed at 960°C showing both transgranular and intergranular propagation. The average grain size was ~400 µm. Sample prepared by Dr. M. Zimmermann.

Polycrystalline materials are generally much more common in applications outside of high-temperature regions in turbine blades subject to extreme conditions. Fatigue cracks are easily imaged concurrently with the microstructural details, which extends PCI's applicability to many more important materials. For lighter structural materials, such as aluminum or magnesium (Fig. 7.3), x rays can penetrate much thicker samples and provides diagnostics of more realistic operational components. Improving understanding about microstructure and its role in crack propagation and initiation, especially in the high-cycle fatigue regime, can impact many more materials science applications than just turbine blades.


Fig. 7.3. AXJ530 magnesium alloy die-cast as a 5-mm-diameter cylinder and tested at a stress amplitude ratio of R = –1. A crack initiated at the largest pore, indicated by the arrow, and grew as a semicircle in the horizontal plane. Because the optical path length is much greater in the center of the cylinder, the crack is harder to see in the center, but it is still visible with the proper contrast settings. Sample prepared by Dr. A. Kumar.

### 7.2.2 Biological Materials

The opportunities in hierarchical biological structural materials, from cortical bone to nacre to dentin, are just as diverse as in inorganic materials. Biological minerals, such as the carbonate minerals found in the skeletons of mollusks and echinoderms, often have a disordered crystal structure and can achieve the wide variety of shapes and structures observed in nature [6-7]. In vertebrates, the carbonated apatite in bone and dentin is organized in a complex structure containing many compositional and architectural features across several length scales, similar to superalloys [7] (Fig. 7.4a). At the scale of the γ/γ′ structures are the mineral crystals and tro pocollagen molecules that form the mineralized collagen fibrils, which are the foundation of bone. These

components form fibril arrays collected into collagen fibers of ~10 µm, comparable to the size of the interdendritic regions of superalloys. Collections of uniformly oriented fibers form lamellar structures, on the spatial scale of dendrites, which have distinct lamellar interfaces between differently oriented lamellar structures; this is analogous to dendritic/interdendritic borders so easily imaged by radiography. Above this length scale, several larger meso- and macroscopic structures exist for different classes of bone.

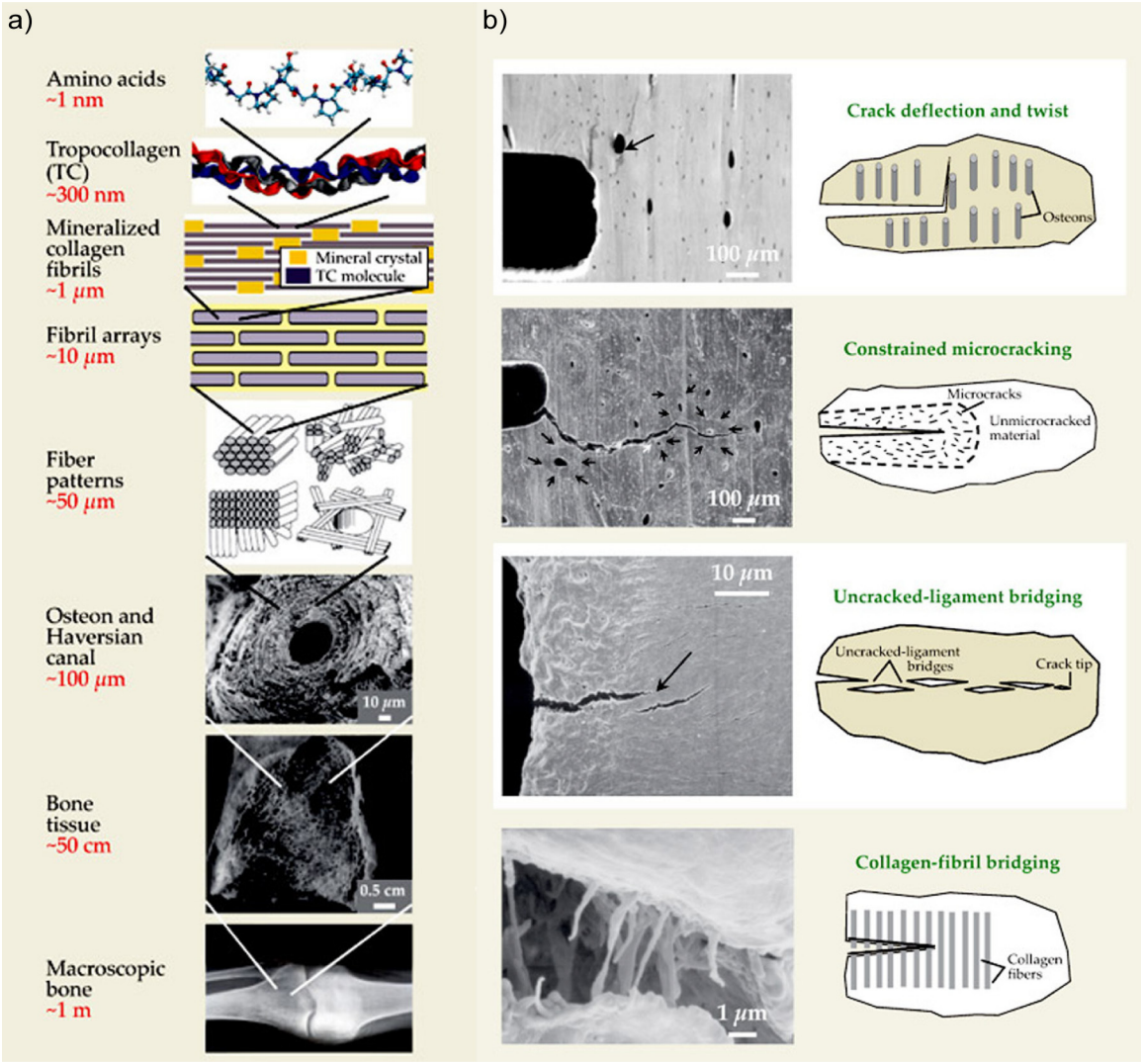


Fig. 7.4. (a) Hierarchical structure of bone spanning $10^9$ spatial orders of magnitude. (b) Toughness mechanisms in bone, again across several orders of magnitude. Adapted from [7].

Fatigue tests performed in vertebrate tissues are usually performed near 1 Hz to match physiologic loading regimes, although a few studies have looked at superphysiologic frequencies in the 50-70 Hz range to examine mechanisms of crack growth and fatigue behavior [8]. Such studies cannot easily test fatigue damage, since large numbers of low-stress cycles are required and may be impractical at 50 Hz. Cortical bone in particular has a number of interesting mechanisms to enhance toughness and restrict crack propagation [7] (Fig. 7.4b). For example, cracks may deflect up to 90° when they encounter osteons, which are long, ~200-µm-diameter cylinders comprised of concentric layers of mineralized collagen fibril arrays. This natural deflection mechanism may increase bone's toughness by up to 20 $MPa \cdot m^{1/2}$ [7,9]. Obviously, this effect is highly dependent on the orientation of the crack with respect to the osteonal structure and is one cause of the severe anisotropy in bone fracture mechanics. Toughness is five times higher (though not high enough for many athletes) across the bone than along it [10].

Another toughening effect is uncracked-ligament bridging, seen in metal-matrix composites as well as bone [11], where an unbroken region separates different parts of the crack. This event spreads the load among the different disconnected portions of the crack and can increase the toughness by a few $MPa \cdot m^{1/2}$ [7,9]. On a nanometer scale, collagen fibrils can bridge narrowly opened cracks, increasing the toughness by ~0.1 $MPa \cdot m^{1/2}$ [7]. The effect is too small to image with the current setup, but it may soon become possible with transmission x-ray microscopes and improved imaging beamlines and detectors. Visualizing the toughening phenomena and quantifying their effect on the crack growth rate, particularly in the kHz-frequency, low-strain regime would be interesting for both bone studies and potential biomimetics applications.

### 7.2.3 New and Improved Imaging Technology

Imaging beamlines are critically important for many applications due to their versatility and sensitivity, and they are present at nearly every major synchrotron source in the world. As such, significant interest exists for better imaging beamlines by

improving the field of view (FOV), spatial resolution, and temporal resolution. New wide-field imaging (WFI) beamlines address these needs, including a WFI beamline currently under development at the Advanced Photon Source (APS) of Argonne National Laboratory, the synchrotron used extensively in this dissertation. Whereas the source-to-sample distance was 75 m in work performed at Sector 32, the new beamline would be located ~250 m downstream from the monochromator with a beam size of 25-50 mm horizontally and 10-20 mm vertically [12]. This expanded FOV is a few hundred times larger than the current 1.8 x 1.5 mm FOV at Sector 32, although the larger beam size would sacrifice photon density; thus, imaging would require higher x-ray photon energies to prevent prohibitively long exposure times. In the fatigue experiments presented, all samples contained notches to hasten crack initiation and localize it to a particular region within the FOV. Without a notch, a crack would likely initiate at the microstructural feature causing the greatest stress intensity, possibly an inclusion or grain boundary, and a wide FOV could see more such features and simultaneously image many more potentially fatal defects to better understand initiation.

Increasing the source-to-sample distance improves the projected source size (Eq. 3.24). This smaller projection improves the resolution of phase contrast, as it defines the point-spread function over which the theoretical intensity is convolved, effectively blurring the spatial resolution. A smaller projected source size also increases the transverse coherence length (Eq. 3.26), so larger features can be imaged in the holographic regime of phase contrast. This effect is not as critical for strongly absorbing objects imaged in the edge-enhancement regime, but it is necessary for studies of more weakly absorbing objects, such as those in biological systems or inclusions with a similar attenuation length to the surrounding material.

Beyond third-generation synchrotron sources are a new generation of x-ray sources that promise femtosecond pulses and even greater coherence – free electron lasers (FELs) [13]. Facilities such as the newly-commissioned LINAC (linear accelerator) Coherent Light Source (LCLS) [14] have an x-ray brightness ten billion times greater than a synchrotron, to the level where samples are quickly damaged or destroyed when

imaged [15]. The source size is smaller overall than at the APS, which improves coherence. For example, the projected source size at the coherent x-ray imaging (CXI) instrument hutch, located 440 m from the source, is 60 μm by 60 μm at 8.3 keV [16]. Note, however, that synchrotrons still have some very distinct advantages in PCI over FELs. The FOV at the CXI is 750 μm by 750 μm for the unfocused beam, while at the proposed APS WDI, the FOV will be one or two thousand times larger. The CXI has a maximum x-ray energy of 25 keV, while at the APS energies can reach hundreds of keV, depending on the beamline, albeit with a significantly lower brightness. For any high-speed time-resolved studies of fatigue-crack propagation, an FEL is ideal given its short pulse duration and incredible brightness; however, for wider FOVs where the edge-enhancement regime of PCI is sufficient, synchrotrons are still the instrument of choice.

Obviously synchrotron and FELs are unwieldy and expensive tools unfit for field diagnostics, and beamtime, particularly given the current dearth of FELs, is at a premium. As discussed in Section 5.5, neutron and gamma-ray sources are also potential imaging tools, but they each have their limitations, and neither is as widely available as x-ray sources. Advances in laboratory x-ray sources may someday provide portable temporally and spatially coherent radiation sources, though they currently lack the brilliances of third-generation synchrotron sources. Laser-based x-ray sources, for example, focus intense, relativistic laser pulses on a gas or metal target to form a dense plasma [17]. The emitted x rays are monochromatic, with the energy determined by the $K_\alpha$ edge of the target. Combining the narrow energy bandwidth with the pulsed nature of the laser, the radiation is temporally coherent. More importantly for phase contrast, though, the radiation is spatially coherent due to the tight focusing of the laser by a parabolic mirror down to <1 μm. The small spot size produces a small source size, reducing the sample-to-detector distances necessary for phase contrast, and this is important for improving photon counts at the detector without a narrowly collimated beam. Laser-based x-ray sources have successfully produced phase-contrast radiographs of biological objects [18], and continued development in this direction may eventually lead to portable sources with sufficient brilliance to image cracks and map strain fields

without a large, billion-dollar facility. Until then, synchrotron x-ray sources will continue to be the premier sites for real-time, *in situ* diagnostics of materials that impact the worlds of science and engineering.

## 7.3 Reference


1 Sato, J. *et al.* Cobalt-base high-temperature alloys. *Science* **312**, (2006).

2 Tsunekane, M., Suzuki, A. & Pollock, T. M. Single-crystal solidification of new Co-Al-W-base alloys. *Intermetallics* **19**, (2011).

3 Suzuki, A., DeNolf, G. C. & Pollock, T. M. Flow stress anomalies in gamma/gamma' two-phase Co-Al-W-base alloys. *Scripta Mater* **56**, (2007).

4 Haynes International, Inc, Kokomo, IN.

5 Pollock, T. M. & Murphy, W. H. The breakdown of single-crystal solidification in high refractory nickel-base alloys. *Metall Mater Trans A* **27**, (1996).

6 Weiner, S., Sagi, I. & Addadi, L. Choosing the crystallization path less traveled. *Science* **309**, (2005).

7 Ritchie, R. O., Buehler, M. J. & Hansma, P. Plasticity and toughness in bone. *Phys Today* **62**, (2009).

8 Kruzic, J. J., Nalla, R. K., Kinney, J. H. & Ritchie, R. O. Mechanistic aspects of in vitro fatigue-crack growth in dentin. *Biomaterials* **26**, (2005).

9 Nalla, R. K., Kinney, J. H. & Ritchie, R. O. Mechanistic fracture criteria for the failure of human cortical bone. *Nat Mater* **2**, (2003).

10 Koester, K. J., Ager, J. W. & Ritchie, R. O. The true toughness of human cortical bone measured with realistically short cracks. *Nat Mater* **7**, (2008).

11 Shang, J. K. & Ritchie, R. O. Crack Bridging by Uncracked Ligaments during Fatigue-Crack Growth in Sic-Reinforced Aluminum-Alloy Composites. *Metall Trans A* **20**, (1989).

12 Advanced Photon Source Upgrade Conceptual Design Report (Rev. 2). (2011).

13 Vartanyants, I. A. *et al.* Coherence Properties of Individual Femtosecond Pulses of an X-Ray Free-Electron Laser. *Phys Rev Lett* **107**, (2011).

14 Emma, P. *et al.* First lasing and operation of an angstrom-wavelength free-electron laser. *Nat Photonics* **4**, (2010).

15 Boutet, S. & Williams, G. J. The Coherent X-ray Imaging (CXI) instrument at the Linac Coherent Light Source (LCLS). *New J Phys* **12**, (2010).

16 LCLS. *Coherent X-ray Imaging Technical Specs*, <https://slacportal.slac.stanford.edu/sites/lcls_public/instruments/cxi/Documents/CXItechspecs.pdf> (2011).

17 Hou, B. *et al.* Hard X-ray generation from solids driven by relativistic intensity in the lambda-cubed regime. *Appl Phys B* **83**, (2006).

18 Boschetto, D. *et al.* Spatial coherence properties of a compact and ultrafast laser-produced plasma keV x-ray source. *Appl Phys Lett* **90**, (2007).